DEVELOPMENT OF SOL-GEL DERIVED HYDROXYAPATITE-TITANIA COATINGS

A THESIS SUBMITTED TO
THE GRADUATE SCHOOL OF NATURAL AND APPLIED SCIENCES
OF
MIDDLE EAST TECHNICAL UNIVERSITY

BY

NUSRET SERHAT ÜN

IN PARTIAL FULFILLMENT OF THE REQUIREMENTS
FOR
THE DEGREE OF MASTER OF SCIENCE
IN
METALLURGICAL AND MATERIALS ENGINEERING

APRIL 2008

Approval of the thesis:

DEVELOPMENT OF SOL-GEL DERIVED HYDROXYAPATITE-TITANIA COATINGS

Submitted by **NUSRET SERHAT ÜN** in partial fulfillment of the requirements for the degree of **Master of Science in Metallurgical and Materials Engineering Department, Middle East Technical University** by,

Prof. Dr. Canan ÖZGEN _____
Dean, **Graduate School of Natural and Applied Sciences**

Prof. Dr. Tayfur ÖZTÜRK _____
Head of Department, **Metallurgical and Materials Engineering**

Assist. Prof. Dr. Caner DURUCAN _____
Supervisor, **Metallurgical and Materials Engineering Dept., METU**

Examining Committee Members:

Prof. Dr. Muharrem TİMUÇİN _____
Metallurgical and Materials Engineering Dept., METU

Prof. Dr. Abdullah ÖZTÜRK _____
Metallurgical and Materials Engineering Dept., METU

Assist. Prof. Dr. Caner DURUCAN _____
Metallurgical and Materials Engineering Dept., METU

Assist. Prof. Dr. Zafer EVİS _____
Department of Engineering Science, METU

Assist. Prof. Dr. Arcan DERİCİOĞLU _____
Metallurgical and Materials Engineering Dept., METU

Date: 17.04.2008

I hereby declare that all information in this document has been obtained and presented accordance with the academic rules and ethical conduct. I also declare that, as required by these rules and conduct, I have fully cited and referenced all material and results that are not original to this work.

Name, Last name : Nusret Serhat ÜN

Signature :

ABSTRACT

DEVELOPMENT OF SOL-GEL DERIVED

HYDROXYAPATITE-TITANIA COATINGS

Ün, Nusret Serhat

M.Sc., Department of Metallurgical and Materials Engineering

Supervisor: Asst. Prof. Dr. Caner Durucan

April 2008, 109 pages

A processing route for development of hydroxyapatite ($Ca_{10}(PO_4)_6(OH)_2$ or HAp)-titania (TiO_2) hybrid coatings on titanium alloy (Ti6Al4V) has been established. HAp powders of different size and morphology were synthesized by aqueous precipitation techniques using different precursor couples and XRD, SEM and FTIR were performed for complete characterization. Hybrid coatings were then prepared via sol-gel by incorporating pre-synthesized HAp powders into a titanium-alkoxide dip coating solution. Titania network is formed by hydrolysis and condensation of Ti-isopropoxide ($Ti[OCH(CH_3)_2]_4$) based sols. The effect of titania sol formulation, specifically the effect of organic solvents on the microstructure of the dip coated films calcined at 500 ºC has been investigated. The coatings exhibit higher tendency for cracking when a high vapor pressure solvent, such as ethanol (C_2H_5OH) is used

causing development of higher macroscopic stresses during evaporation of the sol. Titania sol formulations replacing the solvent with *n*-propanol ($CH_3(CH_2)_2OH$) and acetly-acetone (C_5H_8O) combinations enhanced the microstructural integrity of the coating during evaporation and calcination treatments. Sol-gel processing parameters such as multilayer coating application and withdrawal rate can be employed to change the titania thickness in the range of 0.120 μm-1.1 μm and to control the microstructure of HAp-titania hybrid coatings. Slower withdraw rates and multi-layer dip coating lead to coatings more vulnerable to cracking. A high calcination temperature in the range of 400 ºC-600 ºC lead to more cracking due to combined effect of densification originated stresses and thermal stresses upon cooling.

Keywords: Hydroxyapatite, titania, sol-gel, Ti6Al4V, bone

ÖZ

SOL-JEL YÖNTEMİYLE HİDROKSİAPATİT-TİTANYA KAPLAMALARIN GELİŞTİRİLMESİ

Ün, Nusret Serhat

Y. Lisans, Metalurji ve Malzeme Mühendisliği Bölümü

Tez Yöneticisi: Yrd. Doç. Dr. Caner Durucan

Nisan 2008, 109 sayfa

Titanyum alaşımları (Ti6Al4V) üzerine hidroksiapatit ($Ca_{10}(PO_4)_6(OH)_2$ veya HAp) – titanya (TiO_2) hibrid kaplamaları geliştirmek için üretim yöntemleri tayin edildi. Farklı tane boyutuna ve morfolojiye sahip HAp tozları farklı başlangıç bileşenleri kullanılarak sulu çökeltme yöntemiyle üretildi. Tozların ve kaplamaların karekterizasyonu XRD, SEM ve FTIR analizleri ile gerçekleştirildi. Hibrid kaplamalar, daha önceden sentezlenmiş HAp tozlarının titanyum-alkoksit çözeltisine katılmasını kapsayan sol-jel yöntemiyle hazırlandı. Titanya ağ, Ti-isopropoksit ($Ti[OCH(CH_3)_2]_4$) bazlı solun hidroliz ve yoğunlaşma reaksiyonları sonucunda hazırlandı. Titanya sol formülünün ve kullanılan organik çözücülerin daldırma yöntemiyle kaplanmış ve 500 ºC'de kalsine edilmiş filmlerin mikroyapısına etkisi incelendi. Ethanol (C_2H_5OH) gibi yüksek buhar basıncına sahip çözücüler kullanıldığında kuruma sırasında oluşan yüksek makroskopik

gerilim sonucu çatlaklı yapıda kaplamaların oluştuğu gözlendi. Buna karşılık titanyumdioksit sol formülünde n-propanol ($CH_3(CH_2)_2OH$) ve asetil aseton (C_5H_8O) gibi organik çözücüler kullanılması buharlaşma ve kalsinasyon işlemleri sonrasında mikro yapısal bütünlüğünü daha iyi olan kaplamaların elde edilmesini sağlamıştır. Çok katmanlı kaplama uygulamaları ve daldırmalı kaplama çekme hızı gibi sol-jel üretim yöntemi parametrelerinde yapılan değişikliklerin hem kaplama kalınlığının 0.120 μm-1.1 μm aralığında değiştirilebileceğini hem de HAp-titanya hibrid kaplamaların mikroyapısının kontrol edilebileceğini göstermiştir. Daldırma yönteminde düşük çekme hızları kullanılarak elde edilen kaplamaların ve çok katmanlı kaplamaların çatlak oluşumu yönünden zayıf olduğu gözlemlenmiştir. Bunun yanında, 400-600 ºC aralığında yüksek kalsinasyon sıcaklıkları titanyumdioksit matris ya da HAp kristal yapısında önemli bir değişikliğe yol açmamakta, fakat soğuma sırasında kaplamanın yoğunlaşmasından doğan gerilimler ve termal gerilimlerin sebep olduğu çatlak oluşumuna neden olmaktadır.

Anahtar Kelimeler: Hidroksiapatit, titanya, sol-jel, Ti6Al4V, kemik

To my family…

ACKNOWLEDGEMENTS

I sincerely acknowledge Assist. Prof. Dr. Caner Durucan for his genuine support, guidance and patience with friendly and encouraging attitude. This thesis would never be in process without his effort and comments.

I sincerely thank Prof. Dr. Mehmet Parlak for his help in coating thickness measurements.

I would like to thank Hande Akseki for her endless smile and love even in my gloomy times. That was meaning a lot to me and still…

I must thank to Nihat Ali Işıtman, Muratahan Aykol, Cem Topbaşı for their sincere friendship. I would never expect to have such great people that I could get along perfectly. I genuinely thank them for all the precious times that we spent.

I would like to thank and appreciate my teammates – Betül Akköprü, Derya Kapusuz, Özlem Altıntaş, Dilek Işık, Onur Rauf Bingöl. Chats, laughs and discussions beside science and their never ending support could not have been more helpful for me in this period. Special thanks to Özlem Altıntaş for helping me with the SEM analyses.

I am really grateful to "Nova Lab" members Nagehan Duman, Sıla Süer, Mehmet Yıldırım, Ozan Özkan for their kindness and infinite friendship that they made me feel.

I would like to thank Ziya Esen and Kaan Çalışkan for their help about dealing with problems and support.

My family – mom and dad…. my best encouragers… neither love could be like their's. Thank you for everything…

TABLE OF CONTENTS

LIST OF TABLES

LIST OF FIGURES

CHAPTER 1

INTRODUCTION

1.1. General introduction and rationale of the thesis

Metal alloys have been used in biomedical applications as bone implants and/or bone fracture fixation devices. Metals are usually the common choice in this type of applications because of their excellent mechanical properties satisfying load bearing. Cobalt chromium alloys, stainless steels and titanium alloys are the most common materials used as the metallic biomaterials. Titanium alloys –especially Ti6Al4V- are one step ahead among these metals by offering the combination of significant mechanical properties of high strength, fracture toughness and light weight. The major problem for metallic implants is the metallic ion release from their surfaces and limited biological interaction/integration with the bone tissue. These problems can be solved by introducing a bioactive coating (e.g. HAp) on these metals.

HAp coatings are widely used to modify metallic implant surfaces because of their chemical resemblance to bone with intrinsic biocompatibility and osteointegration potential. Additionally, HAp coatings also limit the adverse toxic effects of the metal. This biologically active ceramic alone lack critical mechanical property, fracture toughness for bone replacement. Thus, implants of Ti6Al4V metals with HAp coatings can provide the superior combination of mechanical and biological properties.

A bioactive surface finish of a titanium alloy can be obtained by simply coating the titanium alloy with HAp. The functional properties of such coating can be further improved by incorporating the HAp in a coating matrix to achieve freedom in tailoring the physical properties of the coating as well to provide flexibility in processing. In addition, choosing a HAp-hosting coating with a chemical similarity to the metal substrate is more significant in terms of achieving better physical integration of the coating to the titanium alloy. In this sense, coating a titanium alloy with the HAp-titania hybrid can offer some additional advantages. Titania matrix can act as a chemical and physical buffer layer for effective attachment of HAp particles on titanium alloy. This combination can also offer use of simple processing methods by adapting available knowledge related to the preparation of titania coatings by wet chemistry techniques, such as sol-gel. Additionally, titania also exhibits bioactivity due to dynamic surface activation promoting bonelike apatite formation in physiological conditions. Therefore these hybrid coatings may provide improved bioactivity, strong titanium alloy-HAp bonding and high corrosion resistance.

Various techniques are available for the processing HAp-titania hybrid coatings such as: plasma spraying, sputtering, electrophoresis, electrochemical deposition, biomimetic methods and sol-gel techniques. Sol-gel technique has certain advantages over the rest of the processing techniques. First of all, as a low temperature aqueous technique, it is applicable to complex substrate geometries by practical means such as dip coating. Moreover, sol-gel chemistry can be controlled to change microstructure, size and scale of the porosity and surface area. In addition, solution properties for each individual coating step can be controlled in multilayered film applications to control thickness and to achieve gradient chemical and structural modifications for the coating layers. Aqueous nature of the sol-gel technique can also help to add new functions such as possibilities to incorporate growth factors for an improved biomedical use.

HAp-titania hybrid coatings can be prepared by several sol-gel routes. In direct routes, a coating sol leading to *in situ* formation of hybrid glassy coating from an aqueous parent solution containing titanium alkoxide, calcium and phosphorus sources can be used. Amorphous and large specific surface area coatings can be prepared by this approach in a single step, but direct routes employ complex chemistry and require use of relatively costly organic precursors for calcium/phosphorus. Alternatively, crystalline HAp powders can be incorporated and encapsulated in an organic solution of titanium alkoxide during gelling. This route was followed in this thesis and was more practical in terms of tailoring the microstructural properties by simple manipulations in the HAp powder properties, together with adjusting the solution chemistry of the titania sol.

The general objective of this thesis is to establish the sol-gel processing routes for development of HAp-titania hybrid coatings on Ti6Al4V by dip coating. HAp powder is custom synthesized by aqueous precipitation methods and introduced to the sol-gel derived titania matrix by mechanical mixing methods. The titania film network is obtained using the sol-gel formulations via direct hydrolysis and condensation of an organic metal alkoxide, Ti-isopropoxide. The chemical and microstructural investigations and modifications on coating properties have been performed as function of several processing parameters. The effects of multiple coating layer application, chemical formulation of the titania sol, calcination temperature and withdrawal rate on coating microstructure have been investigated in a systematic way.

1.2. Background information and literature review

1.2.1. Structure and properties of bone

Bone is a composite material which consists of collagen (20%), calcium phosphate (69%) and water (9%) [1]. Moreover, there are some organic materials such as lipids, polysaccharides and more than 200 proteins involve in the structure of bone [2].

As a main organic constituent, Type I collagen matrix is found in the fiber and these fibers are arranged in parallel form in lamella in dense bone. These fibers contain fibrils with 80-100 nm length [3]. The nature of these fibrils is triple helix consisting two α_1 and one α_2 polypeptide chains of aminoacids. On the other hand, apatite crystals in bone structure own the mineral part. These needle or rod like crystals are known as "biological apatite". Biological apatite is defined as the "inorganic constituents of vertebrate bone and tooth" [4]. The main distinctions between biological apatite and synthetic HAp is their stoichiometry, morphology and crystal sizes [4]. Biological apatites known as non-stoichiometric, carbonate apatites and their Ca/P ratio is lower than stoichiometric pure HAp of which Ca/P ratio is 1.67. However, Ca/P ratio and carbon content of the bone apatites vary due to age or location [2].

Human bone has two types: compact and cancellous. Compact bone is known as dense or cortical bone because of its limited (5-10 vol%) porous structure where cancellous (trabecular or porous) has 50-90 vol % porosity. Cancellous bones are mostly at the ends of the long bones and inside of the flat, short and irregular bones. The macro-structure of the cortical bone can be divided into the parts as Haversian channel, canaliculi, Lacunae and Volkman's channel. Collagen fibers are formed

the lamellar sheets which have a thickness of 3-7μm and 4 to 20 lamella creates the osteon by arranging around Haversian channel. Canaliculi, lacunae and Volkman's channel provides the transportation of the metabolic substances [3].

The mechanical properties are related to the constituents of bone, collagen orientation, porosity and the degree of mineralization. Water content, mode, rate of loading and the direction of the applied load are also additional parameters that affect the mechanical properties of cortical bone [1]. Human bone exhibits high toughness with relatively high modulus due to its composite nature. The fracture toughness is provided by collagen and the fibrous tissues. On the other hand, stiffness of the bone is provided by the apatite crystals.

1.2.2. Background of material selection for bone replacement

Figure 1.1 displays the requirements for the metallic implants which are used in orthopedic applications. As indicated in this Figure; compatibility, mechanical properties and the manufacturing of these implants are significant parameters for the usage of these materials in surgical field.

The most commonly used metallic implants in biomedical applications are Co-based alloys, surgical grade stainless steels and Ti-alloys. Table 1.1 discloses some mechanical properties of these metals together with the mechanical properties of bone and synthetic HAp.

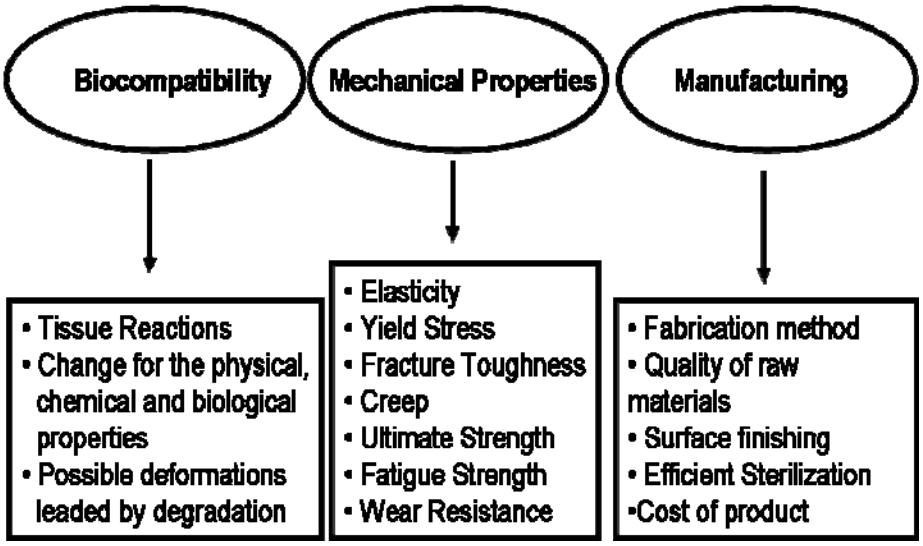

Figure 1.1 The requirements for metallic implants in orthopedic surgery (Adapted from ref. [5]).

1.2.2.1. Cobalt-based alloys

Co-based alloys, widely CoCr alloys, are offered as an alternative material for hard tissue applications. During 1920s, starlike CoCr alloy which was named as Stellite had been used and afterwards, Vitallium have been used as dental implants during 1930s.

For CoCr alloys, the solid solution of Co is formed up to 65%. Co has an hcp structure at room temperature whereas it has a fcc structure at temperatures higher than 460°C. There are three known Co-based alloy types depending on their processing techniques: Cast alloys, wrought alloys and hot isostatic pressed alloys. Fabrication of these alloys is also important in terms of their mechanical properties. Especially, wrought alloys display significantly improved properties. The addition of variety of elements such as Cr, Mo, Ni, Mn, W, Si also affects the mechanical

Table 1.1 Mechanical properties of metallic implants, bone and HAp

	Elastic Modulus (GPa)	Elongation at fracture	Tensile Strength (MPa)	Yield Strength (MPa)	Fatigue Strength (MPa)
CoCrMo	210[6]	8-9[7]	655[8]	450-890[6]	207-896[9]
Stainless Steel (316L)	193[6]	45[7]	485-860[8]	172-690[8]	200-800[9]
Ti6Al4V	120[6]	12[7]	860-965[8]	795-875[8]	598-816[9]
Cortical Bone	15[6]	1.49[7]	70-150[10]	n/a	100-200[9]
Cancellous Bone	0.3[6]	n/a	15[6]	n/a	n/a
Dense HAp	80–110[11]	n/a	38-48[11]	n/a	n/a

properties and transition temperature of these alloys. Especially, chromium addition improves the corrosion resistance of the coating where Mo provides Co-based alloys with finer grains and increased strengths. Elastic modulus of Co-based alloys, similar with stainless steels, is high which is an handicap for an optimum load share between bone and implant. This problem can lead to stress shielding according to elastic mismatch between bone and implant. The only advantage of Co-based alloys seem to be their wear resistance [8].

Biocompatibility of Co-based alloys is a serious concern since Co is known as a toxic element. Although toxicity of Co-based alloys can be tolerated by Cr addition, Co-based alloys are still less biocompatible than Ti alloys. Bouchard et al. reported

the carcinogenic effects of CoCrMo alloys according to in vitro tests on rats which displayed the inflammatory reactions occurred inside the living body after implantation and according to the loosening of the implant [12].

1.2.2.2. Stainless steels

Stainless steels were introduced after vanadium steels in the biomaterials field due to their improved corrosion resistance. 316 and 304 are austenitic stainless steels and 316 type stainless steels exhibit better corrosion resistance over 304 type because of molybdenum content in 316. Low carbon containing 316L stainless steels are more accepted for surgical needs since limited carbon content enables the minimization of susceptibility to sensitization [13]. Stabilization of the austenitic phase (γ, fcc) is owned by nickel in the composition. Moreover, it also progresses the corrosion resistance of the steel.

Mechanical properties of 316L stainless steels are sufficient enough for load-bearing applications and their properties are greatly dependent on the post-treatment processes. Soft stainless steels can be obtained by annealing whereas cold working can be applied for improved strength and hardness. The long scale values for the tensile, yield and fatigue strength of 316L are given in Table 1.1 which varies due to these post-treatment processes.

Corrosion resistance of 316L stainless steel is related to the passive film on the surface. Shih et al. reported the effects of surface oxide properties on corrosion resistance of 316L [14]. According to this study, amorphous oxide layer indicated as the best choice of anti-corrosive layer. Although they have high corrosion

resistance, it is possible to corrode these stainless steels in stressed or oxygen depleted areas. Although 316L type stainless steels offer high mechanical strength and corrosion resistance, high modulus and density limits their usage for biomedical applications.

1.2.2.3. Titanium alloys

Titanium and its alloys are seemed to be the most popular metals for surgical applications because of the combination of high strength, high fracture toughness, biocompatibility, lightweight and corrosion resistance. Commercially pure titanium has four grades depending on their impurity level. These impurities are mostly oxygen, nitrogen and iron. Titanium alloy is an allotropic material which has an hcp structure below 882ºC and a bcc structure above this temperature. Ti alloys, especially Ti6Al4V ($\alpha+\beta$) alloys, are known to be the most significant among the other bio-metals and there are two reasons for their wide usage: high mechanical properties and biocompatibility.

Table 1.1 discloses the mechanical properties of Ti6Al4V alloys. Mechanical properties of Ti alloys are strongly related to the purity of the metal, degree and type of alloying [15]. Tensile strength and yield strength of annealed Ti6Al4V alloys are ranged 860-965 MPa and 795-875 MPa respectively which are higher than both CoCrMo and 316L. On the other hand, elastic modulus is also an important parameter that can lead to bone resorption due to Wolff's Law if elastic modulus value of the implant is much higher than that of bone [16]. Even though none of the common metallic biomaterials' elastic modulus values are close to bone, Ti6Al4V alloys have the lowest elastic modulus among other Co-based alloys and stainless steels.

Fatigue resistance of the metallic materials should be classified in two groups: fatigue resistance of the material outside the body and inside the body. Apparently, fatigue resistance of all three common metallic biomaterials (Co-based alloys, 316L and Ti6Al4V) have sufficient fatigue strength [9] since the strength of the long bones, skull and other vertebral bodies are 100-200 MPa, 97 MPa, 1-10 MPa respectively [9]. However, these fatigue resistance values drop drastically in the long-term after the implantation *in vivo*. Adverse host-tissue response due to wear debris caused by the fatigue process was reported as an affecting issue for the fatigue strength of the implants [9]. These adverse reactions provoke the loosening of the metal.

Fretting fatigue, which is a damage formed by localized relative motion under vibratory load, is a delicate issue for biomaterials and it mostly occurs on the implant-cement interface for hip prosthesis [17]. This conveys the importance of oxide layer on the metal since the damage occurs due to the lack of quick repassivation reflex after the electrochemical breakdown of oxide layer [9].

Table 1.2 discloses the densities of Ti6Al4V, Co-based alloy and 316L. According to this table, the density of Ti6Al4V is lower than both Co-Cr alloy and stainless steel which provides better strength-to-weight ratio for Ti6Al4V.

Table 1.2 Density of common metallic implants [8].

Material	Density (g/cm^3)
Ti6Al4V	4.5
316L	7.9
CoCrMo	8.3

Adverse tissue reactions are critical issues for metallic implants which are caused by ion release and corrosion of the metallic substrate. Although vanadium was reported as a toxic element for the body, Ti alloys have advantages against Co-based alloys and stainless steels: Passive titania layer forms on the surface of the Ti alloy and this layer inhibits Ti^+ ion release to some degree in physiological conditions.

Bonding strength of Ti alloy-HAp interface is superior. Jaffe and Scott indicated that Ti6Al4V-HAp adherence is 33% more than Co-based alloys reasoned by additional chemical bonding besides mechanical integrity because of the apatite making ability of titania passive layer on Ti alloy [18].

Surface properties of Ti alloys greatly affect the cell activities on its surface in physiological condition. Long and short term human bone marrow cells in vitro and protein adsorption response according to surface roughness of Ti6Al4V alloys were investigated by Deligianni et al. [19]. According to their study, both cell attachment and proliferation were improved with surface roughness. Similar results were obtained for protein and fibrinoctin bounding. Surface topography, chemistry and

energy affect the proliferation and differentiation of osteoblast and osteoblast like MG63 cells.

1.2.3. Background of HAp coatings

1.2.3.1. Structure and properties of HAp

HAp is known as a member of calcium phosphate and apatite family. Calcium phosphates are ceramics which are classified due to their Ca/P stoichiometric ratio where apatite family's specific order of chemical formula is important. These ceramics are widely used for medical applications since most of the members of calcium phosphate family are biocompatible, bioactive and bioresorbable.

On the other hand, the order of the chemical formula determines the type of the apatite and the specific formula for apatites and substitute elements are outlined [2].

$$X_{10}(YO_4)_6Z_2$$

X: Ca, Sr, Ba, Cd, Pb, Mg, Na, K…

Y: P, CO_3, V, As, S, Si, Ge, Cr, vacancies…

Z: OH, CO_3,F, Cl, Br, vacancies…

As it was indicated before, synthetic hydroxyapatite mimics the mineral phase of the bone. This resemblance causes the ability of direct bonding to bone which is called as bioactivity [1]. The bioactive and osteoconductive properties of HAp

provides the preferential proliferation and differentiation of osteoblasts, bone forming cells, resulting with the production of collagen and natural apatite mineral on HAp [20]. Bioinert materials, like metals and some ceramics, need to be surface treated to form apatite layer on their surface for gaining such bioactive properties. HAp can also be resorbed by body. The bioresorption of HAp occurs throughout the ingrowth of bone during healing period. However, this resorption occurs in the case of low crystallinity; in other words, HAp calcined at high temperatures does not show bioresorption and they are more stable.

1.2.4. HAp coatings

HAp coated metal implant system provides the best combination of biocompatibility and mechanical properties. HAp coatings offer high degree of bone attachment, improved bone formation and rapid stabilization. According to Garcia and Doremus' study, foreign body reactions, formation of fibrous tissue and structural changes were not evident at the apatite-bone interface due to the electron microscopy observations from HAp-bone attachment spot [21]. This study discloses that the HAp-bone interface is a perfect match in terms of bone attachment leading to accelerated hard tissue formation [21].

As indicated in the previous sections, vanadium is a concern for Ti6Al4V alloys because of potential risk of ion release to the living environment. This problem can be overcome by HAp coatings. HAp coatings minimize the release of these harmful ions to the body. The advantages of HAp coatings can be listed as:

- Enhancement of bone formation,
- Accelerated and stronger bonding between the implant and surrounding tissues,
- Reduction of potentially harmful metallic ion release,
- Establishment of strong interfacial bonds with titanium and this has been attributed to some mechanical bonding between HAp and the titanium substrate.
- Enhancement of the osteoconductive properties of the bridging bone tissue.
- Providing the rapid stabilization of the implant.

Microstructural and mechanical properties of HAp affect the long-term performance of HAp coatings *in vivo* and *in vivo*. Bioresorption rate, crack and porosity, decomposition of HAp related to the processing issues, amorphous phase content of HAp, roughness of the coating, delamination and disintegration are critical issues for long-term stability of HAp *in vivo*. Critical properties of HAp coatings for hard tissue applications can be divided into four categories:

(i) Mechanical properties
(ii) Bonding strength
(iii) Bioresorption rate
(iv) Bone formation (Bioactivity and Osteoconductivity)

1.2.5. Processing techniques for HAp coatings

HAp coatings on titanium alloy can be produced by several techniques such as plasma spraying, sputtering, electrophoretic deposition, electrochemical deposition and sol-gel. The critical issues that determines the efficiency of the coating technique is the dissolution rate, bonding strength and morphology of the final coating. These issues dependent on the chemical composition, crystal structure,

crystallinity, porosity, particle size, surface area of the HAp powders and coatings. Thickness of the coatings and parameters for each coating technique also greatly affect these parameters. This section provides a brief informative explanation for each technique. Table 1.3 shows the approximate thicknesses of HAp coatings that can be produced by different techniques and the advantages and limitations for each method.

1.2.5.1. Plasma spray technique

Plasma spray technique is the most widely used industrial scale manufacturing method in making HAp coatings. Figure 1.2 discloses the schematic diagram of the gas tunnel type plasma spraying method. The coating is achieved by injection of HAp powders into a plasma flame (up to 30000 K) and spraying of molten or heat softened HAp feed onto a surface of the metal substrate by the help of a carrier gas such as argon. The process ends with the fast cooling of the coating.

Three main parameters affect the quality of HAp powders coated by plasma praying: feed powder properties, implant metals and spray parameters [22]. Purity, crystallinity, microstructure, porosity and roughness of the HAp feed powders determine the overall quality of plasma sprayed coating [22]. Generally, pure and highly crystalline HAp powders are selected as a feed powder. However, high processing temperatures for plasma spray method lead to decomposition of HAp powders and formation of additional phases such as tri-calcium phosphate, tetracalcium phosphate, calcium oxide and amorphous phases during cooling. These results low crystallinity for the final HAp coating layer and significantly increases the dissolution rate of HAp in physiological conditions.

Table 1.3 Thickness values, advantages and disadvantages of distinct processing techniques for HAp coatings [22].

Technique	Thickness	Advantages	Disadvantages
Thermal spraying	30–200 μm	High deposition rates; low cost	Line of sight technique; high temperatures induce decomposition; rapid cooling produces amorphous coatings
Sputter coating	0.5–3 μm	Uniform coating thickness on flat substrates; dense coating	Line of sight technique; expensive time consuming; produces amorphous coatings
Dip coating	0.05–0.5 mm	Inexpensive; coatings applied quickly; can coat complex substrates	Requires high sintering temperatures; thermal expansion mismatch
Sol–gel	< 1 μm	Can coat complex shapes; Low processing temperatures; relatively cheap as coatings are very thin	Some processes require controlled atmosphere processing; expensive raw materials
Electrophoretic deposition	0.1–2.0 mm	Uniform coating thickness; rapid deposition rates; can coat complex substrates	Difficult to produce crack-free coatings; requires high sintering temperatures
Biomimetic coating	< 30 μm	can form bonelike apatite; can coat complex shapes; can incorporate bone growth stimulating factors	Time consuming; Requires replenishment and a constant of pH of simulated body fluid
Electrochemical deposition	80 μm	coat complex shapes; uniform coatings	constant pH for the solution of electrolytes

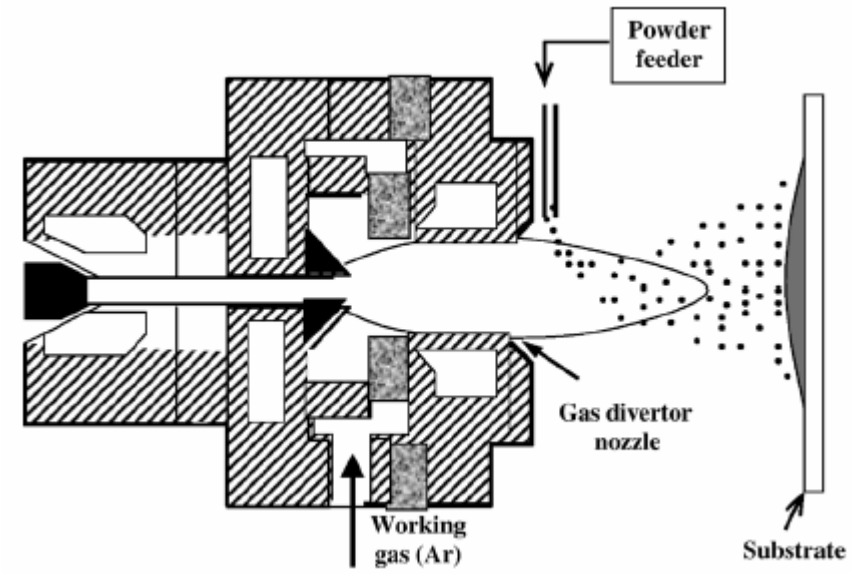

Figure 1.2 Schematic illustration of gas tunnel type plasma spraying torch [23].

The coating quality is also affected by the microstructure and porosity of HAp powders. Powders with different pore sizes can cause the formation of well-flattened splats, accumulated splats, spheroidized particles, partially- or unmelted particle [22]. Unmelted powders and highly porous powders lowers the bonding strength of coating and can lead to delamination of the coating [22].

Microstructure and phase composition of HAp coatings are also dependent on the spray parameters. Dyshlovenko et al. indicated that electric power, spraying distance, and carrier gas flow rate are the most important factors for crystalline HAp content of the coating [24]. Dyshlovenko et al. added the information that higher values for electric power and gas flow rate can lead to a formation of deformed splats with low crystallinity which diminishes the quality of the coating [24]. Similarly, Tsui et al. reported that the ideal properties for HAp coatings such as low porosity, high cohesive and adhesive strength, a high degree of crystallinity, high chemical purity and phase stability can be achieved only by the manipulations on spraying parameters [25].

Today, plasma spray can be considered almost the only well-accepted industrial manufacturing method. However, it does not offer a perfect HAp coating. Apparently, limitations of plasma spraying method is related to the high processing temperature and following rapid cooling affecting the phase purity, crystallinity and thus, dissolution rate of the HAp coatings. Moreover, high thickness of the plasma sprayed coatings decrease the bonding strength of the coating.

1.2.5.2. Electrophoretic deposition

In electrophoretic deposition, charged HAp particles, dispersed or suspended in a liquid medium are attracted and deposited onto a conductive substrate of opposite charge with an application of a DC electric field. There are two types of electrophoretic deposition dependent to the electrode on which the deposition occurs. When the particles are positively charged, the deposition happens on the cathode and the process is called cathodic electrophoretic deposition. The deposition of negatively charged particles on positive electrode (anode) is termed as anodic electrophoretic deposition. Figure 1.3 demonstrates the electrophoretic deposition.

Deposition time, applied voltage, concentration in solid suspension and the conductivity of the substrate are the parameters affecting the efficiency of the electrophoretic deposition process [26]. There are also some factors affecting the quality of the coating such as: particle size and zeta potential of HAp powders, dielectric constant of liquid, conductivity of the suspension and suspension viscosity [26]. Electrophoretic deposition is a quick process providing high reproducibility in limited time and it is also a low cost technique. On the other hand, poor adherence of the HAp coatings is a limiting issue for electrophoretic

deposition. The process also requires high sintering temperatures for improved bonding strength and thus, it is barely possible to obtain crack-free coatings and decomposition of HAp which leads higher solubility can also be evident [27].

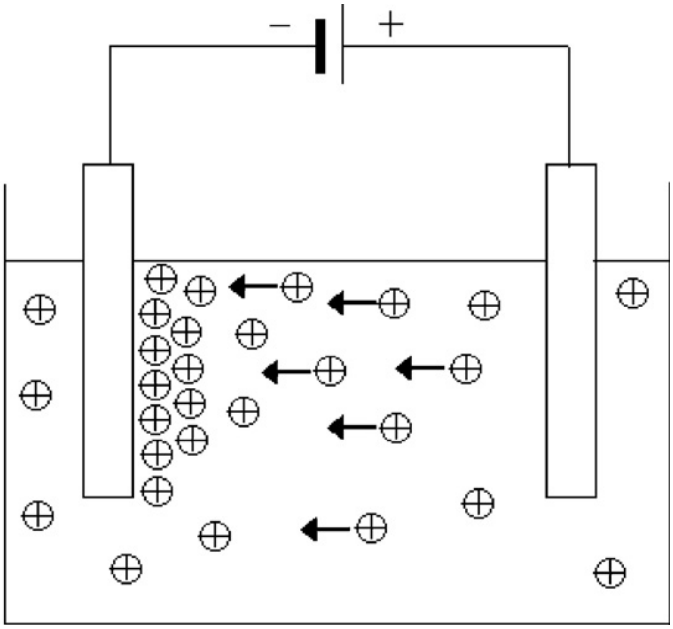

Figure 1.3 Schematic illustration of electrophoretic deposition [26].

1.2.5.3. Ion beam sputtering

Sputtering is a physical thin film deposition process covering the bombardment of a target material with an ion beam in a vacuum chamber. This process lacks of providing the energy to recompose Ca and P ions after sputtering. Thus, the need of post-treatment for sputtered HAp coatings is evident where 500 ºC is enough to provide the energy for HAp coating. Although, sputtered coatings exhibit high bonding strength, non-stoichiometry (Ca/P =1.67) for the coating, time consumption and high cost of the process are their limitations.

1.2.5.4. Electrochemical deposition

The procedure of electrochemical deposition for HAp powders is the deposition of the Ca and P ions from HAp by the driving force of the applied potential. The process is followed with the calcination of coating due to improve the bonding strength of the coatings. Although, this technique offers coating complex shapes and uniform coatings, it is hard to maintain constant pH for the solution since electrolytes continuously change during electrochemical deposition [28, 29]

1.2.5.5. Biomimetic deposition

Biomimetic deposition is simply a process of formation of apatite layer by the immersion of the substrate into the physiological fluid (simulated body fluid, SBF) at physiological temperature. Bioactive surface functionalization (BSF) schemes allow surface modification on the surfaces of such tough materials in situ to produce bioactive ceramic phases. The chemical surface modification of titanium metal [30] is an excellent example of BSF. Immersion of titanium to NaOH conveyed the formation of bioactive titanate surface. In physiological fluid, the overall reactions by Ca ion release cause the formation of apatite layer on titanium surface. Biomimetic deposition method gains interest since this technique offers low deposition temperatures and well step coverage. However, this process is time consuming and hard to adjust pH of the physiological fluid.

1.2.5.6. Sol-gel method

Sol-gel method is a low temperature technique to prepare inorganic materials in different forms. Figure 1.4 displays the illustration of sol-gel method and possible final products by this method. The preparation, gelation of sol and the removal of

the liquid is involved in this preparation process. The definition of a *sol* "is a stable suspension of colloidal particles within a liquid or a solution of polymer molecules" [31]. The solid particles should be denser than the liquid for a sol to exist. These solid particles form colloids and these colloids are ranged between 1-1000 nm.

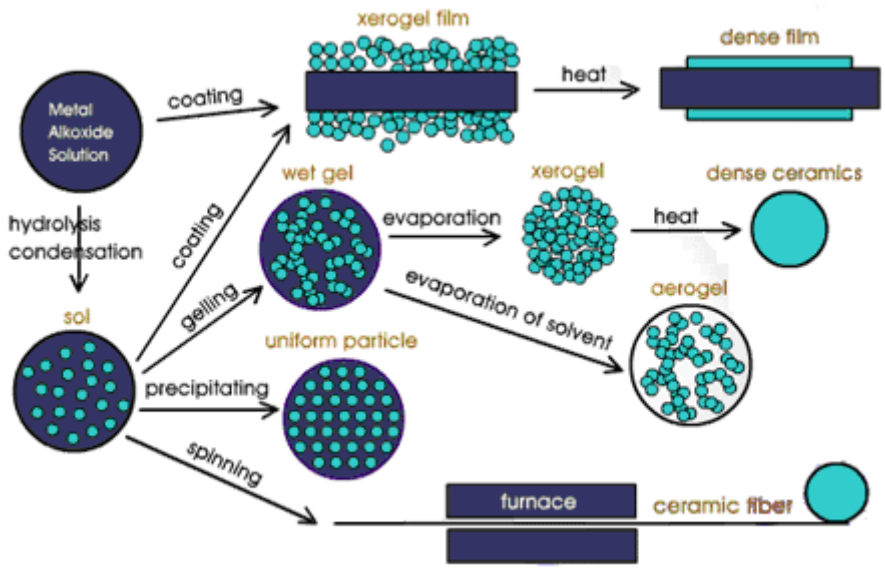

Figure 1.4 Schematic illustration of sol-gel method and its final products [32].

The term *gel* is "a porous 3-dimensionally interconnected solid network that expands throughout a liquid medium container" [33]. There are two different processing ways called colloidal and polymeric route. For the colloidal route, the gel is made of colloidal sol particles whereas for the polymeric route, the gel is made of sub-colloidal chemical units (polymeric chains).

Hydrolysis, condensation, gelation, aging, drying and sintering of the dried gel are the steps for the sol-gel process. As a precursor, inorganic salts or metal alkoxides $M(OR)_X$ are used. In hydrolysis step, precursors are hydrolyzed by addition of water or related alcohol depending on the type of precursor. Hydrolysis is followed

by condensation that forms bulk or films. These by products are than calcined to achieve the final ceramic by removing organic groups from the structure.

Sol-gel process has advantageous when compared to the other coating techniques. High purity and stoichiometric products can be achieved by sol-gel process [34]. The temperature needed during this process is limited and this provides avoiding the decomposition problems as it can be seen in thermal sprayed coatings [34]. By sol-gel process, it is comfortable to mix the constituents in molecular level and by means of this homogeneous films can be produced. Crack problem for the films produced by sol-gel method can be minimized.

Sol-gel method can easily be manipulated by the alteration of precursors chemically during the process and control of the system can be achieved over the rates of hydrolysis and condensation. Therefore, it is possible to obtain variations in the porosity for the final product. In such systems, porous network can be a template for heterogeneous nucleation for the growth of biological apatite layers [35]. Subsequent steps, aging and drying, can also be regulated for the desired composition and mechanical strength.

Addition of different functionalities by the incorporation of the organic and biomolecules in sol-gel network, incorporation of fluorine for hydrophobicity, silver for antimicrobial benefits and variety of polymer additives for mechanical property modifications are some instances for sol-gel derived added functionalities. Sol-gel process also offers wide range of final product types. Powders, fibers, thin films, bulk amorphous and monolithic solids can be acquired by this technique [34]. For coatings, coating process is also variable for the substrates and spin and dip coating methods are to be used in sol-gel process. Therefore, coatings on complex

substrates can easily be obtained. In addition to these advantages, the required set up is fairly inexpensive.

There are also some limitations of sol-gel technique. The precursors are usually expensive and sensitive to moisture. When careful aging and drying are required, sol-gel process is a time consuming process.

1.2.6. Sol-gel derived HAp-based coatings: Process parameters affecting the coating properties

You et al. studied the influences of heating conditions and surface roughness on HAp coatings derived by sol-gel method [36]. They stated that heat treatment conditions and surface roughness play important role for the microstructure and the homogeneity of the coating. It is observed that heating the coatings with a slow rate and for a longer time causes more uniform and dense surface. Moreover, higher crystallinity can be reached by this way. You et al., on the other hand, prepared Ti6Al4V substrates which are made by alumina grit blasting for the observations of the effects of surface roughness of the coating [36]. It is observed that 20μm sized alumina grit blasted substrates have more smooth and homogeneous surfaces than the 100μm sized alumina grit blasted substrates. Moreover, 20μm sized alumina grit blasted substrates showed fewer cracks. Rougher surface can be bonded to higher volume of HAp and it can cause increased cracks according to the shrinkage during drying and heat treatment. You et al. [36] achieved the solutions that the lower surface roughness, the higher uniformity and the fewer cracks can be obtained. Smoother surface also cause less thermal stress.

Chai et al. worked on the critical aging time for hydroxyapatite coatings. They followed the alkoxide route to produce HAp [37]. It is reported that, without aging

calcium oxide phase also exist with HAp in the structure [37]. However, when the solution is aged more than 24 h, the existence of phases different than HAp can be avoided. They also stated that the solution should be aged until preventing the unexpected weight loss between 680-750°C upon heating. Chai et al. also studied a change for the aging environment by aging the solution in the nitrogen environment [37]. However, they observed that there was no noticeable change because of the environment.

Incorporation of different materials is allowed by sol-gel route to enhance the properties of HAp coatings. Kim et al. worked on fluor-hydroxyapatite (FHA) coatings [38]. They investigated that the FHA films showed crystalline apatite films and increased crystallinity by the increment of the temperature. The bonding strength of the FHA films increased from 20MPa at 400°C to 70MPa at 500°C. When it is compared to regular HAp coatings, FHA showed slower dissolution in the saline solution and from the cell behavior perspective, it is stated that MG63 cells had the similar proliferation behaviors both on FHA and HAp coatings.

1.2.6.1. Sol-gel derived HAp-titania hybrid coatings

HAp-titania hybrid coatings exhibit superior features in mechanical, chemical and biological point of view as it was indicated. Table 1.4 displays bonding strength results for HAp and HAp-titania coatings from literature. This table also shows the mechanical properties of some HAp coatings with titania incorporation.

Titania insertion to the HAp coatings extremely affects the adherence especially for the HAp-Ti alloy interface. Double layer or hybrid coating approaches were studied for the investigation of the effects of these coatings on the bonding strength [39-41].

Although the processing technique and coating thickness are important, the enhancement for the interfacial adherence is evident for these coatings.

Table 1.4 Bonding strengths of some HAp and HAp-titania hybrid coatings.

Coating	Method	Calcination Temp.(°C)	Number of Layers	Substrate	Bonding Strength (MPa)	Ref.
HAp-titania	s-g*	500	4	Ti6Al4V	39.8±3.75	[41]
HAp	s-h	500	n/a	Ti	20	[39]
HAp-titania(70%)	s-g**	500	n/a	Ti	53.9	[39]
HAp-titania (Buffer layer)	s-g	400	2	Ti	35	[39]
HAp-titania (Buffer layer)	s-g	500	2	Ti	55	[39]
HAp	s-g	400	1	Ti	22	[39]
HAp	s-g	500	1	Ti	40	[39]
HAp + (TCP,CaO, TTCP)	Plasma Spray	500	n/a	Ti	6-26	[3]

s-g: sol-gel

* mechanical mixing method

** i*n situ* formation of HAp and titania phases

Besides mechanical improvements, HAp-titania hybrid coating also enhances biological performance. Peltola et al. studied the biomimetic technique for the formation of HAp on the titania layer on Ti alloy [42]. In this study, it is explained that titania layer was attracted calcium and phosphorus from simulated body fluid (SBF) which indicates the bioactivity of titania coatings. Thus, bioactivity of HAp increases with the reinforcement of titania in the structure and this enhances the bone ingrowth and cell transportation. Similar findings were reported by Balamurugan et al. illustrated that the existence of titania in the coating increases the osteoblast adhesion and induces the growth of cells [43]. They observed that HAp-titania hybrid coatings do not exhibit cytotoxic effect and on the other hand these coatings allow the differentiation of osteoblasts which is important for the remodeling of bone. Improvement for the corrosion resistance is also one of the significant features of HAp-titania coatings. Presence of Ti-OH bond reveals the increment in the corrosion resistance. HAp-titania hybrid coatings can be obtained according to two different processing routes by in situ formation or mechanical mixing:

(i) Direct (in-situ) formation of HAp-titania coatings: In this route, first calcium and phosphorus precursors dissolved in alcoholic and/or water solutions in stoichiometric proportions. This solution is then aged together with titania sol leading to in-situ formation of HAp together with titania network. $Ti(OBu^n)_4$ or $Ti(OPr^i)_4$ is common starting alkoxides for in situ formation route of HAp-titania hybrid coatings. Ti precursor hydrolyzes in butanol, propanol or ethanol solution depending on the precursor preference. Functionally grading coatings (from 100%TiO_2-0%HAp to 0%TiO_2-100%HAp) can be achieved by adjusting the addition of HAp solution while mixing with titania sol. By this route, coating with a dense and clear interface can be produced, however more studies about improving the bonding capability of HAp-titania hybrid coatings are to be done. Lim et al. indicated that films with a thickness at nanoscale are available by this route [60].

(ii) Mechanical mixing of HAp suspension with titania sol: This route is simply mechanical mixing of HAp powders and titania gel. For this route titanium precursors are hydrolyzed and condensed in alcoholic solution and mixed with the HAp powders. Titanium oxopolymers are widely used for TiO_2 sols and the most known oxopolymers are n-butoxide $Ti(OBu^n)_4$ and iso-propoxide $Ti(OPr^i)_4$. During or after polymerization reactions, HAp powders in a liquid media are added to the titania matrix solution. Milella et. al. studied the production of HAp-titania hybrid coatings by this route [41]. They have reported that this route shows a titania matrix encapsulating the HAp particulate. Chemically clean and homogeneous coatings can be achieved. Coatings with rough surface and the porosity can be achieved from nano-sized pores to none. In Milella et al.'s study the size of the pores are ranged 250-300 nm and the thickness of the coating is in micron scale [41]. Functional grading is also available by this route. By adjusting the composition of titania sol and HAp precipitates, each layer can be coated with different compositions. Limitations of this route are the formation of cracks after drying and heat treatment.

1.3. Objective of the thesis

The general objective of this study was to establish the processing routes for the development of crack-free, uniform HAp-titania hybrid coatings on Ti6Al4V alloy substrates. Titania component has been obtained with typical sol-gel reactions by direct hydrolysis and condensation of an organic metal alkoxide. HAp powder was first synthesized by aqueous precipitation methods and introduced to the sol-gel derived titania matrix by mechanical mixing methods.

The work conducted in this thesis is composed of two major tasks. *In the first part*, phase pure HAp powders of controlled size and chemical identity have been synthesized by classical precipitation methods by using various precursors of calcium and phosphate salts or other sources, such as calcium salts-ortophosphoric acid combinations. The details of synthesis methods have been outlined and discussed, complete characterization, i.e. phase identification and morphology of HAp powders produced by various precipitation reactions have been performed.

The second part focuses on processing of the HAp-titania hybrid coatings. Titania matrix was produced by sol-gel method by the hydrolysis and condensation of Ti alkoxide. The involvement of synthesized HAp powders to the sol was the next step in the processing of the sol-gel derived hybrid coatings. This part mostly focused on physical and morphological identifications of the coatings and modifications on coating properties as a function of coating layer number, the chemical formulation of the coating solution, HAp powder size, calcination temperature, and dip coating process parameters such as withdrawal rate. The effects of these parameters on the chemical identity, morphology, thickness and microstructure of the coatings have been investigated.

CHAPTER 2

MATERIAL CHARACTERIZATION AND EXPERIMENTAL PROCEDURE

2.1. Characterization of HAp powders and HAp-titania coatings

2.1.1. X-Ray diffraction (XRD) analysis

XRD measurements were employed for the phase analysis of HAp powders and HAp-titania hybrid coatings. Analyses were performed by Rigaku X-Ray diffractometer (Ultima D/MAX2200/PC). CuK_{α} radiation was used as an X-ray source at 40 kV. The scan speed was 2°/min. HAp powder samples were scanned over from 20º to 40º in 2θ and HAp-titania coatings from 20º to 60º.

2.1.2. Scanning electron microscopy (SEM) analysis

Morphology of HAp powders and HAp-titania coatings were studied by SEM. SEM analyses were performed by using a JSM-6400 Electron Microscope (JEOL), equipped with a NORAN System 6 X-ray Microanalysis System and Semafore Digitizer. Powders and coatings were coated by Au-Pd alloy by an HUMMLE VII sputter coating device (ANATECH).

2.1.3. Fourier transform infrared spectroscopy (FTIR) analysis

Fourier transformed infrared (IR) spectra analyses were performed to determine the chemical structure of HAp powders according to measured bond vibration frequencies of phosphate (PO_4^{-3}), hydroxyl (OH^-), carbonate (CO_3^{-2}) and hydrogen phosphate (HPO_4^{-2}) groups. FTIR analyses were performed by Bruker IFS 66/S F Model Spectrometer and the range was chosen between 400-4000 wavenumbers (cm^{-1}).

2.1.4. Coating thickness measurement

Dektak 6M Profilometer was employed for the thickness analyses of the coatings. Dektak 6M Profilometer, which is a surface profile instrument that provides the data by vertical detection of the stylus with horizontal movement across the sample's surface. Scan length of the stylus for the coatings was selected as 3000 μm between the spot from non-coated part to the spot from the coated part and the duration was 30 s.

2.2. Materials

All the chemicals used for the synthesis of HAp powders by precipitation method together with the sol-gel precursors are listed in Table 2.1.

Table 2.1 List of the chemicals used in the thesis, and their sources.

Material	Formula	Source	Molecular Weight (g/mol)
calcium nitrate tetra hydrate	$Ca(NO_3)_2 \cdot 4H_2O$	Merck	236.2
calcium carbonate	$CaCO_3$	Kale Seramik, TURKEY	100
di-ammonium hydrogen phosphate	$(NH_4)_2 \cdot HPO_4$	Merck	132. 0
ortho-phosphoric acid	H_3PO_4	Merck	98.0
Ti-isopropoxide	$C_{12}H_{28}O_4Ti$	Sigma-Aldrich	284.3
n-propanol	C_3H_8O	Sigma-Aldrich	60
acetyl acetone	$C_5H_8O_2$	Fluka	100.1
nitric Acid	HNO_3	Merck	63
ethanol	C_2H_5OH	Riedel-de Haen	46

2.3. Experimental procedure

2.3.1. Synthesis of hydroxyapatite (HAp) powders

The first part of experimental work conducted in this thesis is the synthesis of HAp powders by aqueous chemical routes. The objective of this part is to synthesize phase pure HAp powders of tailored physical properties – essentially morphology and size- by precipitation techniques using a variety of calcium sources of different solubility values and different phosphorus sources. Accordingly, three different precursor couples for calcium and phosphorous were used to obtain HAp powders. Figure 2.1 shows the flow charts for the different synthesis routes followed in making HAp powders. Experimental details for HAp powders synthesis are outlined in the following section.

2.3.1.1. Synthesis of HAp-I: Experimental details

The first route is modified from a previous work [44]. This route is simply mixing calcium and phosphate containing slurries in stoichiometric ratio leading to HAp. $Ca(OH)_2$ solution and H_3PO_4 (Merck) were used as a precursor couple. $Ca(OH)_2$ was obtained from CaO derived by calcination of $CaCO_3$. The chemical reactions for this route are shown below.

$$CaCO_{3(s)} \rightarrow CaO_{(s)} + CO_{2(g)} \quad (2.1)$$

$$CaO_{(s)} + H_2O_{(aq)} \rightarrow Ca(OH)_{2(s)} \quad (2.2)$$

$$10Ca(OH)_{2(aq)} + 6H_3PO_{4(aq)} \rightarrow Ca_{10}(PO_4)_6(OH)_{2(s)} + 18H_2O_{(aq)} \quad (2.3)$$

As it can be seen from Equation (2.1), the first step was obtaining CaO from $CaCO_3$ (from Kale Seramik Çanakkale Kalebodur Sanayi, A.Ş., Çan, Türkiye) and then hydrated calcium oxide was used as aqueous calcium source. In making $Ca(OH)_2$, first 100 g of $CaCO_3$ was calcined at 1010 ºC for 2.5 h to obtain CaO. Then, $Ca(OH)_2$ was prepared by mixing CaO slurry with distilled (DI) water. The slurry was dried at 60 ºC for 2 hours to obtain $Ca(OH)_2$ powder and ground afterwards.

For the preparation of HAp powders, 58.8 grams of $Ca(OH)_2$ and 27.3 ml of H_3PO_4 (85.6% wt.) were mixed with 1000 ml of DI water separately. First $Ca(OH)_2$ slurry was stirred vigorously, and dropwise addition of H_3PO_4 solution into this was accomplished in almost 2 h. The mixture was aged for 21 days. During this period, samples were collected for XRD analyses at constant time intervals to examine the precipitating phases. At the end, suspension containing the precipitates was vacuum filtered and dried at 80 ºC for 2 h. Following the precipitation; the solid powder products were calcined at 1000 ºC for 3 h. Characterization of the powder products was performed by using XRD, SEM and FTIR.

2.3.1.2. Synthesis of HAp-II: Experimental details

In the second route, an original recipe was followed and two solid powders; $CaCO_3$ (Kale Seramik) and $(NH_4)_2HPO_4$ (Merck) precursor couple was used. These two precursors have relatively lower solubility values compared to those in the first route. The chemical reaction for the formation of HAp with these precursors is given by,

$$10CaCO_{3(s)} + 6(NH_4)_2HPO_{4(s)} \rightarrow$$

$$Ca_{10}(PO_4)_6(OH)_{2(s)} + H_2O_{(aq)} + CO_{2(g)} \qquad (2.4)$$

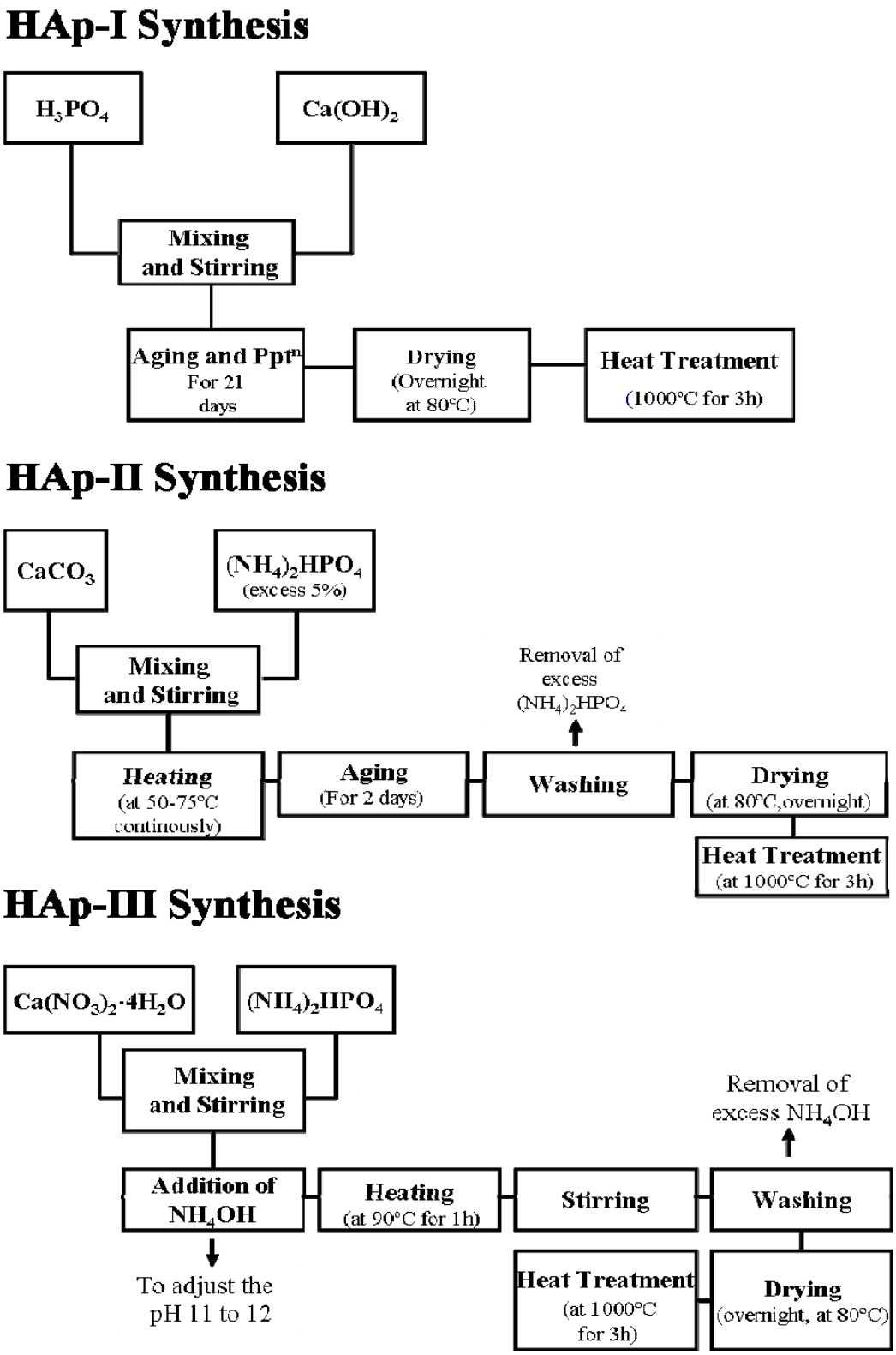

Figure 2.1 Flowcharts for the synthesis process of HAp-I, HAp-II and HAp-III.

First, 0.5 moles $CaCO_3$ and 0.3 moles of $(NH_4)_2HPO_4$ with 5 wt% excess amount were prepared separately in same the amount of DI water. Excess amount of $(NH_4)_2HPO_4$ was added to accelerate the dissolution of barely soluble $CaCO_3$ powders. $(NH_4)_2HPO_4$ solution was poured to the $CaCO_3$ suspension. The mixture was heated to 70ºC when it was being stirred vigorously. The pH values were recorded during preparation. During aging, samples were collected for XRD analyses at constant time intervals to investigate the precipitating phases. After aging for 2 days, the aqueous suspension was filtered to recover the solid precipitates and the excess phosphate was removed by DI washing. Then, the solid product was dried at 80 ºC for 2 h. The calcination was again done at 1000 ºC for 3 h. Then, complete characterization of the powder products was performed by using XRD, SEM and FTIR for as-precipitated and calcined samples.

2.3.1.3. Synthesis of HAp-III: Experimental details

The third route was followed according to Jarcho et. al.'s study [45]. This time a solid calcium precursor of relatively higher solubility; namely; $Ca(NO_3)\cdot 4H_2O$ (Merck) was used with $(NH_4)_2HPO_4$ (Merck). The chemical reaction for this route is given in Reaction (2.5).

$$10Ca(NO_3)_2\cdot 4H_2O_{(s)} + 6(NH_4)_2HPO_{4(s)} + 8(NH_4OH)_{(aq)} \rightarrow$$

$$Ca_{10}(PO_4)_6(OH)_{2(s)} + 20(NH_4NO_3)_{(g)} + 40(H_2O)_{(aq)} \qquad (2.5)$$

Initially, 0.5M $Ca(NO_3)\cdot 4H_2O$ and 0.3M of $(NH_4)_2HPO_4$ were prepared in 50ml of DI water separately and stirred vigorously. pH values of Ca and P solutions adjusted to pH=11-12 by the addition of NH_4OH(Merck). According to previous knowledge, octacalcium phosphate ($Ca_8H_2(PO_4)_6\cdot 5H_2O$, OCP) and dicalcium phosphate

dihydrate ($CaHPO_4 \cdot 2H_2O$, DCPD) involve in the reactions at high pH values with HAp phase and they may also precipitate during these reactions [46]. Nancollas and Zhang also showed that during the synthesis of HAp between the pH values 10 to 11, octacalcium phosphate forms as an intermediate phase [46]. Most likely, OCP transfers into amorphous calcium phosphate (ACP), then to calcium-deficient hydroxyapatite($Ca_{(10-x)}(HPO_4)_x(PO_4)_{(6-x)}(OH)_{(2-x)}$, CDHAp) and at last to HAp. HAp becomes the most stable and the precipitating phase only at extremely alkaline conditions, i.e. pH>11. After initial pH adjustment, a milky solution is formed by dropwise addition of calcium containing solution to phosphorus containing solution. Throughout this addition, the pH of the solution was kept constant at the range of pH=11-12 by continuous NH_4OH addition. After adding all the components, the final solution was stirred for 2 h after adjusting the pH value 11-12. Then, the solution was heated to 90 °C on a hot plate and stirred for 1 h at this temperature. The pH value was 6.50 after heating. After 1 h, the batch was cooled down to room temperature by natural cooling in air and stirred overnight (approximately 20 h). The solution was filtered and washed continuously with water to remove any excess NH_4OH. The filtered cake was dried at 80 ºC overnight and calcined at 1000 °C for 3 h. Again, complete characterization of the resultant powder was performed by using XRD, SEM and FTIR for as-precipitated and calcined samples.

2.3.2. Preparation of HAp-titania (TiO_2) coating solutions

In this section, experimental methods for preparation of HAp-titania coatings are introduced. Pretreatment procedures of the Ti6Al4V substrates, details of dip coating process and heat treatment procedures applied after the coating process are also discussed in this section.

In an attempt to obtain HAp-titania coating solutions, several procedures have been adapted from the available literature. As a general processing approach, HAp powders synthesized according to procedures explained in section 2.3.1 were introduced to titania sol-gel formulations during gelling step to obtain hybrid sols that can be applied to the metal substrates.

In hybrid sol-gel coating preparation studies the major processing challenge was determination of the titania sol-gel formulation which leads to a formation of glassy continuous crack-free coating layer. Two different aqueous based sol-gel approaches named as Hybrid-I and Hybrid-II had been tried to obtain a sol-gel formulation leading to a uniform and crack free coating on the cleaned metal substrates. In both case Ti-isopropoxide ($Ti[OCH(CH_3)_2]_4$) was titania forming organic precursors, but a combination of different types/amount of organic solvents have been employed. Preparation of the coating solutions were performed at room temperature. Figure 2.2 displays the flow chart of the sol-gel routes for different formulations (Hybrid I and Hybrid II).

2.3.2.1. Preparation of Hybrid-I sol

A modified recipe from Nakajima et. al's study [47] was followed. This particular formulation aims obtaining approximately 10 vol % titania yield compared to the total volume of the overall solution. The remaining volume is the organic precursors present initially or organic by-products forming during the gelation process, which are removed from the system later on during drying and calcination. Table 2.2 lists the relative amounts of the precursors used in the Hybrid-I formulation

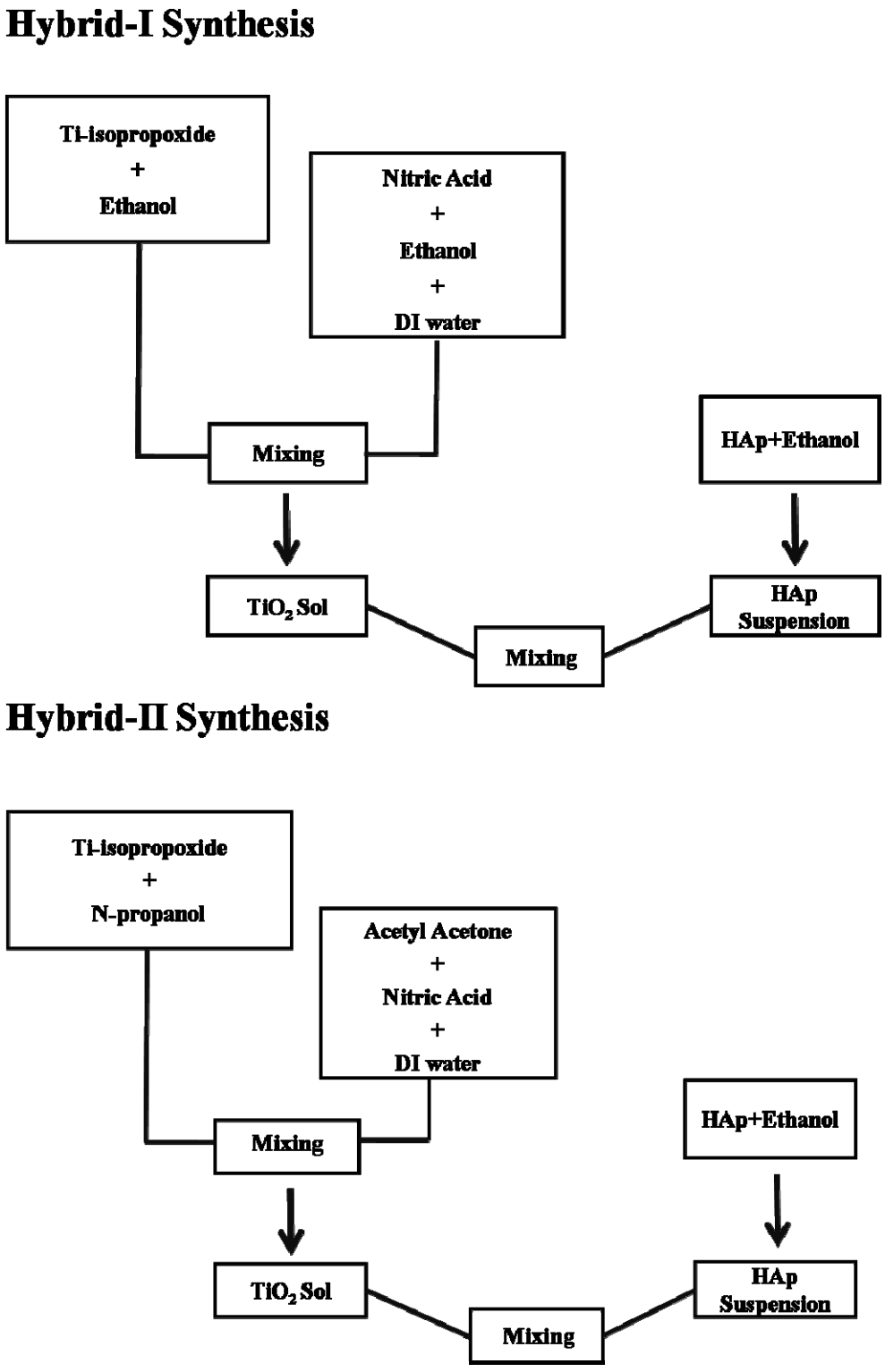

Figure 2.2 Sol-gel processing flowcharts of HAp-titania coatings for Hybrid-I (top), and Hybrid-II (bottom) formulations.

Table 2.2 The relative amounts of the chemicals to prepare Hybrid-I sol.

Material	Mole
Ti-isopropoxide	1
ethanol	12
nitric acid	0.25
water	1
HAp	0.5

Two solutions were prepared separately to obtain final titania sol. First, in glass beaker, 3.25 ml Ti-isopropoxide was dissolved in 3.6 ml ethanol under vigorous stirring. The pH of this solution was around pH=5. In a different beaker 0.18 ml nitric acid, 16 M 3.6 ml ethanol and 0.18 ml DI water were mixed by a magnetic stirrer. This solution was strongly acidic with a pH<1. Then, this acidic solution was added into the Ti-isopropoxide: ethanol solution to catalyze the sol-gel reactions. The final mixture was mixed for 30 min and the pH was measured as pH<1. On the other side, 1g HAp powders were added to 0.323 ml of ethanol solution for the preparation of the powders for incorporating them to the titania solution. The prepared HAp suspension was poured to the titania sol to obtain the HAp-titania hybrid solution. Typically, the HAp-titania hybrid sol was applied to the metal substrates within 1 h of aging.

2.3.2.2. Preparation of Hybrid-II sol

In preparation of this coating sol, the work from Milella et al. has been adapted [41] . This time both acetyl acetone and n-propanol were used together with the all precursors used in preparation of Hybrid-I. Acetyl acetone, an organic stabilizer, is added as a chelating agent to slow down hydrolysis of the extremely reactive titania precursor (Ti-isopropoxide). The amounts of the chemicals used in this recipe are given in Table 2.3. In preparation of this sol, first 3.15 ml of Ti-isopropoxide was mixed with 8 ml of n-propanol. This was followed by a subsequent addition of 0.5 ml acetyl acetone and rest of the n-propanol (8 ml). At the end 0.4 ml DI water and 0.1 ml nitric acid (16 M) were introduced in the mixture by drop wise addition. The final pH of the solution was around 2. HAp powders of two different average size were added to this titania sol in a similar way explained for Hybrid-I.

Table 2.3 The relative amounts of the chemicals to prepare Hybrid-II sol.

Material	Mole
Ti-isopropoxide	1
n-propanol	20
acetyl Acetone	0.5
water	2
nitric acid	2
ethanol	10
HAp	0.5

2.3.3. Preparation of Ti6Al4V substrates

Ti6Al4V rods (diameter = 20 mm) were obtained from S-Tech Corporation (Florida, USA) and they were cut to slices (with a thickness of approximately 2 mm) using a wire erosion machine. The coin shape substrates were polished by silicon carbide grinding papers no 360, 600, 800 and 1200 grit subsequently to achieve approximately equal roughness for all substrates. The polished Ti6Al4V samples were then cleaned before the coating process. The first step of the cleaning procedure was ultrasonic cleaning in DI water for 30 min to remove possible residues from the mechanical polishing. Afterwards, substrates were put in acetone (99.9%, Kimetsan, Ankara, Turkey) for 20 min, ethanol (96%, Merck) and DI water for 15 min to eliminate organic contaminants. The cleaned substrates were then dried by blowing warm air (around 70 ºC) using a hair drying machine.

2.3.4. Coating procedure

Dip coating process was employed to apply HAp-titania sols to the metallic substrates. Cleaned substrates were dipped in to the solution in a controlled manner by using a dip coater and hold submerged in the sol for 10 s and then withdrawn with a constant speed of 16 cm/min. Coating samples were first dried by blowing warm air (around 70 ºC) using a hair drying machine. This was followed by oven drying at 100 ºC for 1.5 h to remove the organics. Finally, the coated samples were heat treated at 500 ºC for 30 min for calcination and to mature the titania-based coating. “As-prepared” condition denotes the coated samples which were only exposed to warm air drying treatment and oven drying 100 ºC for 1.5 h.

Above explained coating procedure can be considered as a standard protocol for making a single layer of HAp-titania hybrid coating. However, a series of different coating process parameters have also been modified throughout the thesis to achieve some variations in the coating properties and also to control the physical and phase identity of the coatings. The main coating parameters that had been further explored in the thesis were; number of coating layers, dipping rate and post coating calcination temperature.

Accordingly, multi layered coatings were made by repeating the standard coating conditions. In making the multi layered samples after each individual coating step, same drying (warm air followed by oven drying) and calcination treatments (at 500 ºC, 30 min) were achieved.

In some coating trials, dipping rates of 9 and 22 cm/min were also employed to explore the effects of dipping rate on coverage efficiency, coating the morphology and thickness. In addition, some samples made according to standard coating and drying conditions outlined as above were calcined at 400 ºC and 600 ºC for 30 min. These studies were performed to investigate to identify the phases developing at different heat treatment temperatures and also morphological variations in the coating as a function of calcination temperatures.

CHAPTER 3

RESULTS AND DISCUSSION

3.1. Characterization of HAp powders

This section includes the material characterization results for the HAp powders synthesized according to the chemical routes outlined in the experimental section. The phase identification of the reaction products both in "as-precipitated" condition and "after calcination" treatments is presented. The morphological properties of the resultant HAp powders are also investigated. This section also discusses the chemistry and mechanism of the individual HAp synthesis routes in regard to the physical properties of the HAp powders formed. Table 3.1 displays the solubility of solid precursors used in these routes for synthesis of HAp. This information was interpreted to distinguish the properties of the synthesized HAp powders**.**

3.1.1. Phase analyses of hydroxyapatite powders

3.1.1.1. Phase analysis of HAp-I

HAp powders were obtained according to the reaction (3.1).

$$10Ca(OH)_{2(aq)} + 6H_3PO_{4(aq)} \rightarrow Ca_{10}(PO_4)_6(OH)_{2(s)} + 18H_2O_{(aq)} \quad (3.1)$$

The product was not a phase pure HAp as revealed by the XRD analysis. Figure 3.1 shows the phase identity of the solid products obtained according to the reaction (3.1) up to 21 days. This Figure discloses the XRD patterns of the solid samples extracted from the mother solution at 3^{rd}, 8^{th}, 12^{th} and 21^{st} days. As can be seen from the XRD patterns, HAp formation in poor crystalline nature starts in a couple of days (3 days). Along with HAp, another calcium phosphate phase - dicalcium phosphate dihydrate ($CaHPO_4 \cdot 2H_2O$ or DCPD) - continuously precipitates. At the end of the aging period of 21 days, extent of HAp formation was increased, but the precipitated phase was still not phase pure. After 21 days, there was still significant amount of dicalcium phosphate dihydrate.

Table 3.1 The solubility values (g/100 cc H_2O) for the chemical precursors used as calcium and phosphorus sources in different HAp precipitation routes [48].

	Solubility (g/100 cc)	
Name	**Cold water**	**Hot water**
$CaCO_3$	0.0014	0.0018
$Ca(NO_3)_2.4H_2O$	266	660
CaO	0.131	0.07
$Ca(OH)_2$	0.1850	0.0771
H_3PO_4	548	very soluble
$(NH_4)_2.HPO_4$	57.5	106.0

The reasons for limited formation of HAp crystals with an undesired second phase were explored with solution chemistry studies, where the pH of the mother was continuously monitored during precipitation. The pH values of the solution ranged

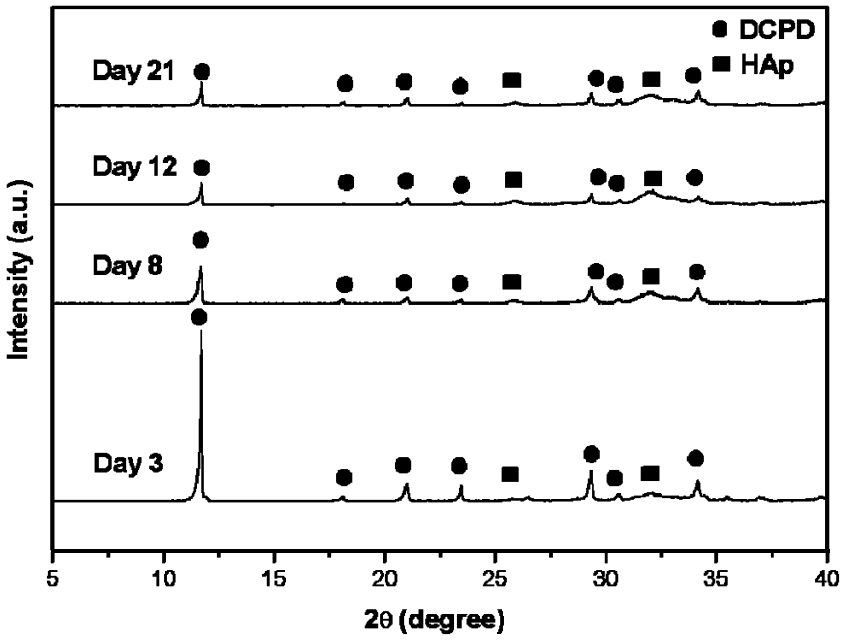

Figure 3.1 XRD diffractograms of the solid precipitates formed at different times of aging during synthesis of HAp-I.

from 11.5 to 13 during the 21 days of aging. The almost constant pH behavior suggests that no or very limited OH^- ion uptake from the solution which may lead to precipitation to HAp precipitation. If OH^- ions in the solution were used in the expense of HAp crystal formation, the solution pH should decrease continuously reaching to the saturation at the end. The co-precipitation problem seems to be related to the stoichiometrical deviations in the mother solutions and can be modified in a way to obtain phase pure product.

Figure 3.2 shows a flow chart of the modified first route to produce HAp powders. The effect of excess orthophosphoric acid (H_3PO_4) on pH and kinetics of Hap formation was studied. Different amounts of 0.1 M orthophosphoric acid (1, 10, 15 and 20 ml) were added to 20 ml of 21-days aged solution separately.

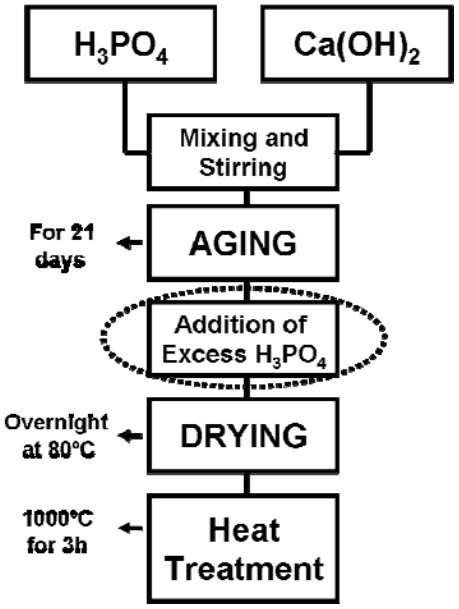

Figure 3.2 Modified flow-chart of the first route by addition of phosphoric acid to accelerate the dissolution of brushite.

The changes for the solid products upon addition of the orthophosphoric acid are represented by XRD analysis as shown in Figure 3.3. Addition of 1 ml and 10 ml of orthophosphoric acid to the solution provided the formation of almost phase pure HAp and only limited amount of dicalcium phosphate dihydrate was left for these two solutions. At these particular concentrations of extra orthophosphoric acid, the formation of HAp was promoted which was also confirmed by the changes in the pH of the mother solution. Figure 3.4 shows the change in pH as a function of orthophosphoric acid addition. The pH values decreased by the addition of the acid as expected. But there is a limiting value for the excess phosphoric acid as can be seen in XRD diffractograms in Figure 3.3. In case of higher amount of orthophosphoric acid addition, i.e. for 15 ml and 20 ml, formation of DCPD phase was actually promoted. This difference is governed by the solubility diagram defining the stability of the all calcium orthophosphate salts that are at equilibrium with their saturated aqueous solutions.

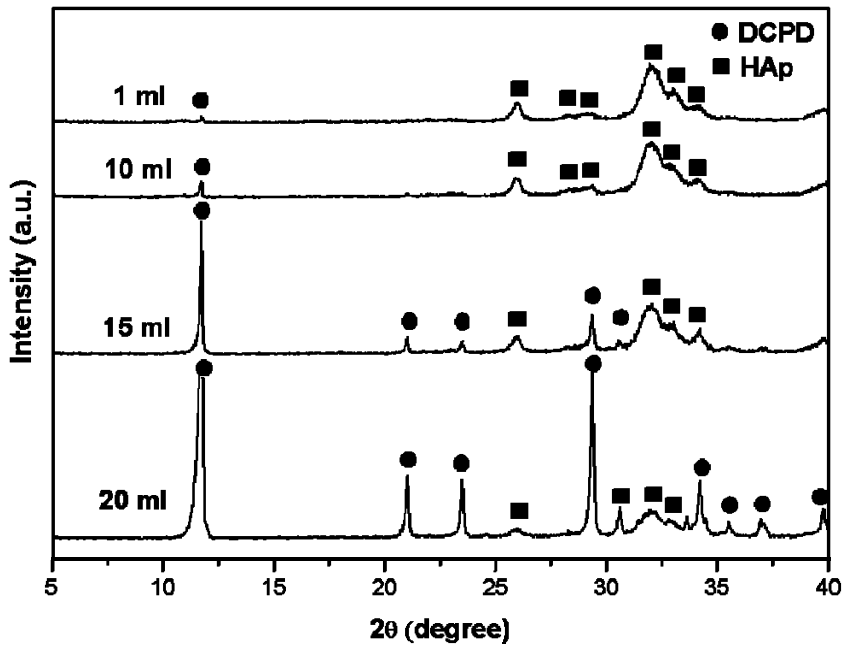

Figure 3.3 XRD diffractograms of the solid precipitates formed according to the modified recipe for HAp-I upon addition of excess H_3PO_4.

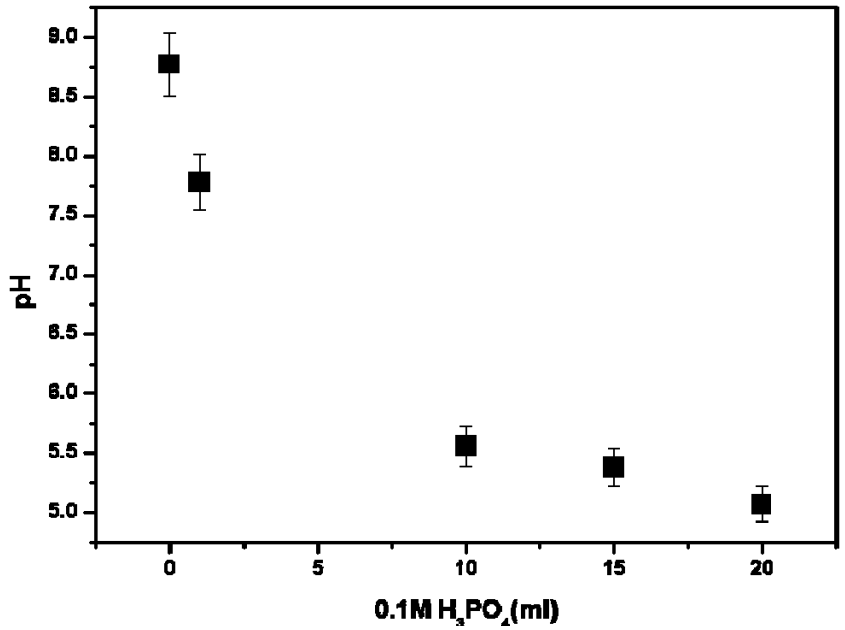

Figure 3.4 The pH change of the mother solution as a function of excess ortho-phosphoric acid addition.

The stability isotherm is shown in Figure 3.5. Accordingly, from all the possible calcium phosphates, HAp is the only thermodynamically stable phase at 10.5>pH>4.3 whereas $CaHPO_4$ (dicalcium phosphate, DCP) or $CaHPO_4 \cdot 2H_2O$ (dicalcium phosphate dehydrate, DCDP) might be both stable at lower and higher pH values. This explains the precipitation of DCPD when excess amount of orthophosphoric acid is (more than 1 ml/ 20 ml) added in the modified formulations where the final solution pH values reach close to 4.3.

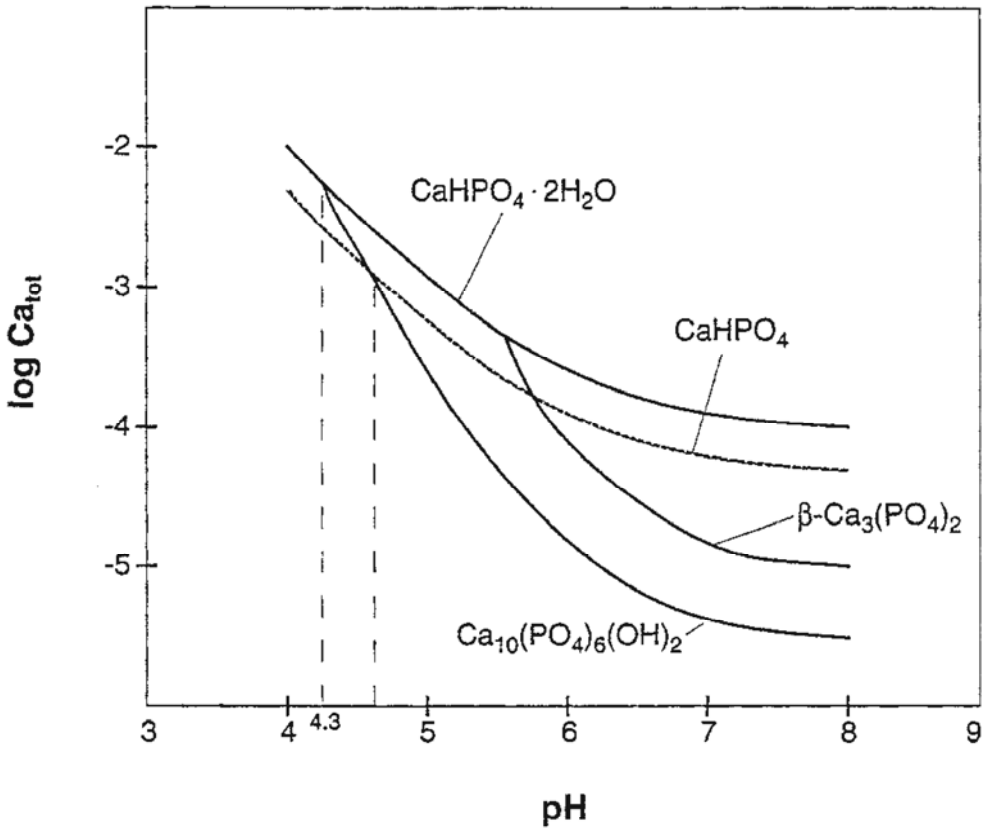

Figure 3.5 Solubilities of various calcium phosphate phases at 25 ºC in the system of $CaO\text{-}P_2O_5\text{-}H_2O$ as a function of pH [49].

In summary, HAp-I which was synthesized from relatively moderately soluble precursors; $Ca(OH)_2$ and H_3PO_4 co-precipitated with DCPD. Formation of this second phase can be avoided to some extent in the presence of excess phosphorus solution to promote the formation of HAp. But even after this modification at the end of aging period, although HAp product was obtained, there was still some DCPD as a second calcium-phosphate phase.

3.1.1.2. Phase analysis of HAp-II

In making HAp-II, calcium source with relatively lower solubility - $CaCO_3$ - and $[(NH_4)_2HPO_4]$ were employed to obtain HAp precipitates according to the reaction shown below.

$$10CaCO_{3(s)} + 6(NH_4)_2HPO_{4(s)} \rightarrow Ca_{10}(PO_4)_6(OH)_{2(s)} + H_2O_{(aq)} + CO_{2(g)} \quad (3.2)$$

Figure 3.6 displays the evolution of the HAp product as a function of precipitation time. The XRD analysis were performed on samples collected at the 2nd, 4th and 6th days which show that the formation of CaO also proceeds during evolution of HAp product. But there was no CaO or any other phase different than poorly crystallized HAp after 6 days. This product was phase pure HAp in as-precipitated condition. As precipitated HAp-II was phase pure, but its stoichiometry was off as determined by further XRD analysis of the heat treated samples. A calcium-to-phosphorous ratio of Ca/P=1.67 stands for stoichiometric HAp with the composition of $Ca_{10}(PO_4)_6(OH)_2$. As shown by the XRD patterns in Figure 3.7 after the calcination at 1000 ºC for 3 h, the crystallinity of HAp powders improves distinctly. In addition to this change, CaO starts to form. Formation of CaO after calcination suggest that the Ca/P ratio is higher than stoichiometric ratio of Ca/P=1.67.

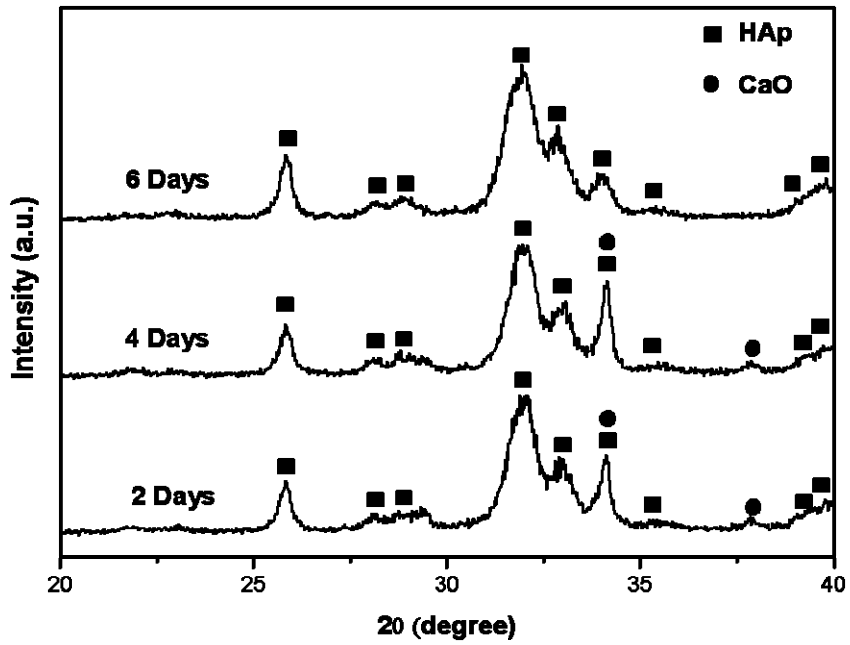

Figure 3.6 XRD diffractograms of the solid precipitates formed at different times of aging during the synthesis of HAp-II.

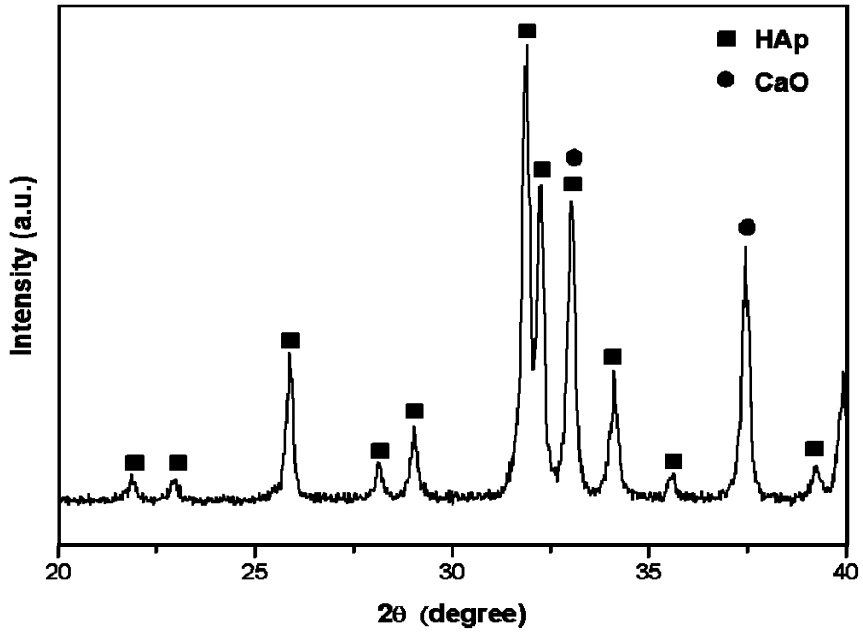

Figure 3.7 XRD diffractograms of HAp-II calcined at 1000 ºC for 3h.

It can be seen from the phase diagram of $CaO\text{-}P_2O_5$ in Figure 3.8 showing the phase regions of calcium-phosphate salts. For calcium phosphate compounds with calcium deficiency, i.e. Ca/P<1.67 (C_3P:$Ca_3(PO_4)_2$) is expected to form at calcination temperatures higher than 800^oC. In a similar way, existence of CaO together with HAp suggests that this product is not stoichiometric and that Ca/P ratio of HAp-II is higher than 1.67.

3.1.1.3. Phase analysis of HAp-III

Both of the synthesis routes used for HAp-I and HAp-II were not completely successful in producing a phase pure product of high crystallinity. A third route was used for making HAp-III with the use of precursors $Ca(NO_3)_2.4H_2O$ and $(NH_4)_2HPO_4$ which offers a calcium source with the highest solubility compared to those used in the previous precursor couples. The chemical reaction for this route is shown below.

$$10Ca(NO_3)_2.4H_2O_{(s)} + 6(NH_4)_2HPO_{4(s)} + 8NH_4OH_{(aq)} \rightarrow$$

$$Ca_{10}(PO_4)_6(OH)_{2(s)} + 20NH_4NO_{3(g)} + 40H_2O_{(aq)} \qquad (3.3)$$

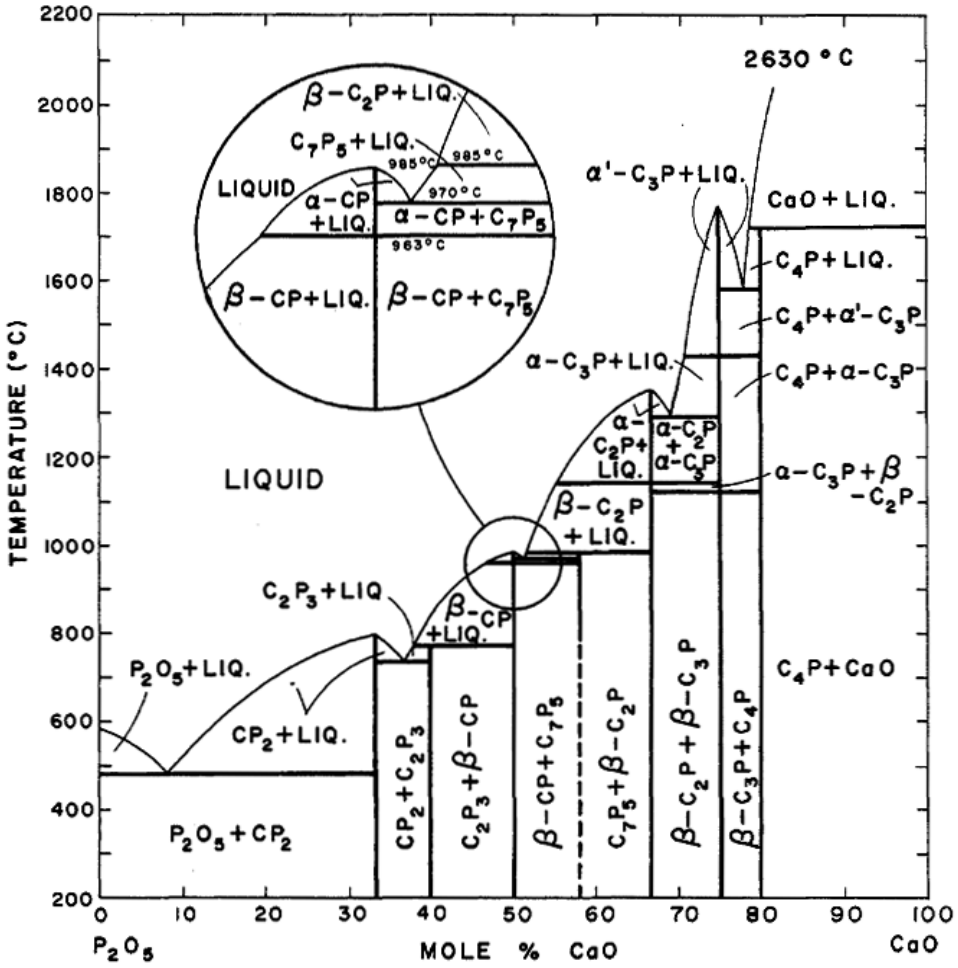

Figure 3.8 Phase diagram of the CaO-P_2O_5 system; (C=CaO, P=P_2O_5) [50]

Figure 3.9 shows the XRD patterns of the HAp product in as-precipitated form produced by this reaction. This Figure reveals that there was no other diffraction peak observable besides HAp peaks after 24 h of precipitation reaction. The precipitated powders were subsequently calcined at 1000 ºC for 3 h and Figure 3.10 shows the XRD pattern of the calcined HAp-III powder. Sharper and well defined diffraction peaks with an increase in the intensities indicate improved crystallinity for the calcined powders. No additional phase was formed after calcination and this confirms the purity and stoichiometry of HAp product at as-precipitated condition. HAp-III was the most successful in all three routes used. Phase pure HAp can be formed in one day.

3.1.2. Scanning Electron Microscopy (SEM) analyses of hydroxyapatite powders

SEM analyses reveal the details about the particle size and morphology of the HAp powders. SEM results have been also interpreted in explaining the precipitation mechanisms of different HAp powders according to three precipitation reaction.

Figure 3.11 discloses the SEM micrographs displaying the morphology of the all HAp powders synthesized in this work. These SEM images are representative for the calcined powders. HAp-I crystals have an average size of 0.5-1 μm and these crystals form irregularly shaped agglomerates ranging 2-20 μm. Similarly, SEM micrograph of HAp-II shows the average crystal size of these powders that are smaller compared to those for HAp-I and nano-sized reticulated crystals of HAp gather as irregular shaped agglomerates of 5-30 μm. HAp-III, on the other hand, exhibit a plate like morphology. The average size of these particles ranged between 10-20 μm. No agglomerates are present unlike HAp-I and HAp-II.

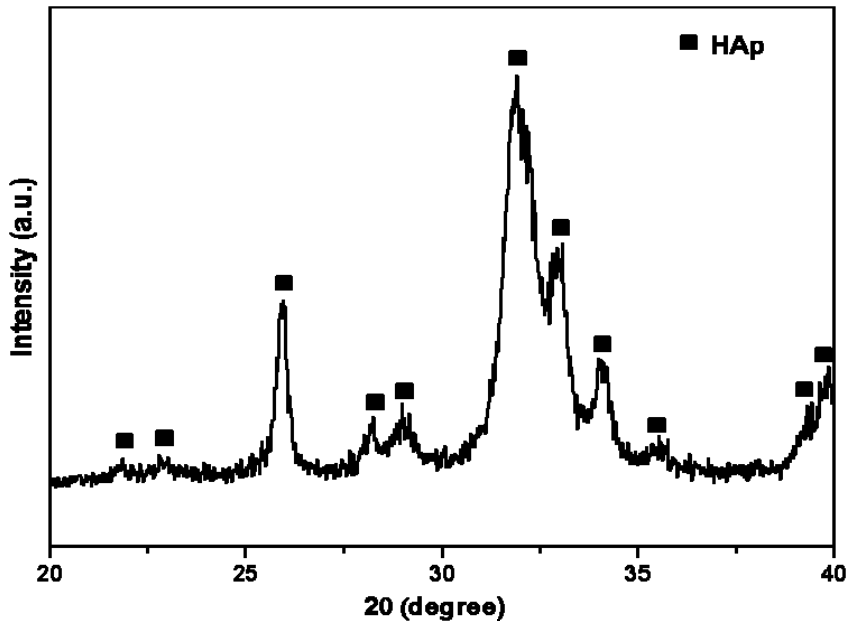

Figure 3.9 XRD diffractogram of HAp-III in as-precipitated form.

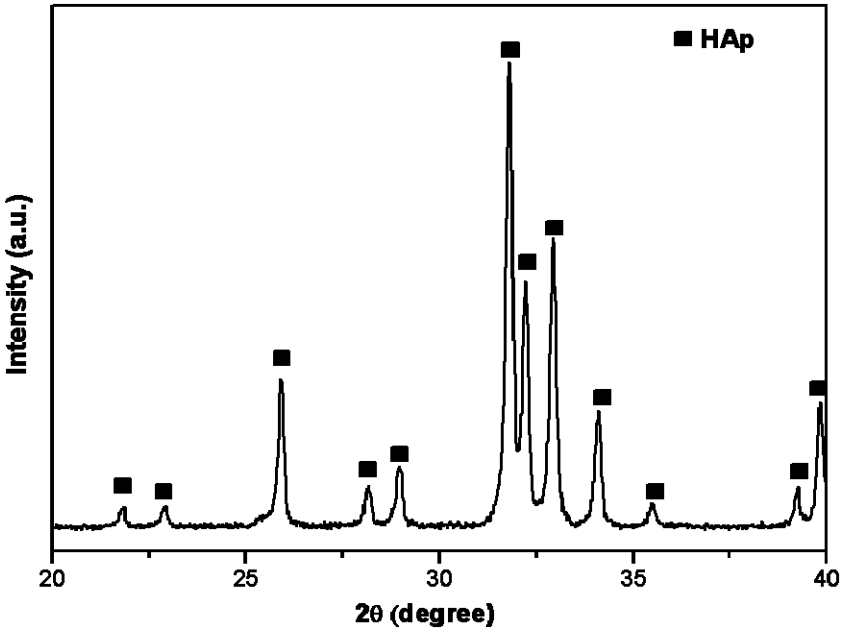

Figure 3.10 XRD diffractogram of HAp-III calcined at 1000 ºC for 3 h.

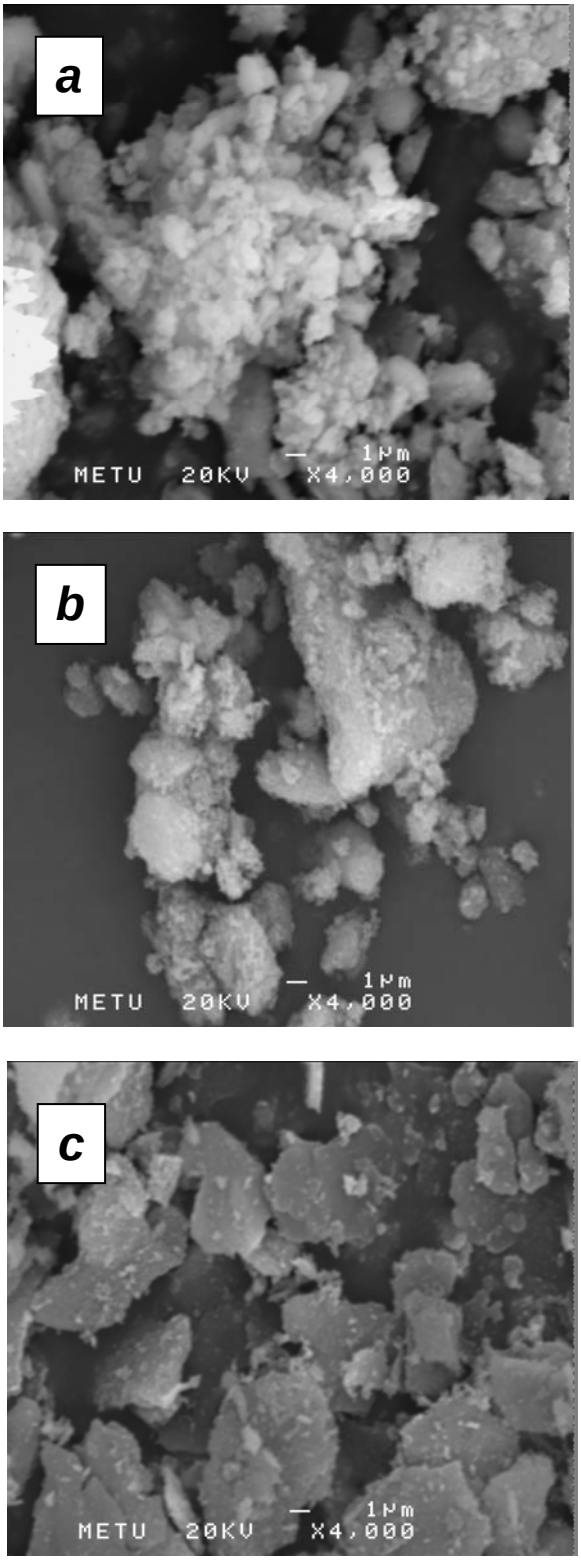

Figure 3.11 SEM micrographs of (a) HAp-I, (b) HAp-II and (c) HAp-III powders (scale bar=1 micrometer).

Together with the control on chemical identity of the HAp product, another reason for using different precursor couples in study was to tailor the size and the morphology of the HAp powders. Control on product particle size could be achieved by manipulating the solubilities of the precursors. The solubilities of the precursors compounds eventually affect the saturation level of the ionic constituents in the solution. This is one of the critical factors that can affect particle size of the final product. Saturation index (or saturation ratio, S) is a term to define the degree of saturation and it is described as;

$$\textit{Saturation Index} = \textit{Actual Concentration} / \textit{Solubility} \qquad (3.4)$$

Crystal size and morphology are both related to the saturation index. Degree of supersaturation also determines the nucleation rate. For ionic solutions with relatively higher saturation indices one should expect formation of nuclei products in larger numbers and therefore precipitation of relatively small crystals products.

This is possible when salts of low solubility are used. As it has been shown by this study so far, HAp powders with smaller crystals were produced as in HAp-I and HAp II, where moderately or sparingly soluble salt precursors are used. In making HAp-III on the other hand, $Ca(NO_3)_2 \cdot 4H_2O$ and $(NH_4)_2HPO_4$ were used. Both are highly soluble in water and high solubility of the precursors led to solution with smaller saturation index compared to the other solutions prepared in the two previous precipitation methods. Therefore, for HAp-III low nucleation rates favored formation of larger and discrete crystals precipitates. Figure 3.12 schematically shows the two HAp products that can be formed at different solution saturation levels analogous to the difference observed for HAp-II and HAp-III.

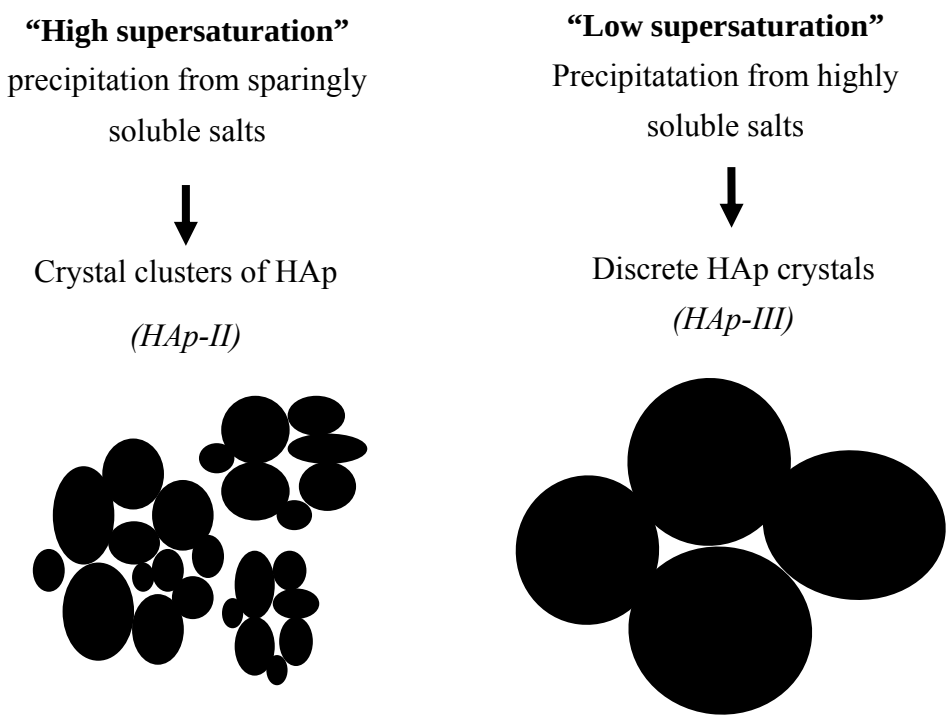

Figure 3.12 Schematic representation for HAp powders that can be formed at two different solution saturation levels.

3.1.3. Fourier Transformed Infrared (FTIR) analyses of hydroxyapatite powders

FTIR spectra analyses were performed to further distinguish the chemical structure of HAp products by investigating the details in absorption behavior due to presence of different structural groups of OH^-, PO_4^-, HPO_4 and CO_3^- bands. Table 3.2 is a modified list from Bonfield and Rehman's study and it displays IR absorption band assignments of different structural groups for pure products of carbonated and commercial grade HAp [51]. This table also shows absorption observed peak assignments of the HAp powders synthesized in this thesis, both in as-precipitated and calcined state.

Table 3.2 FTIR absorption band assignments for commercial HAp, carbonated HAp and HAp products synthesized in the thesis in as-precipitated (top) and calcined (bottom) state.

Peak Assignments	Carbonated	Commercial	$Ca(OH)_2$ +	$CaCO_3$ +	$Ca(NO_3)_2.4H_2O$ +
HA cm^{-1}	Apatite	HAp	H_3PO_4	$(NH4)_2HPO_4$	$(NH4)_2HPO_4$
Hydroxyl Stretch	3571	3570	3569	3570	3570
Carbonate υ_3	1650-1300	1650-1300	1650-1300	1650-1300	1650-1300
-(m)	1650	1648	1641	1641	1641
-(m)	1454	1455	1463	1465	1463
-(m)	1417	1417	1421	1411, 1427	1423
-(w)	1321	-	1309	1309	1311
Phosphate υ_3	1190-976	1190-976	1190-976	1190-976	1190-976
-(vs)	-	1091	-	1088	1092-1094
-(vs)	1041	1042	1034-1036	1034	1030-1032
Phosphate υ_1 (m)	961	962	962	961	962
Carbonate υ_2 (ms)	873	877	874	874	876
Phosphate υ_4	668-520	668-520	668-520	668-520	668-520
-(m)	629	632	-	629	629
-(vs)	603	602	601	606	602
-(vs)	567	566	565	569-563	563
Phosphate υ_2 (w)	469	472	473	473	473

Peak Assignments	Carbonated	Commercial	$Ca(OH)_2$ +	$CaCO_3$ +	$Ca(NO_3)_2.4H_2O$ +
HA cm^{-1}	Apatite	HAp	H_3PO_4	$(NH4)_2HPO_4$	$(NH4)_2HPO_4$
Hydroxyl Stretch	3571	3570	3572	3574	3572
Carbonate υ_3	1650-1300	1650-1300	1650-1300	1650-1300	1650-1300
-(m)	1650	1648	1641	1642	1641
-(m)	1454	1455	1481, 1466, 1450	1458, 1450, 1442, 1429	1468, 1450, 1442,
-(m)	1417	1417	1414	-	1425, 1413-1411
-(w)	1321	-	-	-	-
Phosphate υ_3	1190-976	1190-976	1190-976	1190-976	1190-976
-(vs)	-	1091	1090	1092	1092
-(vs)	1041	1042	1057-1026	1042-1040	1043-1042
Phosphate υ_1 (m)	961	962	961	961	962
Carbonate υ_2 (ms)	873	877	-	876	-
Phosphate υ_4	660-520	660-520	660-520	660-520	660-520
-(m)	629	632	632	637	636
-(vs)	603	602	602	604	602
-(vs)	567	566	569	569	571
Phosphate υ_2 (w)	469	472	475	465	474

Figure 3.13 shows the complete IR spectra (in the range of 400-4000 cm^{-1}) of powders HAp-I, HAp-II and HAp-III in as-precipitated and calcined state. The detailed analyses of the complete IR spectra of produced HAp powders have been performed in the respective regions for vibration frequencies for, carbonate, phosphate and hydroxyl groups.

3.1.3.1. Carbonate groups

Figure 3.14 shows the selected region (1800-700 cm^{-1}) of IR spectra of HAp powders in as-precipitated and calcined state where carbonate absorption bands should be present. There are four types of vibrational modes for carbonate groups (υ_1, υ_2, υ_3 and υ_4) but only two (υ_2 and υ_3) of them are observable in IR spectra as listed in Table 3.2 Both of these bands are present for all HAp powders in as-precipitated condition; one around 1650-1300 cm^{-1} assigned for υ_3 and second around 873 cm^{-1} for υ_2 vibrational mode. There is no significant difference for all as-precipitated HAp powders as shown in Figure 3.14a.

Calcination produced some changes in the chemical structure for HAp-I and HAp-III. Figure 3.14b is a collection of IR spectra of the calcined HAp powders. The carbonate related absorptions, i.e. at around 1650-1300 cm^{-1} assigned for υ_3 and around 873 cm^{-1} for υ_2 vibrational mode, is only observable for HAp-II but not for HAp-I and HAp-III. This means that carbonate group is an intrinsic structural group only in HAp-II, where the calcium source was $CaCO_3$. The carbonate substitution observed in as-precipitated HAp-I and HAp-II with a representative formula of $Ca_{(10-x)}(CO_3)_x(PO_4)_{(6-x)}(OH)_{(2-x)}$ is due the physical absorption of CO_2 from the air atmosphere during precipitation, which was driven off during calcination.

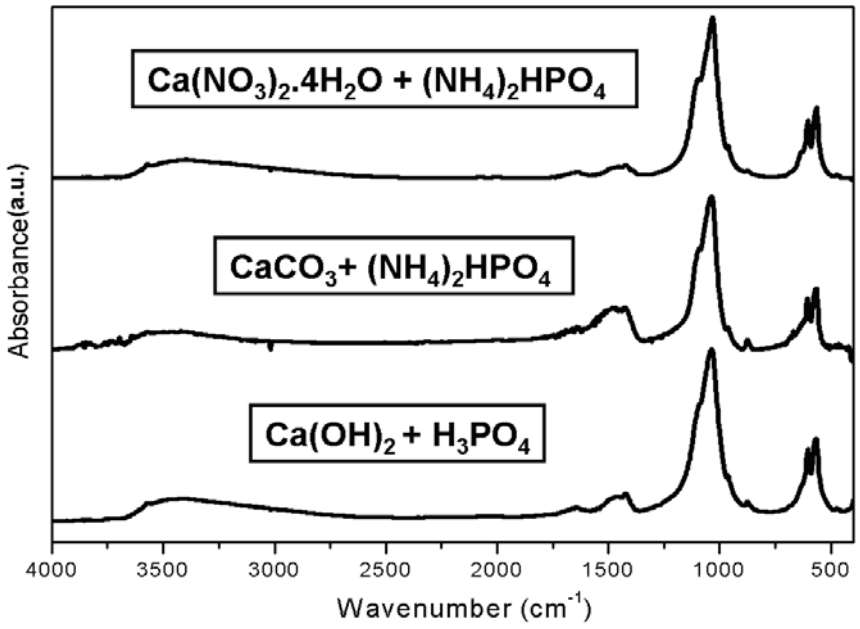

(a)

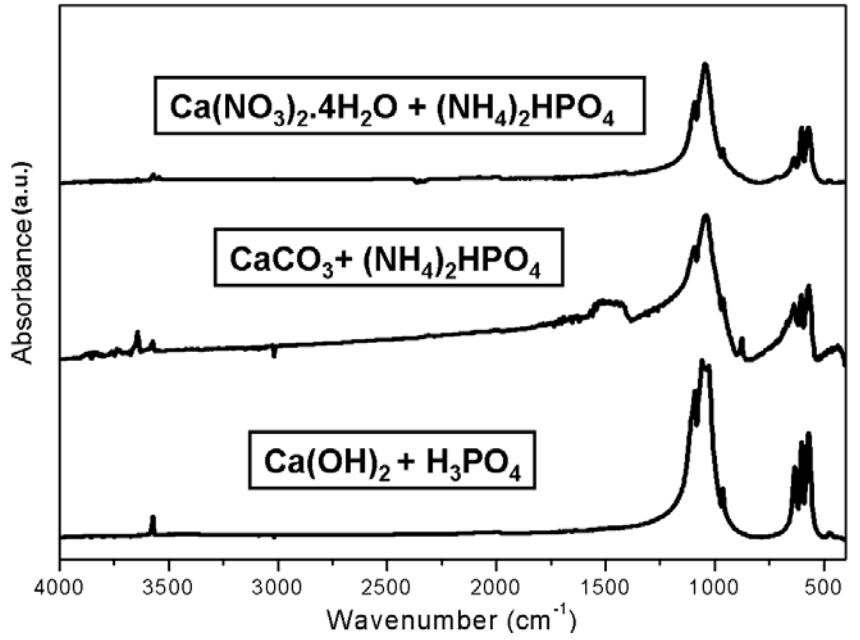

(b)

Figure 3.13 Complete FTIR spectra (400-4000 cm^{-1}) of the HAp-I, HAp-II and HAp-III in (a) as-precipitated, and (b) calcined state.

.

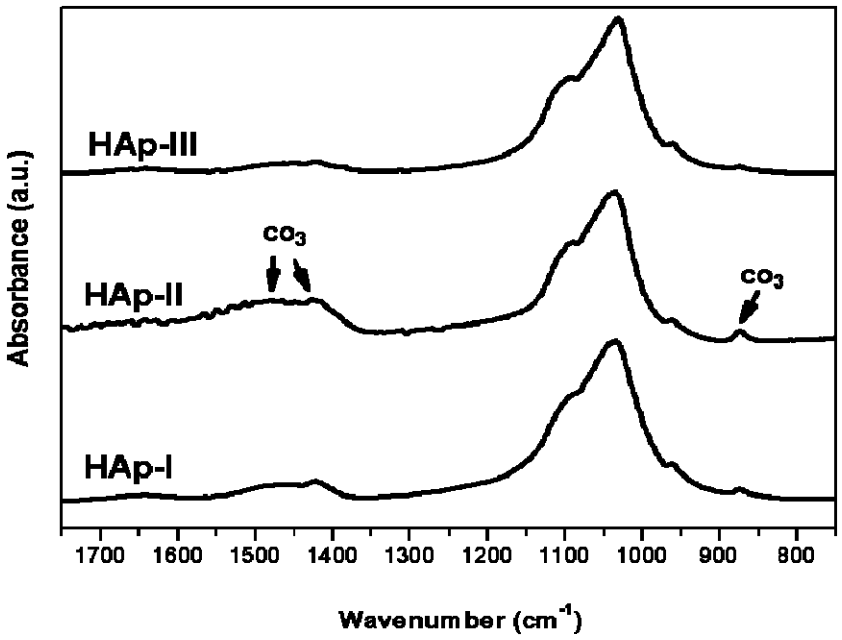

(a)

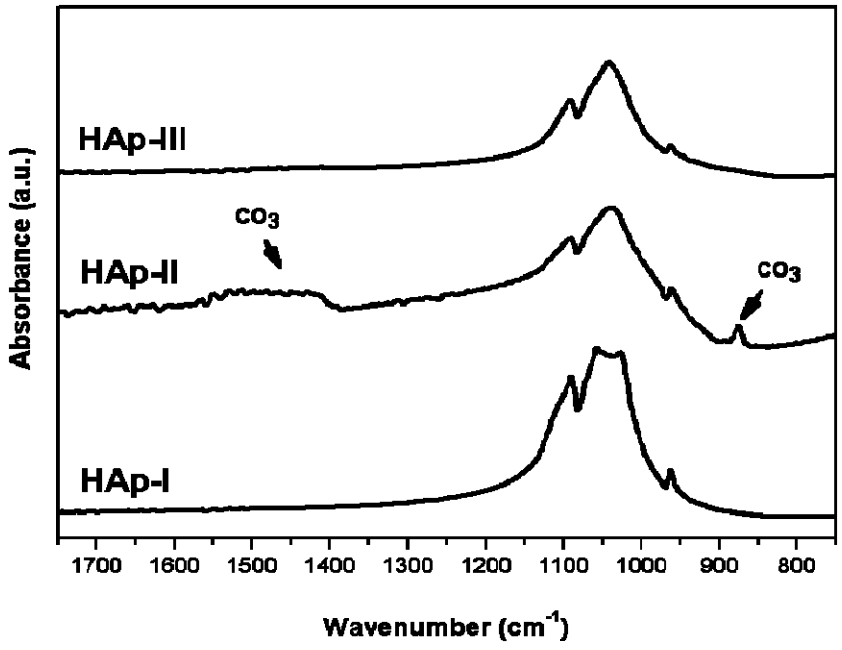

(b)

Figure 3.14 CO_3^- absorption bands for the HAp-I, HAp-II and HAp-III in (a) as-precipitated, and (b) calcined state.

3.1.3.2. Phosphate groups

Figure 3.15 shows the phosphate absorption bands of the HAp powders in as-precipitated and calcined form in the range of 1300-400 cm^{-1}. There is no remarkable difference for as-precipitated powders prepared with different precursor couples. For all HAp main P-O bands are present observed at around 1090cm^{-1} 1040 cm^{-1} for antisymmetric stretch mode; at around 962 cm^{-1} for symmetric stretch modes; and at around 602 and 569-566 cm^{-1} for antisymmetric bending mode respectively.

There is another band common in all spectra located at around 870 cm^{-1}. This band can be due to either HPO_4 group (P-OH stretch of HPO_4) or due to υ_2 band of CO_3^- (873 cm^{-1}) as mentioned in section 3.3.1. However, none of the additional bands for P-OH , 1023, 906 and 852 cm^{-1} [52] are present for any of the HAp powders suggesting that 870 band is from CO_3. So, it can be said that as-precipitated HAp powders do not include any HPO_4 group as is in Ca-deficient HAp ($Ca_{(10-x-y)}(HPO_4)_x(CO_3)_y(PO_4)_{(6-x-y)}(OH)_{(2-x-y)}$), but simply a carbonated version.

This is also supported by the FTIR data of the calcined sample as shown in Figure 3.15b. There is no significant variation in phosphate group bands with calcination. But the disputable 870 cm^{-1} peak is only present for Hap-II, the carbonated HAp. As discussed in the previous part this peak disappears for HAp-I and HAp-III upon removal of absorbed carbonate during calcination.

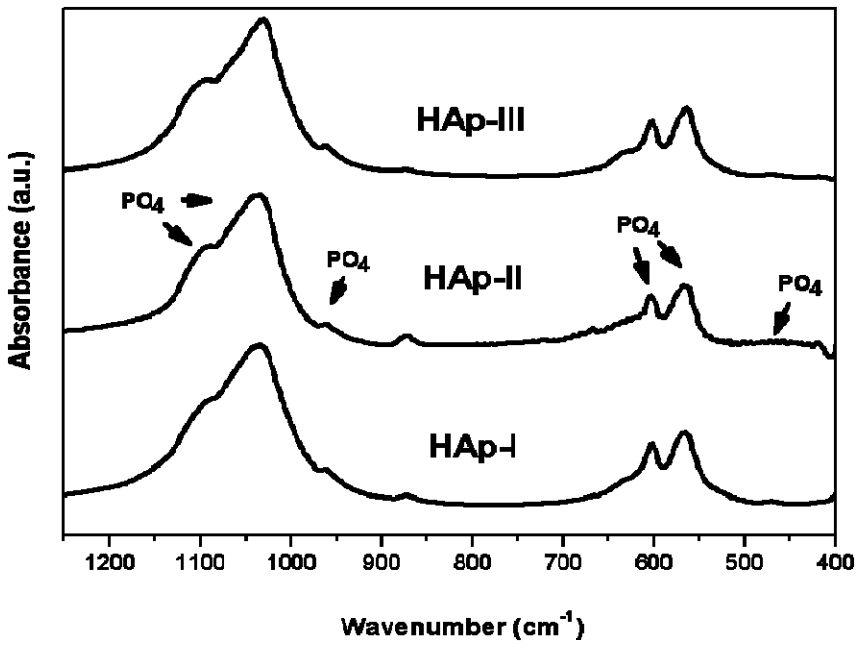

(a)

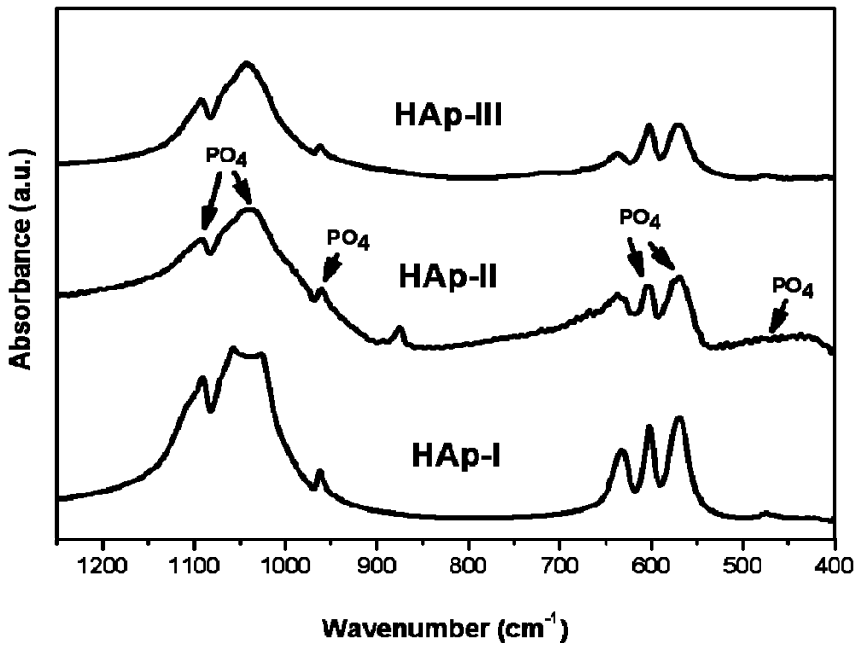

(b)

Figure 3.15 Phosphate absorption bands for the HAp-I, HAp-II and HAp-III (a) as-precipitated, and (b) calcined state.

3.1.3.3. Hydroxyl and water groups

Figure 3.16 shows the differences for all three HAp powders in terms of physically (absorbed H_2O) and chemically bound (due to OH) water. The absorption band for OH^- stretch is at 3569 cm^{-1} for the HAp-I and 3570 cm^{-1} for HAp-II and Hap-III. In as-precipitated samples, absorption intensity of OH^- stretch band is lower than those for calcined ones which may indicate the carbonate substitution in the structure of the samples [51]. The peaks for adsorbed water are at 340 cm^{-1} and 1650cm^{-1} and high absorption intensity of water molecules for as-precipitated product explicates the increment in the contamination due to water molecules [53].

As it can be seen from Figure 3.16a and 3.16b, adsorbed water simply decomposes subsequent to calcination. The determining band for structural form of OH observed at 3570 cm^{-1} for HAp-I and HAp-III, whereas 3574 and 3643 cm^{-1} for Hap-II. The intensity difference is related to the amount of removed H_2O from the structure during calcination at 1000 ºC. The significant difference between calcined samples and as-precipitated ones is the development of a new peak for calcined samples at 633cm^{-1} for HAp-I, and 637 cm^{-1} for HAp-II and HAp-III samples. Figure 3.17 reveals the comparison of as-precipitated and sintered HAp samples due to the latterly formed peak between the bands 700-400 cm^{-1}. This well-defined peak belongs to structural OH^- and was developed by increasing temperature. As it can be seen from the comparison of Figure 3.16a and 3.16b absorbed water simply decomposes after calcination.

As a result, according to XRD and FTIR analyses, HAp-III powder is the only phase pure and stoichiometric sample among all three HAp products. Therefore, HAp-III is mostly used in subsequent coating studies if otherwise is mentioned.

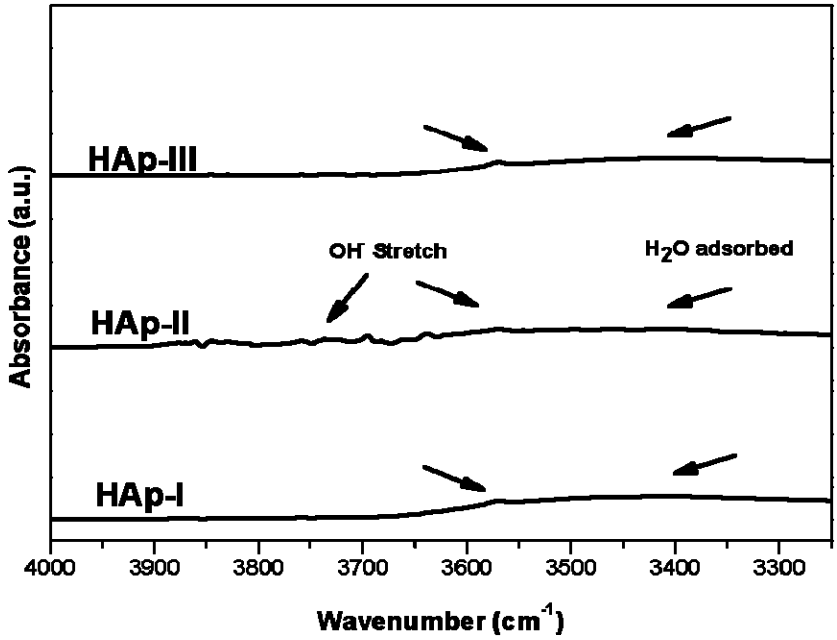

(a)

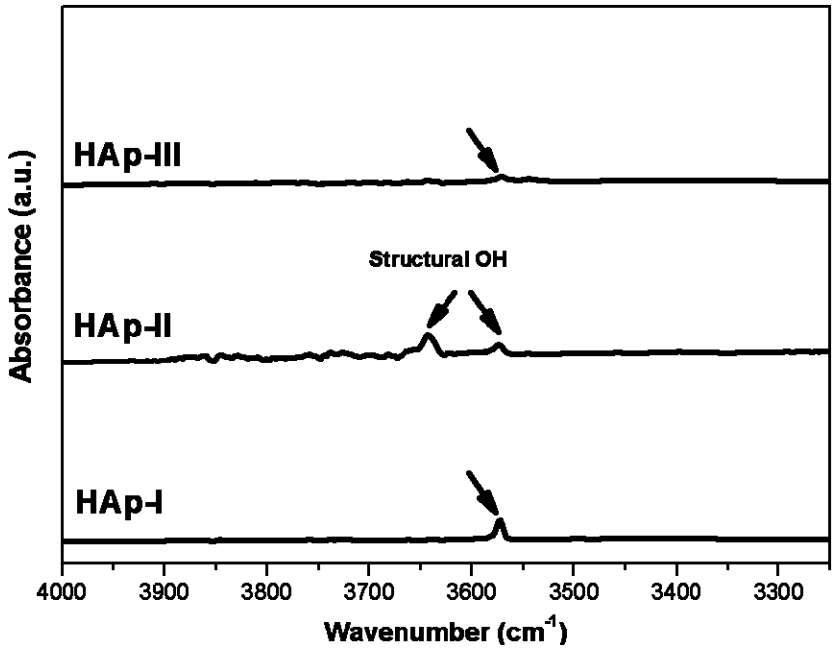

(b)

Figure 3.16 OH group absorption bands for the HAp-I, HAp-II and HAp-III a) as-precipitated, and (b) calcined state.

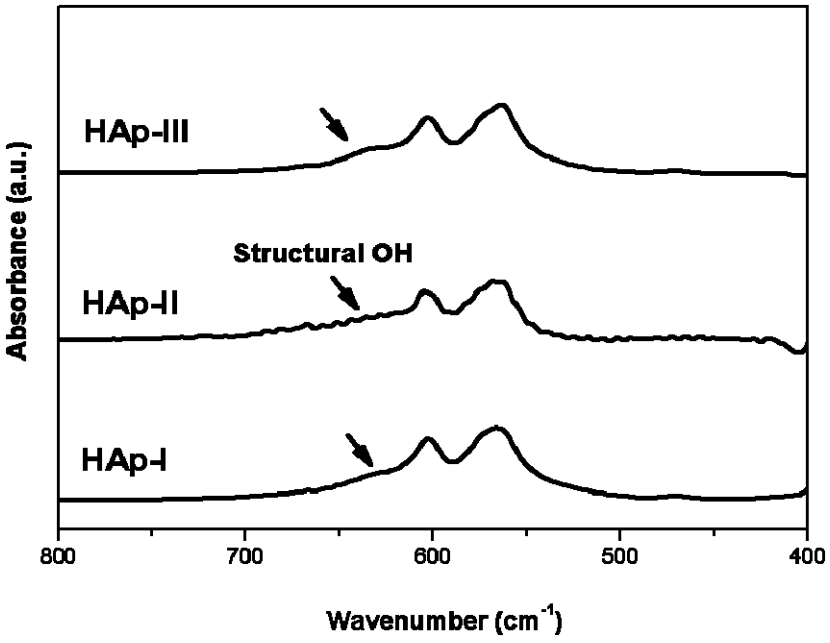

(a)

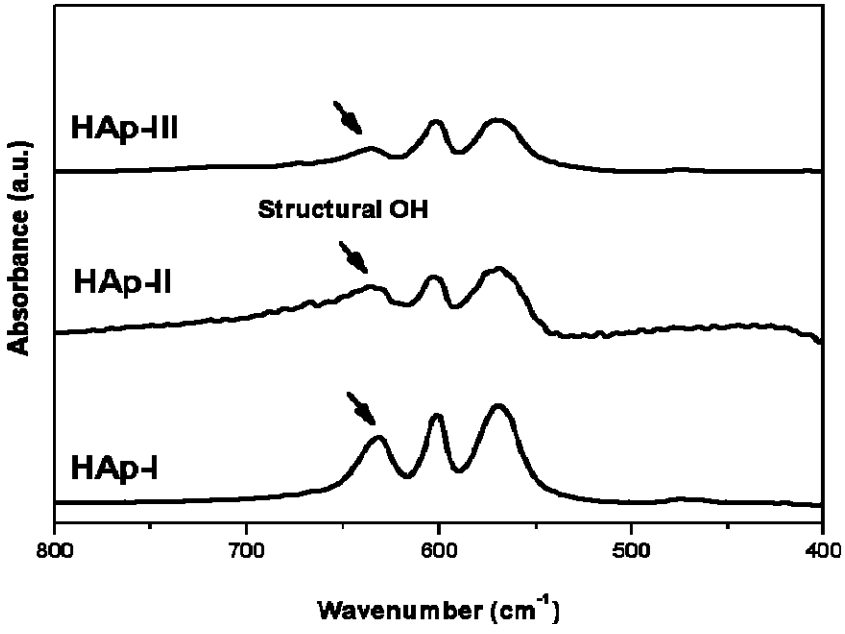

(b)

Figure 3.17 Structural OH group absorption bands for the HAp-I, HAp-II and HAp-III (a) as-precipitated, and (b) calcined state.

3.2. Characterization of HAp-titania coatings

The focus of this section is the characterization of HAp-titania coatings formed using two formerly introduced titania sol formulations, named as Hybrid-I and Hybrid-II. The coating solutions were obtained by introducing pre-synthesized HAp powders into a titania sol by mechanical mixing. Dip coating was employed for applying the coating solutions onto Ti6Al4V substrates. Morphological investigations and phase identifications of the prepared coatings have been performed. The properties of the coatings in as-prepared and sintered conditions are discussed.

This section also includes modifications that have been achieved in coating properties as a function of HAp powder properties, calcination temperature and due to variations in dip coating process parameters. XRD, SEM and EDS analyses were performed for the characterization of the coatings. The typical calcination procedure was open air heating at 500 ºC for 30 min if some different condition is mentioned. Typically a dip coating withdrawal rate was 16 cm/min. Generally, HAp-III with an average particle size of 10-20 μm-was used.

XRD diffractogram of a bare Ti6Al4V substrate is shown in Figure 3.18 as a reference for comparison purpose. Figure 3.19 illustrates the SEM micrographs representative for the surface of non-coated Ti6Al4V after surface pretreatment for the same purpose. The inset in Figure 3.18 is a redisplay of XRD diffractogram of Ti6Al4V, but with much lower intensity scale values to improve the resolution. The XRD diffractograms for the coatings presented are also in the same intensity scale with this inset to ease the interpretation of the XRD data and the determination of diffraction peaks in 2θ of interest.

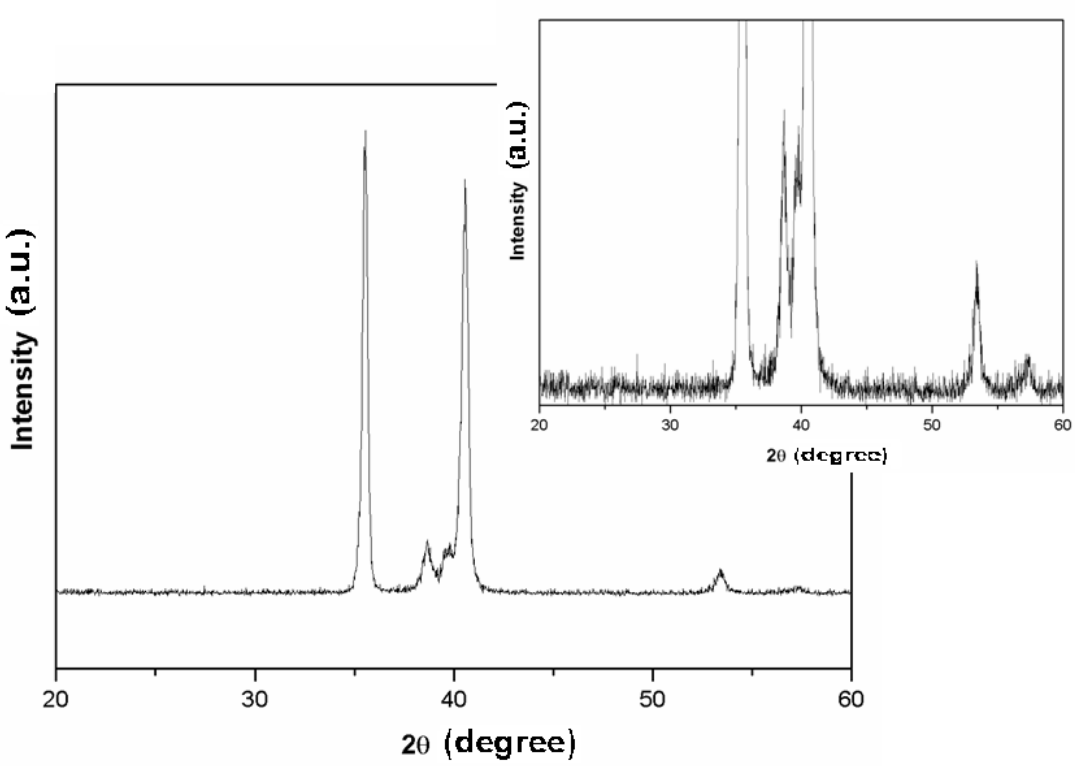

Figure 3.18 XRD diffractogram of bare Ti6Al4V substrate. The inset is the same diffractogram with better resolution redisplayed according to intensity.

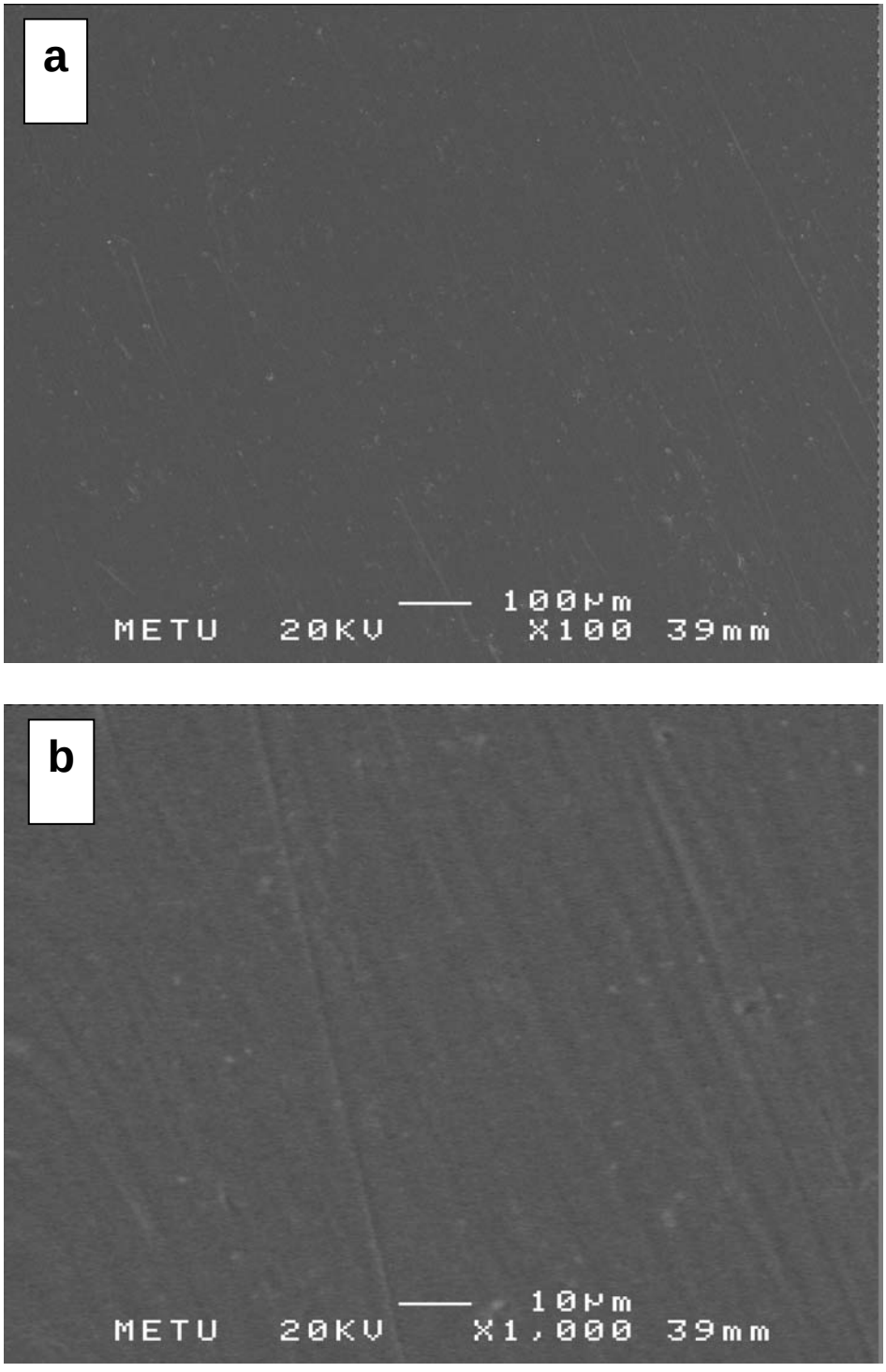

Figure 3.19 SEM micrographs of bare Ti6Al4V surface at (a) x100 and (b) x1000. Scale bars correspond to 100 µm and 10 µm respectively.

3.2.1. Effect of number of layers on coating properties

A coating prepared by mechanical mixing method was employed for understanding the effect of multiple application of coating solution on the general coating morphology and phases. Figure 3.20 shows the SEM results of a single layer coating sample and three-time coated Hybrid-I sample which were subsequently calcined at same conditions (at 500 ºC for 30 min). According to Figure 3.20a, HAp powders are present on substrate surface but the surrounding coating layer is not thick enough as the scratches on the metal substrate from the polishing process can be observed. On the other hand, Figure 3.20b. displays a complete surface coverage due to a presence of a thicker of titania matrix without any scratch tracks. This time HAp crystals are embedded in relatively thicker but not a pristine coating. Crack network formation is the most significant outcome of multilayer application of the coating and cracks in these thick coating will obviously lower the quality of the coating by deteriorating the bonding strength and overall durability of the coatings. This issue will be discussed further in the coming sections and crack formation can be minimized and sometimes completely avoided by proper choice of the organic components in the coating solution.

XRD results also exhibit parallel result with SEM observations suggesting more accumulation of the coating material in the case of multi layer application as shown in Figure 3.21. According to these XRD patterns, accompanied with the increase in the intensity HAp peaks (set of peaks at around 2θ = 32-33º) the intensities of diffractions from anatase also get strengthened in case of multilayered coatings. The amount of HAp powders adhered on the substrates surface and the thickness of the titania matrix both enhance with the number of coating layer.

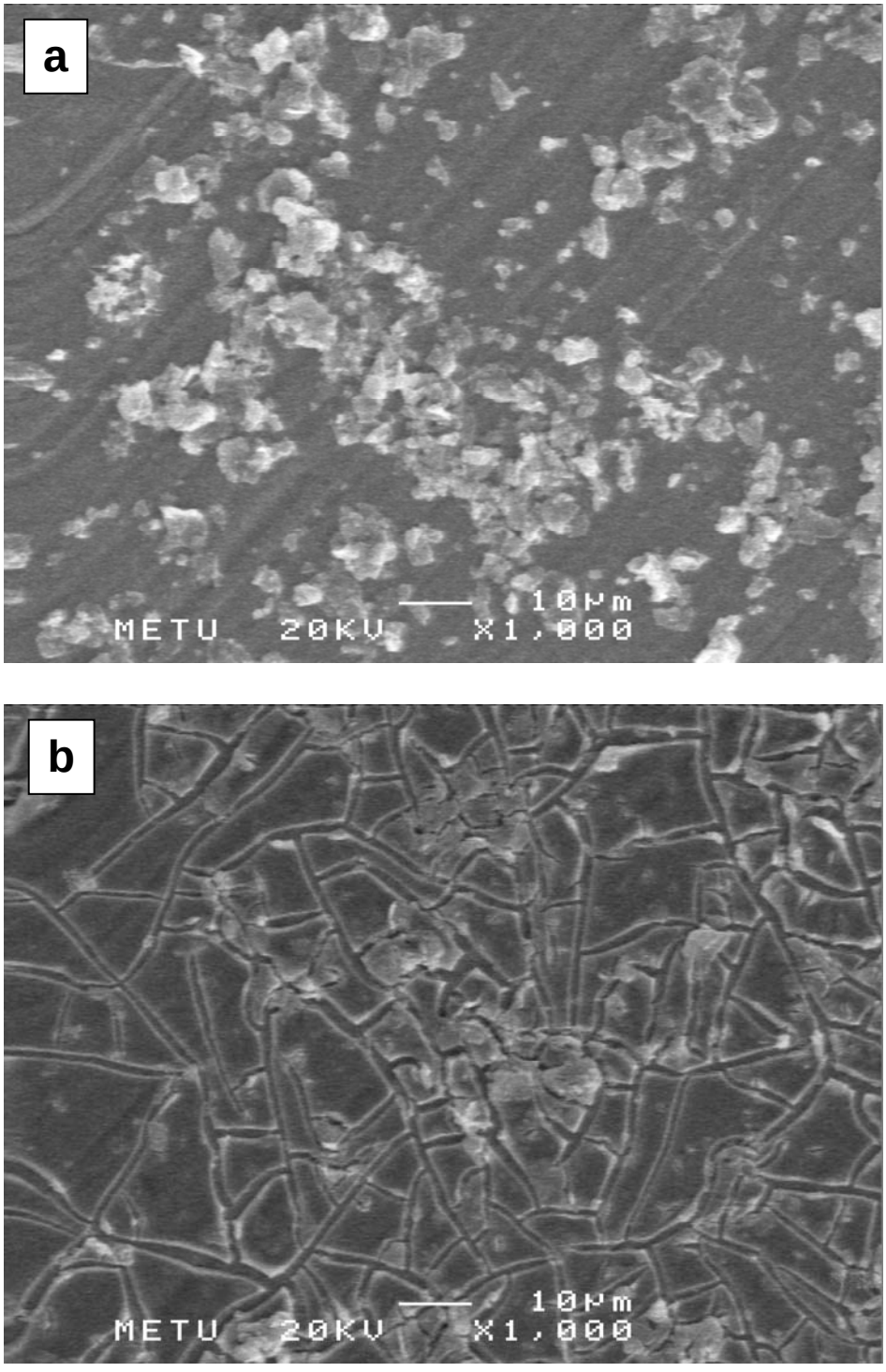

Figure 3.20 SEM images for the surfaces of HAp-titania hybrid coatings calcined at the same conditions in air at 500 ºC for 30 min. (a) single layer coating of Hybrid-I and (b) multilayered (three-time coated) Hybrid-I coating.

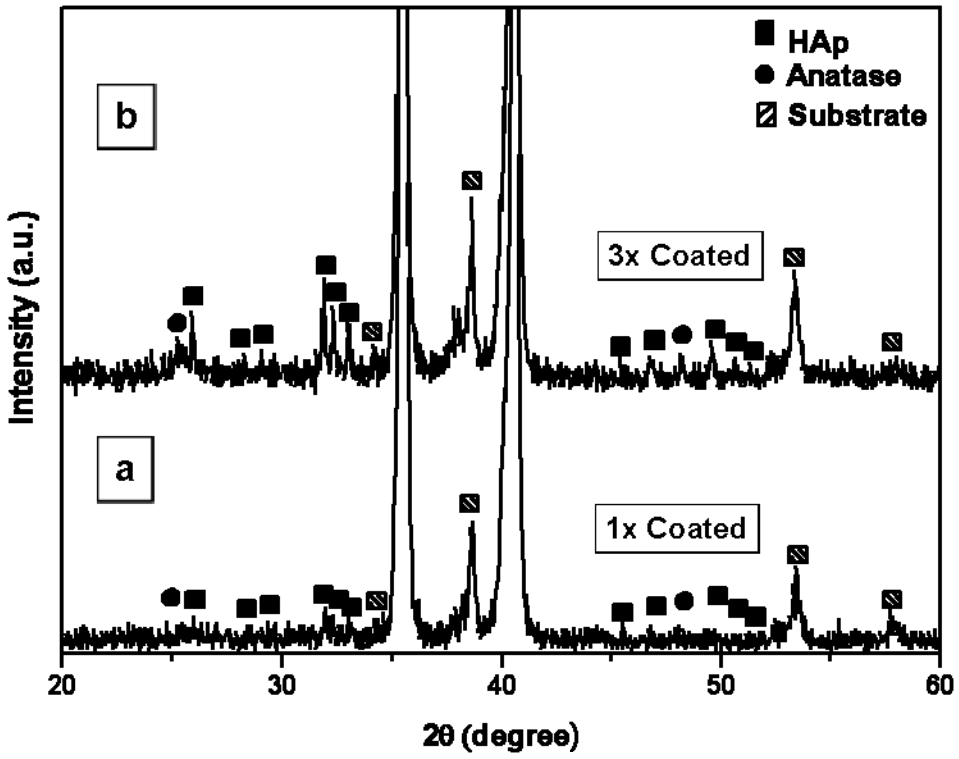

Figure 3.21 XRD diffractograms of HAp-titania hybrid coatings calcined at the same conditions in air at 500 ºC for 30 min. (a) single layer coating of Hybrid-I and (b) multi layered (three-time coated) Hybrid-I coating.

3.2.2. Morphology and phase identification of the coatings

Before investigating the coating properties further in detail, a set of experiments was performed to ensure the deposition and presence of the HAp-titania coating on the substrate in as-prepared condition. The reason for such analyses was two-fold. First, all the XRD analyses performed in the thesis have been obtained by conventional XRD setup with the geometrical arrangements suitable for powder and bulk sample analyses with limited capacity towards examining the thin films and coating. As a result, detection of a thin amorphous layer may be poor or deficient. Secondly, the titania coatings are on a titanium based substrate, making the phase identification more complex and sometimes misleading.

These two points are presented in the SEM micrographs in Figure 3.22. Figure 3.22a shows the SEM micrograph of a three-time Hybrid-II coated sample of the HAp-titania coating in as-prepared condition. Figure 3.22b is SEM image of the same coating obtained at a higher magnification. According to this Figure, a coating film encapsulates the HAp powders and some branched thin micro-cracks in this matrix are observable, confirming deposition of the coating material on the metal substrate.

Also, in this SEM picture the signs for uneven or incomplete coverage such as polishing marks on substrate can not be seen. Similarly, the SEM image in Figure 3.22b shows the details of the same coating at higher magnification showing the HAp particles are embedded in a continuous but locally cracked coating covering the metal surface. These SEM examinations can be correlated with the XRD results shown in Figure 3.23 displaying the XRD diffractograms of the same coatings. As it is shown in Figure 3.23a, in as-prepared condition coating show limited amount of titania (anatase) phase at around $2\theta=25^{o}$, whereas the peaks for other coating

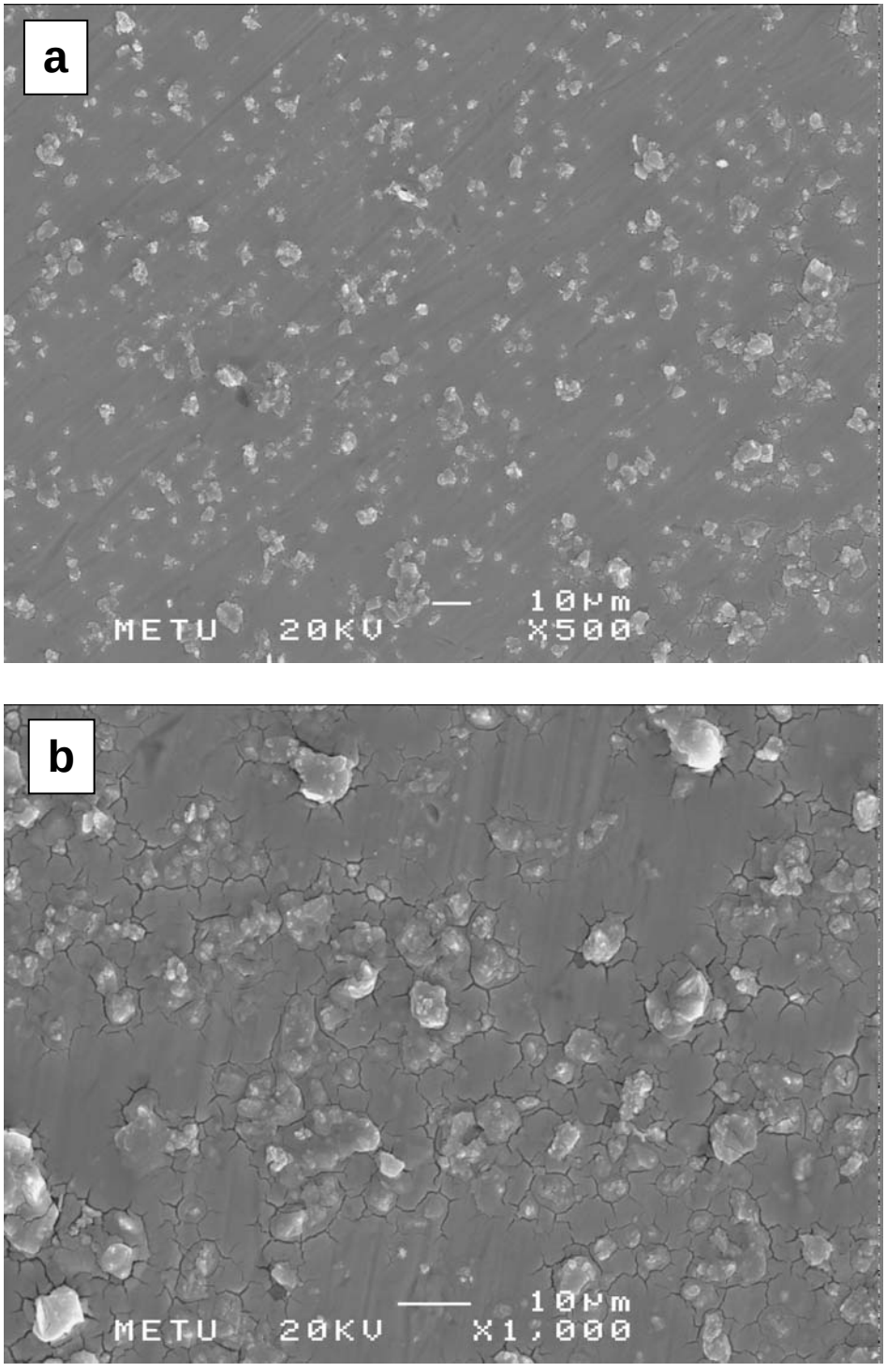

Figure 3.22 SEM images for the surfaces of multilayered (three-time coated) Hybrid-II coating in as-prepared condition (dried at 100 ºC for 1.5 h) taken at (a) low magnification (x500) and (b) high magnification (x1000).

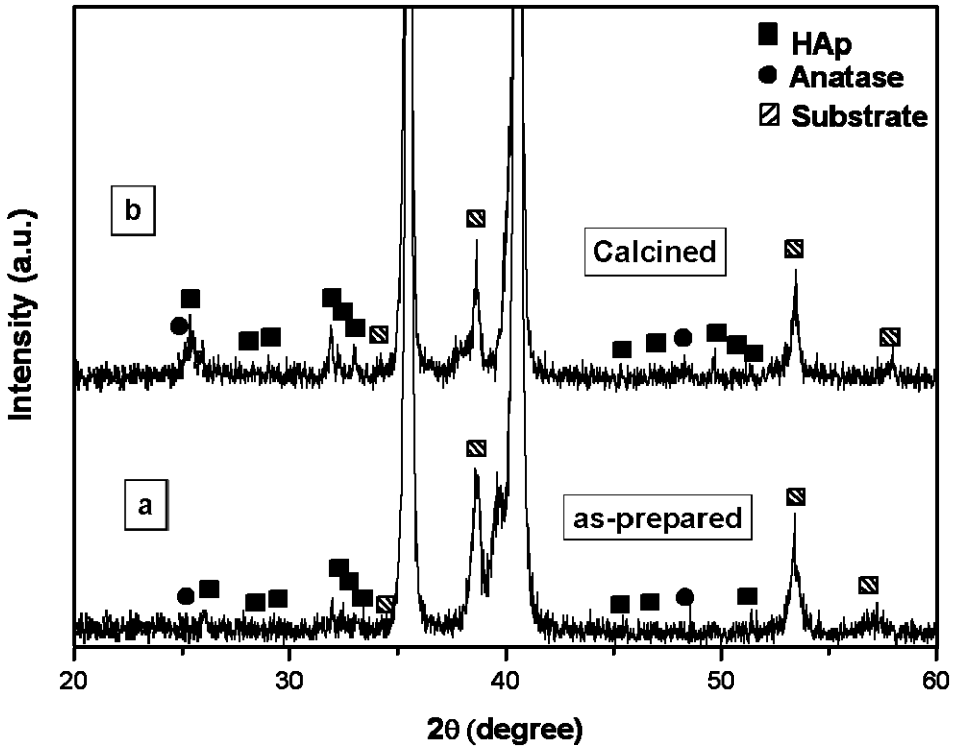

Figure 3.23 XRD diffractograms of multi layered (three-time coated) HAp-titania Hybrid-II coatings (a) in as-prepared condition (dried at 100 ºC for 1.5 h) and (b) after calcination for 30 min at 500 ºC.

component HAp (e.g. set of peaks at around 2θ = 32-33º) as well as Ti alloy substrate can be seen more clearly. This suggests that XRD peaks for titania phase may not represented in the XRD diffractograms , or may be detectable at limited extent due to amorphous nature in as-prepared condition and also due to very limited thickness.

A uniform coating as revealed by the SEM pictures can be confirmed only by careful interpretation of the XRD data. The indicators for presence of the coatings - after calcination- in the XRD diffractograms are HAp peaks (2θ = 32-33º) and the titania (anatase) phase at around 2θ=25º.

3.2.3. Effect of sol-gel formulation on coating properties

In the previous sections two multilayered HAp-titania coatings with distinct structural difference have been mentioned without discussing any processing related details for such variation. As can be seen in Figure 3.20b, in one coating cracking is a critical problem; on the other hand, the film formation was achieved without that much crack formation for another three-layered coating as depicted by Figure 3.22b. Crack formation and the microstructural difference in the coatings are both controlled by the type of the coating sol formulation used. XRD analysis of three-time coated, subsequently calcined samples were shown before in Figure 3.20b and Figure 3.23b, were produced by using two different coating formulations named as Hybrid-I and Hybrid-II, respectively. The major difference in composition was the presence of different organic solutions in the case of Hybrid-II. In this section, the distinctions and reasons for the morphology differences for HAp-titania hybrid coatings with two formulations (Hybrid-I and Hybrid-II coatings) were compared and discussed.

As previously shown in XRD analysis, both Hybrid-I and Hybrid-II coatings display resembling features. HAp phase peaks, the strongest peak for anatase located at around 2θ=25º, coming from the titania matrix of the coatings can be distinguished. The general EDS analyses performed from representative SEM images of both coatings given in Figure 3.24 also show similar features that give clues regarding to Ca and P elements of the HAp powders. SEM results disclose the differentiations for the features of those two coatings related to titania matrix. Figure 3.25 shows the SEM micrographs of three-time coated Hybrid-I and Hybrid-II coatings calcined for 30 min at 500 ºC. As shown in Figure 3.25a, Hybrid-I coating offers randomly dispersed HAp coating and titania matrix with macro-crack network. On the other hand, as it is displayed in Figure 3.25b, Hybrid-II coating have again random but relatively more uniformly disturbed HAp powders included in titania matrix with some micro-cracks.

Crack formation and the microstructural difference in the coatings are both controlled by the coating sol formulation used. The crack development is related to evaporation and drying behavior of the coating solutions mainly controlled by the organic constituents in the titania forming sols. The difference in solution vapor pressure of these two sols is a parameter that reflects the evaporation behavior of the organics during drying and subsequent calcination. Table 3.3 shows the vapor pressures for the individual chemical ingredients used in the formulations of Hybrid-I and Hybrid-II coating sols.

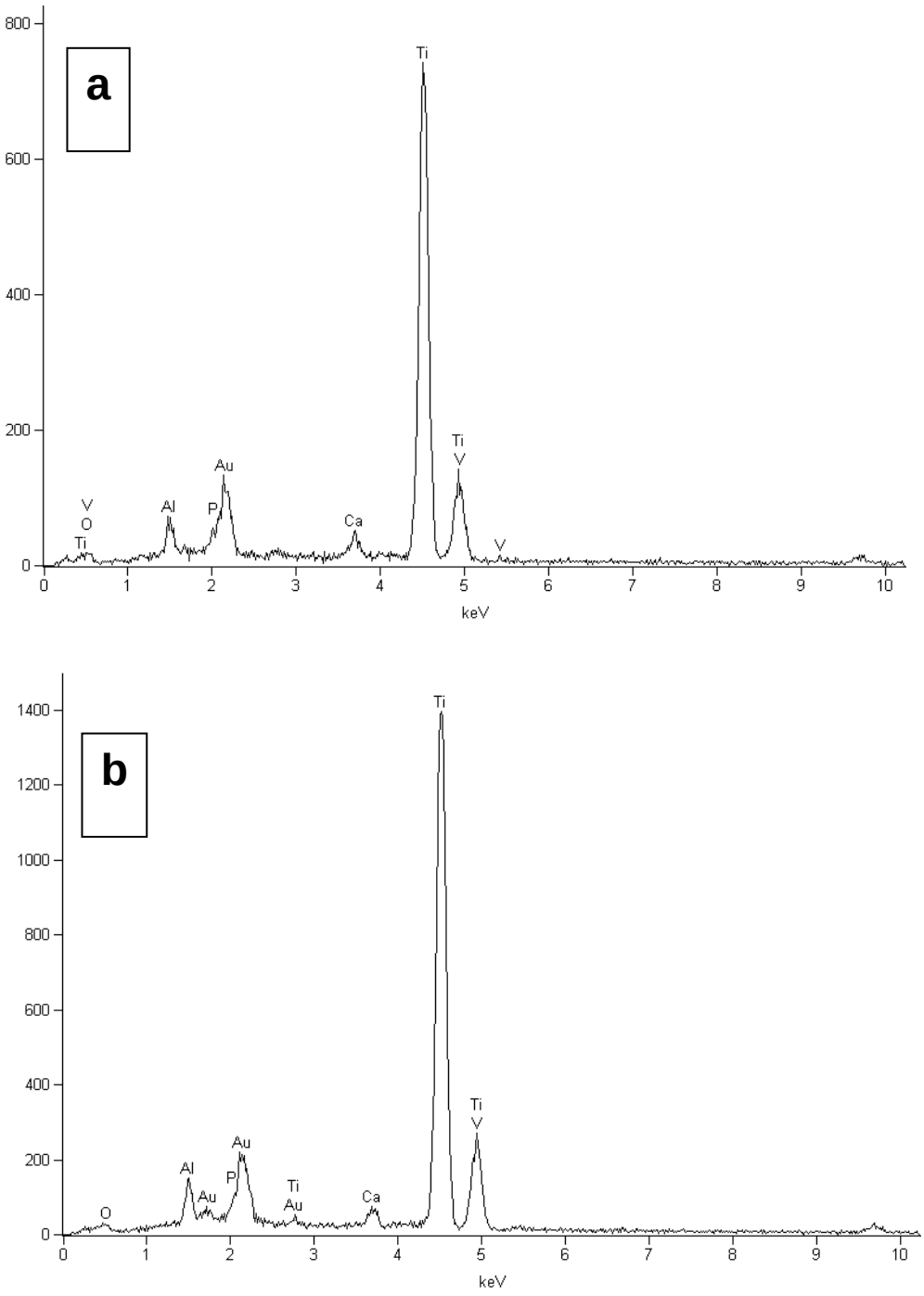

Figure 3.24 EDS spectra of multi layered (three-time coated) HAp-titania hybrid coatings calcined at the same conditions in air at 500 ºC for 30 min. (a) Hybrid-I and (b) Hybrid-II samples.

Table 3.3 Vapor pressure and boiling temperature values of the organic precursors of Hybrid-I and Hybrid-II sol [Adapted from Material Safety Data Sheets].

MATERIAL	VAPOR PRESSURE (mm Hg) at 20 ºC	BOILING TEMP. (ºC) at 760 mmHg
Ti-isopropoxide	N/A	232
n-propanol	14.5	97.4
acetyl acetone	6	139-141
nitric acid	62	86
ethanol	44	78

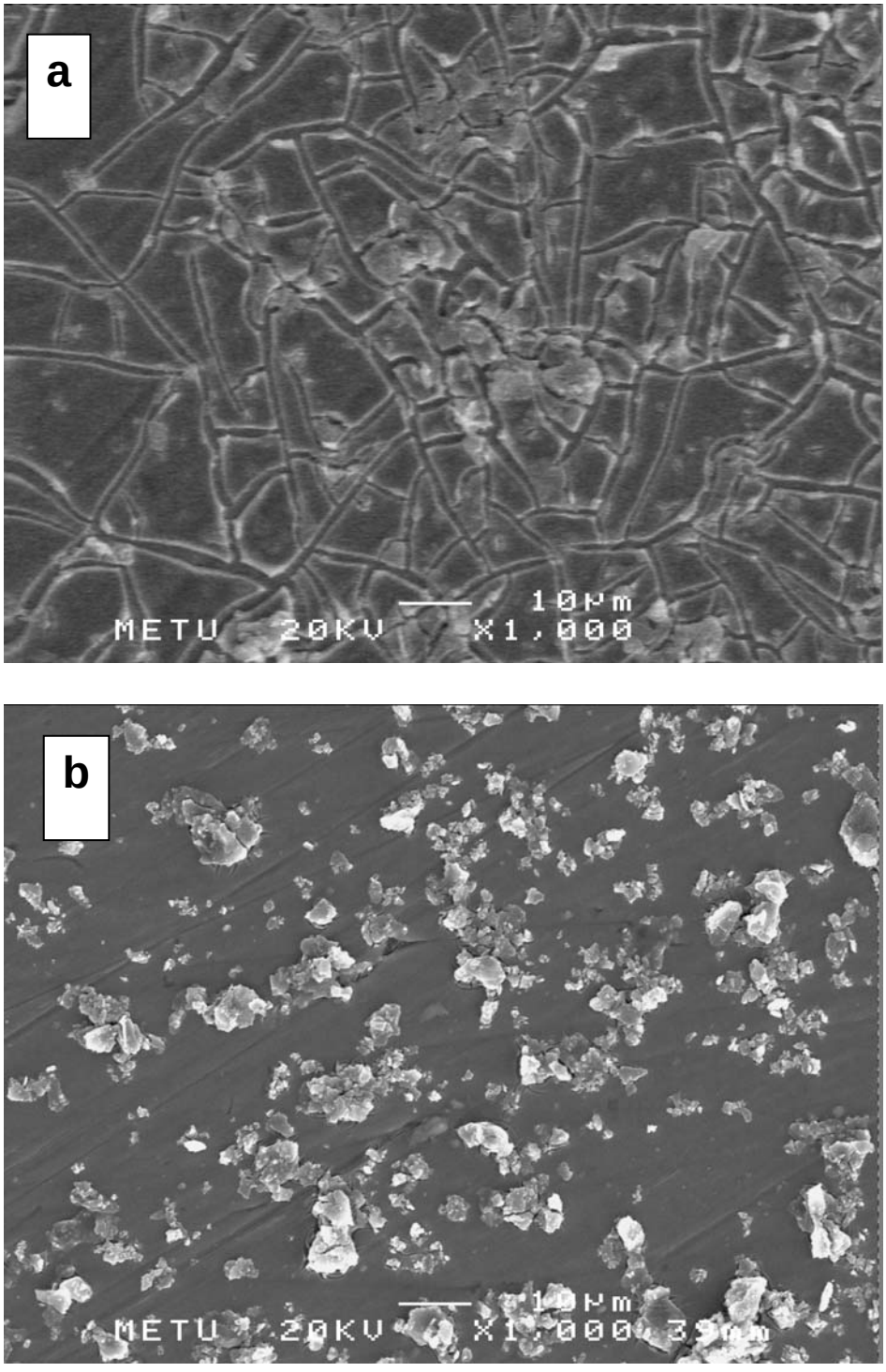

Figure 3.25 SEM analysis of three times coated (a) Hybrid-I and (b) Hybrid-II samples.

Hybrid-I is mainly composed of Ti-isopropoxide, ethanol and small amount of nitric acid catalyst. Hybrid-II sol additionally contains acetyl acetone and *n*-propanol replacing ethanol of Hybrid-I sol and all the ingredients of Hybrid-I sol. Acetyl acetone and *n*-propanol have vapor pressure of 14.5 and 6 mmHg respectively**,** whereas the major chemical component in Hybrid-I ethanol has relatively much higher vapor pressure of 44 mmHg. Therefore, on average Hybrid-I has higher vapor pressure compared to that of Hybrid-II. The relation between the rate of evaporation and the vapor pressure is formulized as:

$$\text{Rate of Evaporation} = V_E = H(p_W - p_A) \tag{3.5}$$

where V_E indicates the evaporation rate of the liquid, H is a factor depending on the temperature, drying atmosphere and the geometry of the system [55]. p_W and p_A are the vapor pressure of the evaporating liquid at the surface and ambient vapor pressure, respectively. The effect of ambient vapor pressure can be neglected for our system as all the drying and calcination procedures were performed in the same atmospheres. The stress at the surface of the planar substrate during evaporation of a liquid layer is given by:

$$\text{Drying Stress} = \sigma_x \approx \frac{L \cdot \eta_L \cdot V_E}{3K} \tag{3.6}$$

where η_L is the viscosity of the liquid and L is the half thickness of the layer, and K an atmosphere dependent parameter [55]. Accordingly, cracking due to evaporation is more likely to occur if the drying rate or the coating layer is thick. Thus, Hybrid-I sols with higher vapor pressure evaporate and dry-out faster compared to Hybrid-II leading to a higher stress build-up in the coating layer.

The cracking behavior depends on evaporation-related to the macroscopic stress (σ_x) to some extent. However, this macroscopic stress is amplified in the presence of discontinuities that actually cause the fracture. In HAp-titania hybrid coatings, HAp particles embedded in the titania matrix act as local stress raising flaw sites and the crack initiation begins from the attachment point of HAp particles with titania matrix. This is due to the local vapor pressure variance at the neck-like convex contact point at the HAp powder embedded in titania. Under isothermal conditions the curvature of a surface increases the effective vapor pressure. Thus, the tip of the convex surface of HAp-gel attachment or the meniscus at the contact point is the first site to evaporate and following crack prolongation is controlled by the overall vapor pressure of the gelling solution. In this case, for both Hybrid-I and Hybrid-II coatings, drying cracks are formed; however, longer and thicker cracks are observed for the Hybrid-I coatings because its higher vapor pressure and higher macroscopic drying stress, σ_x. As a result, both Hybrid-I and Hybrid-II sol formulations have a potential for forming HAp-titania coatings as confirmed by XRD and SEM analyses. However, Hybrid-II coatings offering a better structural integrity and minimal crack formation were investigated further in the thesis.

3.2.4. Modification on coating properties

In order to control the microstructure, different coating processes parameters were manipulated:

i. withdrawal rates used during th dipping process.

ii. calcination temperature.

iii. HAp particle size.

The influence of these parameters on coating properties such as crack formation, general morphology and the amount of HAp powders adhered on to the substrate were investigated by XRD and SEM.

3.2.4.1. Effect of withdrawal rate

All the coatings presented up to this point were produced at a withdrawal rate of 16 cm/min. Similarly, coatings from the same sol-gel formulation were made at two different rates, at 9 cm/min and 22 cm/min. Comparative data related to coating thickness, HAp adhesion and morphology are presented here.

The effect of substrate withdrawal rate on coating properties is also illustrated by the SEM and accompanying XRD results. Figure 3.26 shows the SEM micrographs of the samples deposited using two different withdrawal rates of 9 and 22 cm/min, respectively. The amount of the titania coating matrix deposited increases when faster rates are used as the scratch tracks of the underlying metallic substrate due to polishing are covered in the case coating made with a withdrawal rate of 22 cm/min. Additionally, the coating deposited at faster rate does not exhibit coating matrix cracking. Figure 3.27 shows the XRD data for the samples prepared by different withdrawal rates, at 9 cm/min, 16 and 22 cm/min, showing typically similar diffraction intensities for the HAp component and therefore almost a constant amount of HAp deposition independent from the withdrawal rate. These two observations indicate that the thickness of the titania matrix increases with the withdrawal rate. Therefore, for the samples dip coated with lower withdrawal rates, relatively more HAp powders are embedded in a thin titania film.

The measured coating thicknesses are shown in Table 3.4. These results are representative for the titania film layer thickness. The coating thickness changes with the number of coating operations and also with the withdrawal rate. For the samples produced with standard withdrawal rate of 16 cm/min, the titania thickness for single-step coated sample is found as 0.120 μm which increases to 0.810 μm for multilayered (three-time coated) film. The coatings thickness also increases with withdrawal rate and varies in the range of 0.65-1.1 μm, for the three-time coated

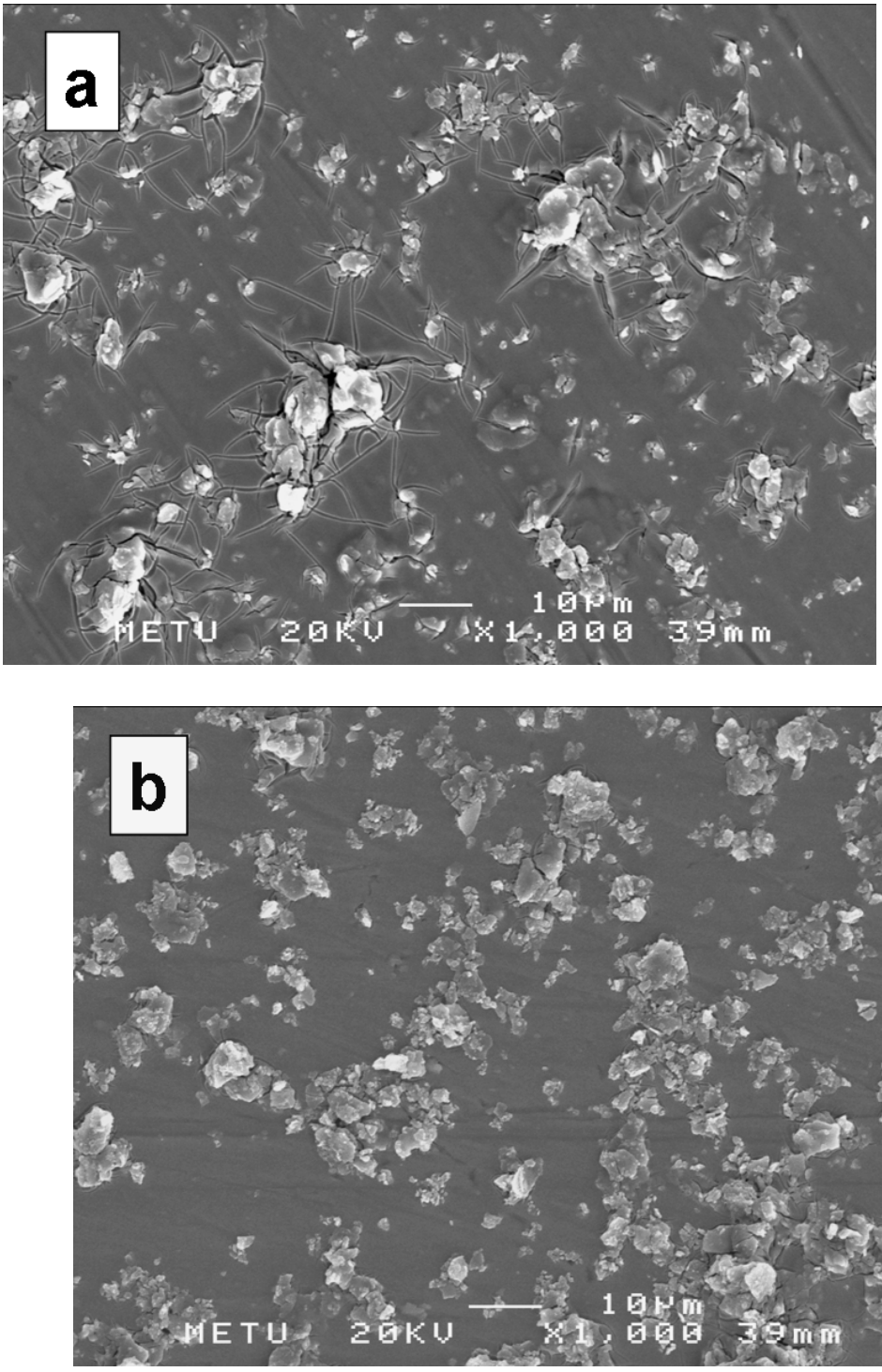

Figure 3.26 SEM images of the surfaces of multilayered (three-time coated) HAp-titania films obtained by using Hybrid-II formulation dip coated at withdrawal rate of (a) 9 cm/min and (b) 22 cm/min. The calcination was performed at the same conditions in air at 500 ºC for 30 min.

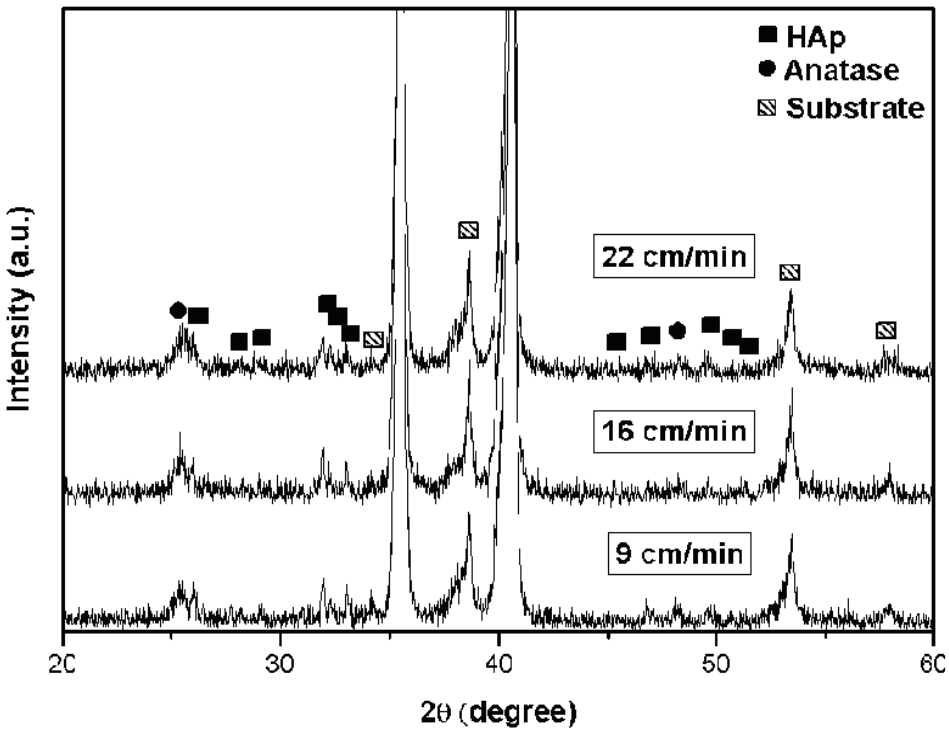

Figure 3.27 XRD diffractograms of multilayered (three-time coated) HAp-titania films obtained by using Hybrid-II formulation dip coated at withdrawal rate of (a) 9 cm/min , (b) 16 cm/min and (c) 22 cm/min. The calcination was performed at the same conditions in air at 500 ºC for 30 min.

Table 3.4 The thickness of HAp-titania films dip coated different times or at various withdrawal rates and samples were both calcined in air at 500 ºC for 30 min.

Coating	Number Of Layers	Withdrawal Rate (cm/min)	Thickness (μm)
Hybrid-II	1	16	0.120±0.50
Hybrid-II	2	16	0.400±0.100
Hybrid-II	3	16	0.810±0.100
Hybrid-II	3	9	0.650±0.100
Hybrid-II	3	22	1.110±0.100

samples obtained with withdrawal rates of 9 cm/min and 22 cm/min, respectively. Similar findings on the change of coating thickness with the withdrawal speed are also available from related previous works. The relation between thickness and withdrawal velocity is shown in the equation derived by Landau and Levich below [54].

$$h=0.94(\eta U)^{2/3}/\gamma_{LV}{}^{1/6}(\rho g)^{1/2} \quad (3.7)$$

where h indicates the thickness of the coating, U symbolizes the withdrawal velocity, γ_{LV} reveals the liquid-vapor surface tension and g is the gravitational force. According to Equation (3.8), the coating thickness is proportional to the adjusted

withdrawal velocity of the dip coating machine. This $h \alpha U^{2/3}$ relation is also confirmed for the polymeric systems by Brinker and Ashley [34]. Another study for the thickness withdrawal speed relation was reported by Strawbridge and James [55] and where thickness-viscosity-withdrawal speed correlation for acid catalyzed TEOS solutions was investigated for withdrawal velocities from 5 to 15 cm/min.

The properties of HAp-titania hybrid coatings in terms of the withdrawal rate and coating thickness dependence are in agreement with the classical behavior expected from the sol-gel coatings. Typically, coating thickness increases with the withdrawal speed observed by SEM investigations as the scratch tracks disappear by increased withdrawal rate. As shown in Figure 3.26, crack formation occurs at higher extent at slow withdrawal rates. One source for cracking might be evaporation rate controlled macroscopic stress as discussed earlier. However, SEM images of Figure 3.26 imply more severe cracking in the case of thinner coatings formed at a slower withdrawal rate, controversial to relationship given in Equation (3.6).

The details of coatings microstructure corresponding to the slowest and fastest withdrawal speeds with higher magnification SEM micrographs are again shown in Fig 3.28 Crack formation occurs at higher extent at slow withdrawal rates.

Another source for cracking is the local factors related to physical interaction between solid HAp powders and titania matrix producing lateral forces during dip coating withdrawal step. This factor becomes more critical in the presence of relatively higher amount of solid HAp particles in a thin titania layer. Thickness of titania matrix is important since HAp powders apply radial load to titania layers during vertical withdrawal and this might lead to radial crack formation. The radial

stress that may loosen the coating by bending on thickness of the layer is indicated in the following equation (3.8).

$$\sigma = \left(\frac{P}{Bd^2}\right)\log\left(\frac{CE_c}{E_S}\right) \tag{3.8}$$

Here, *d is* coating thickness and *P* is concentrated load at the surface, E_c and E_s exhibits Young's modulus of the film and substrate respectively and B and C are dimensionless coefficients [56, 57]. According to Equation (3.9)**,** maximum stress is highly dependent on *d* indicating that thin films are more susceptible for this type of crack formation [56]. Therefore, slow withdrawal speed preferentially decreases the amount of titania sol attaching to the surface produces thinner coatings containing more HAp particles acting more effectively as radial micro-crack sources.

3.2.4.2. Effect of calcination temperature

Coating properties and microstructure also change according to another critical processing parameter, i.e. calcination temperature. In addition to the standard 500 ºC calcination, two other temperatures were chosen for the post-treatment of coatings at 400 ºC and 600 ºC. Figure 3.29 discloses the XRD analyses of the hybrid coatings post-treated at 400 ºC, 500 ºC and 600 ºC, respectively. At low calcination temperature (400 ºC) there is no sign for presence of titania. This is due to very limited thickness of the amorphous titania layer. But the diffraction peaks of HAp confirm presence of the hybrid coating on the surface. Titania peaks can be seen for the coatings calcined temperatures higher than 500 ºC and 600 ºC. Amorphous sol-gel titania coating first crystallizes to anatase somewhere in the temperature range of 400-500 ºC. Formation of higher temperature polymorph

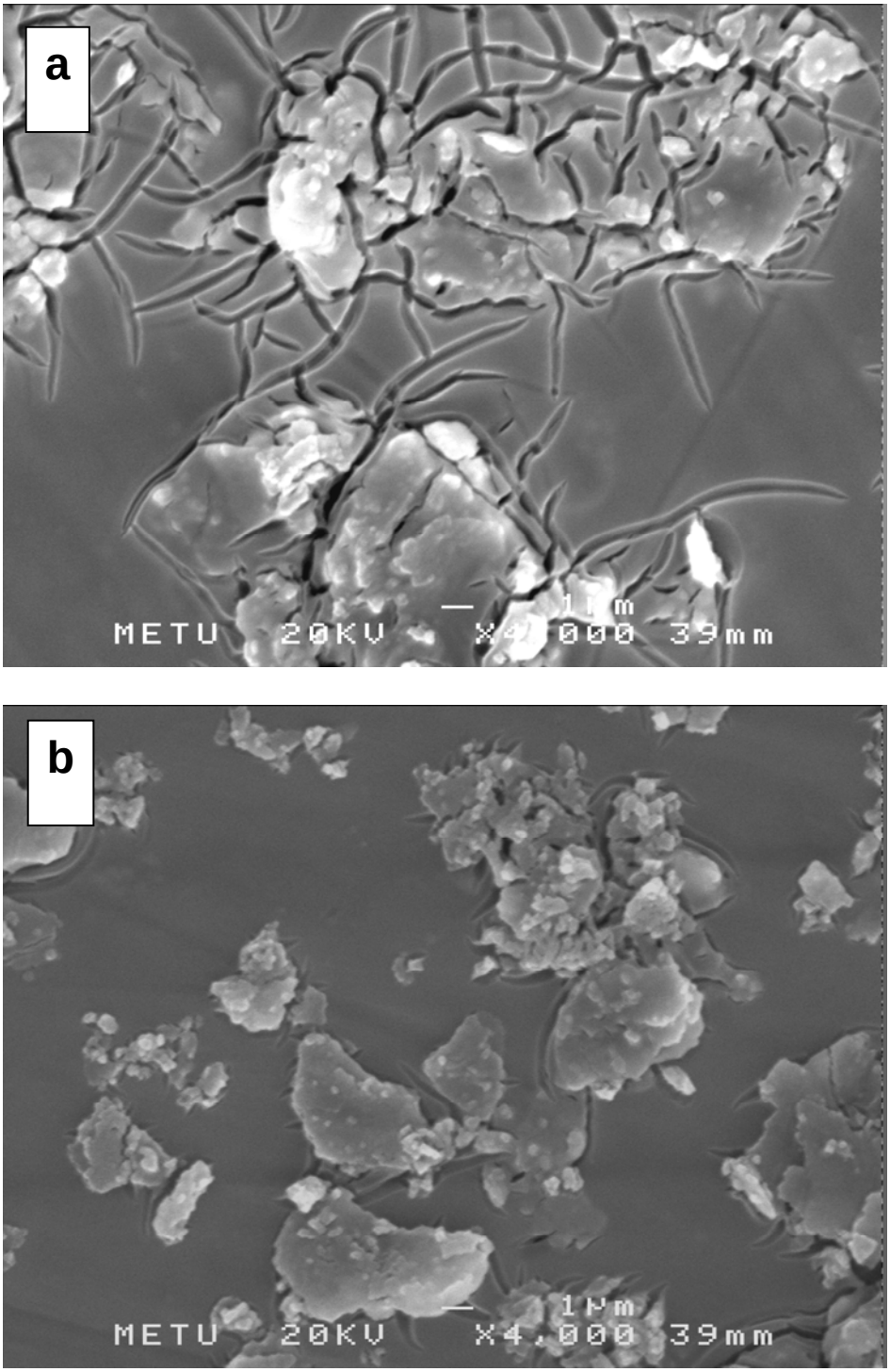

Figure 3.28 SEM images of the surfaces of multilayered (three-time coated) HAp-titania films obtained by using Hybrid-II formulation dip coated at withdrawal rate of (a) 9 cm/min and (b) 22 cm/min with higher magnification correspond to 1μm. The calcination was performed at the same conditions in air at 500 ºC for 30 min.

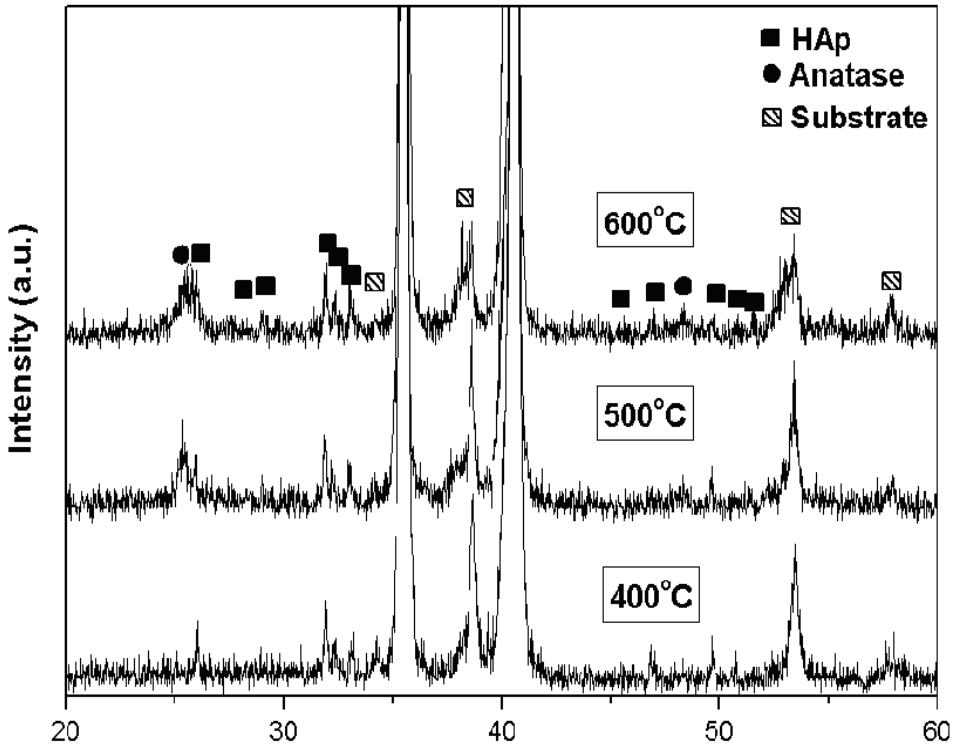

Figure 3.29 XRD diffractograms of multilayered (three-time coated) HAp-titania films obtained by using Hybrid-II formulation calcined at 400º, 500º or 600 ºC for 30 min. The withdrawal rate was 16 cm/min in all cases.

-rutile- does not seem to be formed even at 600 ºC. The rutile diffraction peaks are not clear at 500 ºC and 600 ºC.

For the range (400-600 ºC) used in this study calcination temperature does not lead some changes in the crystal nature of the phases. There is obviously no phase transformation for HAp component in this temperature range and crystalline HAp stays unchanged. Calcination mostly affects the identity of the amorphous titania matrix. Crystallization to anatase occured somewhere in 400 ºC-500 ºC and crystallization to rutile was not obvious in this study. Coatings calcined at 500º and 600 ºC are comparable in terms of the chemical identity of the phases.

The calcination temperature more critically affects the microstructure of the coating. Higher calcination temperature leads to macrocracking as shown in Figure 3.30 displaying the SEM images of the HAp-titania hybrid coatings calcined at 400 ºC and 600 ºC for 30 min.

The homogeneity and coverage of the titania matrix remains unchanged due to different calcination temperatures in the range of 400-600 ºC. The roughness of the titania matrix is comparable and relatively smooth at samples calcined at 400 ºC as well as for the sample calcined at 600 ºC. But obviously both micro- and macro-cracks in titania matrix form at higher calcination temperatures. This cracked network is due to the high temperatures approaching to practical sintering conditions. At around densification range the intrinsic stress due to densification of the coating under constraint and thermal stress on cooling both intensify.

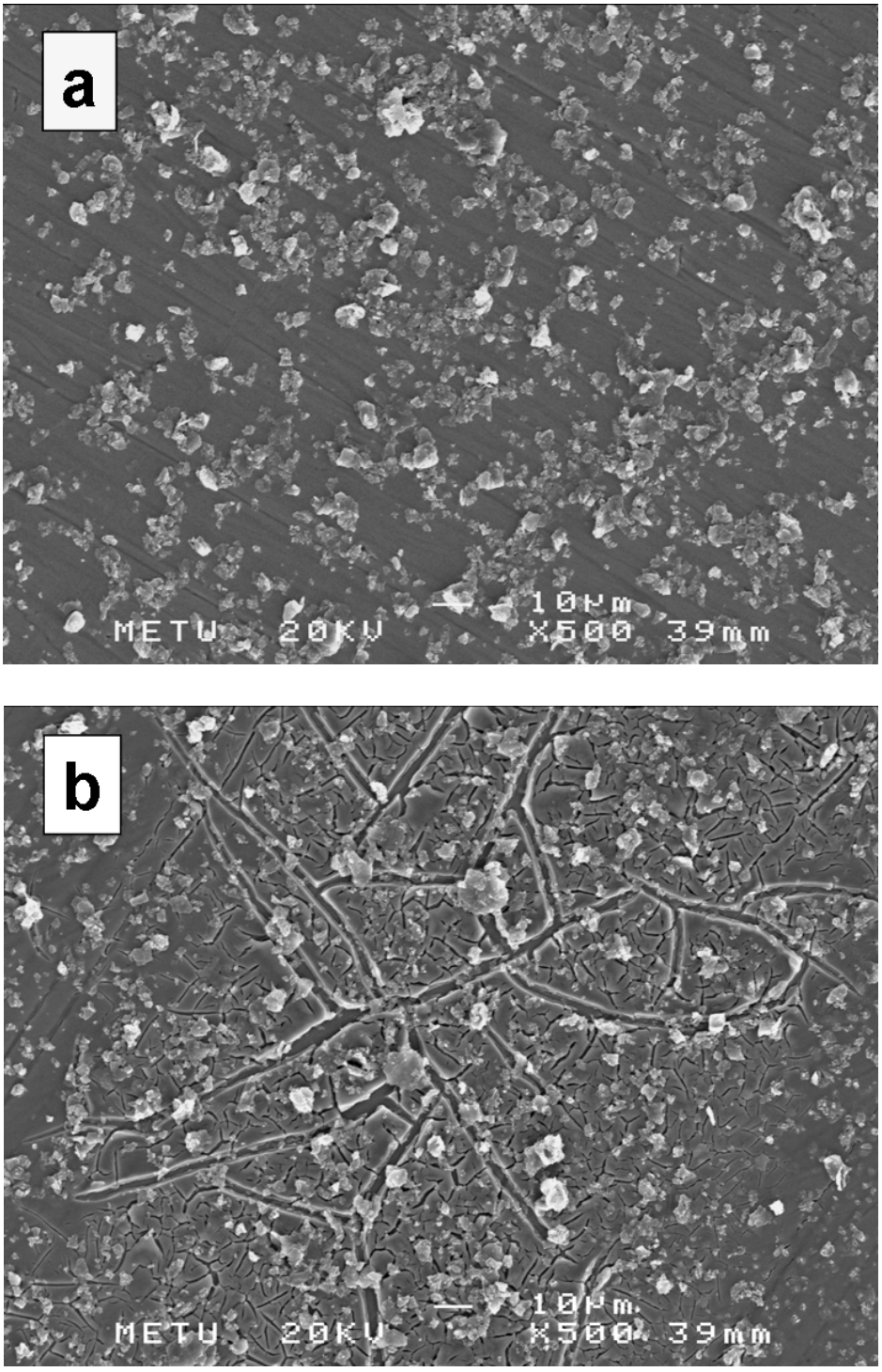

Figure 3.30 SEM micrographs of the surfaces of multilayered (three-time coated) HAp-titania films obtained by using Hybrid-II formulation dip coated with withdrawal rate of 16 cm/min calcined (a) at 400 ºC for 30 min, and (b) at 600 ºC for 30 min.

3.2.4.3. Effect of HAp powder size

The effect of HAp powder size on coating properties are shown with the SEM micrographs in Figure 3.31. This Figure show two coating produced using HAp-III or HAp-II. As discussed in the HAp powder synthesis section, HAp-III with a plate like morphology is composed of particles ranging in the size range of 10-20 μm.

The other HAp powder employed on the other hand, i.e. HAp-II was much smaller in the as-synthesized condition it look as reticulated sub-micron size HAp crystals. This Figure shows a typical features of the rough surface for the hybrid coating. However homogeneously dispersed HAp particles are obviously smaller when HAp-II powders were employed. It looks like that that the irregular shaped agglomerates for HAp-II were dispersed in the solution and, sub-micron particles can be seen from the micrograph for HAp-II substituted Hybrid-II coating. Figure 3.32 displays the XRD analysis of HAp-II substituted hybrid coatings. As it is shown in the Figure, XRD features are similar compared to HAp-III containing coatings. EDS analysis was also employed for the confirmation of the HAp and titania phases. The results were taken at 500x magnification and are shown in Figure 3.33. It displays almost the same features as HAp-III substituted coatings. All elemental peaks of the substrate and HAp are observable. The use of smaller HAp powders can be beneficial in terms of making coating with more uniform microstructure.

3.2.5. Effect of pore generators

Porosity is a significant functional requirement for hard tissue implants, where a network promotes the bone ingrowth and provides better attachment of bone with the implant. This section briefly discusses the attempts for achieving a controlled

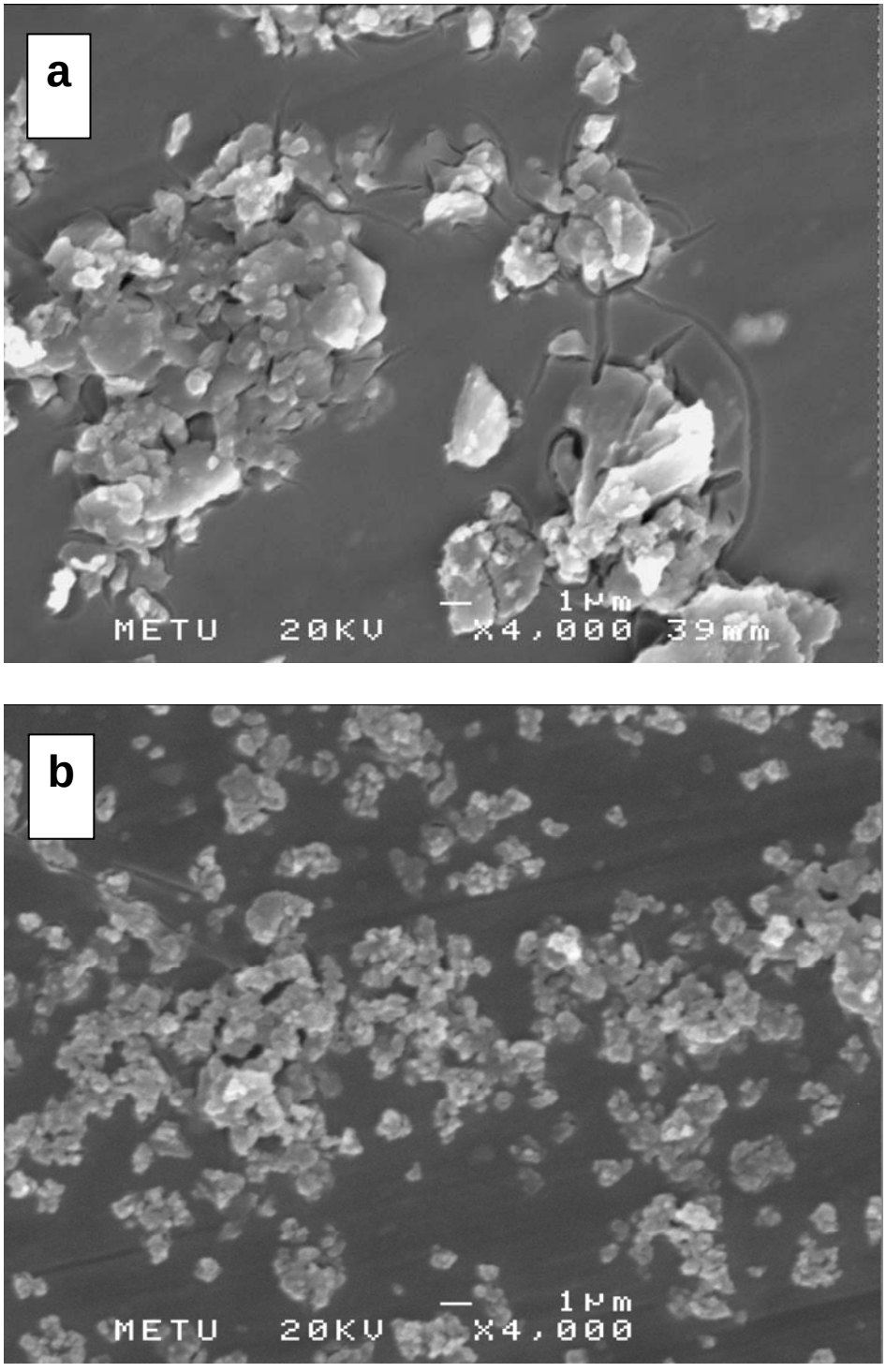

Figure 3.31 SEM micrographs of multilayered (three-time coated) HAp-titania films obtained by using Hybrid-II formulation dip coated with withdrawal rate of 16 cm/min using HAp products of different precipitation reactions; (a) HAp-III of $Ca(NO_3)_2 \cdot 4H_2O$ and $(NH_4)_2HPO_4$, (b) HAp-II of $CaCO_3$ and $(NH_4)_2HPO_4$.

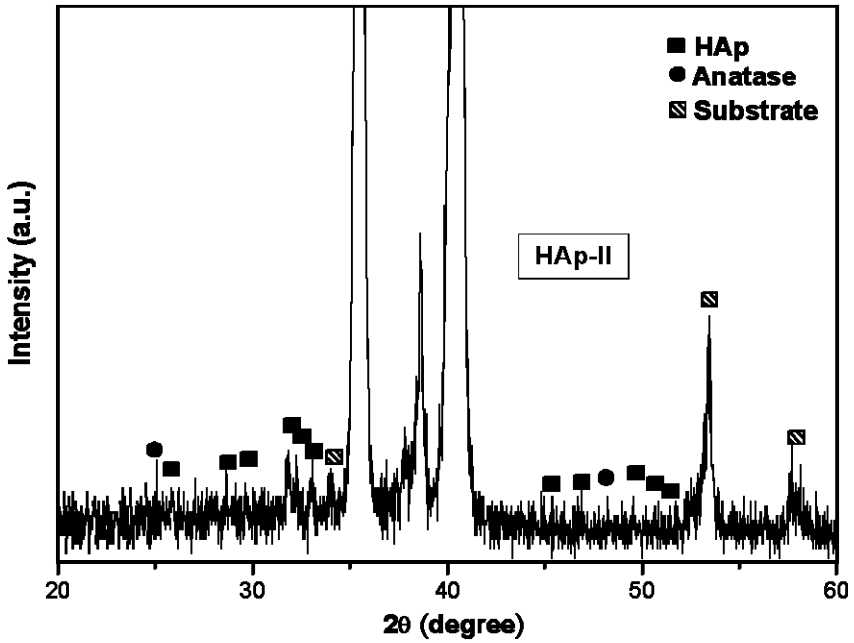

Figure 3.32 XRD diffractogram of multilayered (three-time coated) HAp-titania films obtained by using Hybrid-II sol-gel formulation dip coated with withdrawal rate of 16 cm/min using HAp-II product of $CaCO_3$ and $(NH_4)_2HPO_4$ precipitation reactions.

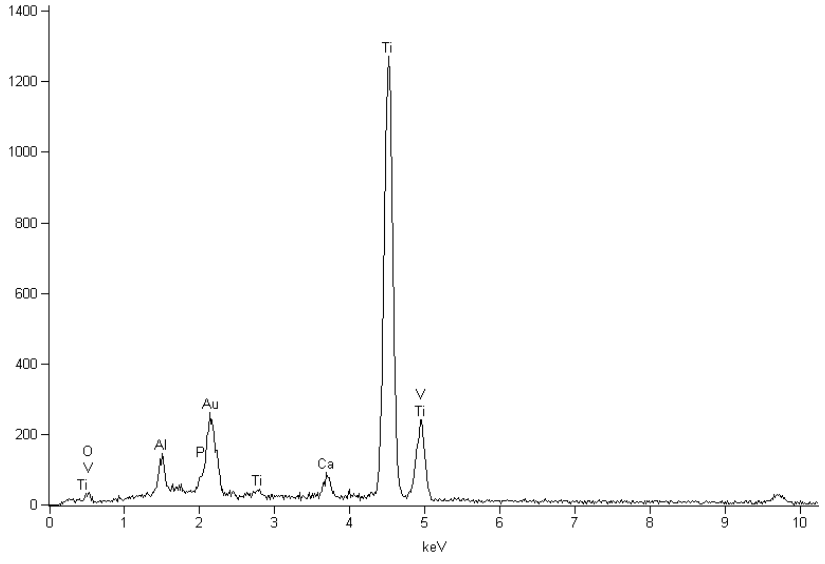

Figure 3.33 EDS spectra of multilayered (three-time coated) HAp-titania films obtained by using Hybrid-II sol-gel formulation dip coated with withdrawal rate of 16 cm/min using HAp-II, product of $CaCO_3$ and $(NH_4)_2HPO_4$ precipitation reactions.

porosity in the HAp-titania coatings by addition of a pore generator. NaCl powders were used to create openings in the matrix, which can be dissolved by leach out washing following the coating process. SEM, XRD and EDS analyses were used for the determination of the NaCl phases with HAp and titania and, the identification of the morphology before and after water treatment of the samples. The samples were prepared by the addition of solid NaCl granules (<40 μm) at NaCl:HAp= 1:1 molar ratio in to the coatings sols. The goal was to provide a porous structure by subsequent dissolution of the salt crystals after drying the coating. Water treatment was applied for 20 min.

Figure 3.34 reveals the XRD diffractogram of the three times coated HAp-titania-NaCl coating before and after water treatment, where the sharp and intense peak for NaCl is observable for unwashed sample. However, after water treatment for 20 min., the NaCl peak disappears indicating that the all NaCl powders were dissolved and washed away. The SEM micrographs for NaCl substituted hybrid coatings prior and latter to washing are displayed in Figure 3.35. For the micrograph before washing, the similar features are seen as the previous hybrid coatings. NaCl powders are observable and appear brighter than HAp powders. As it is shown, the microstructure of the coating changes after washing upon removal of NaCl particles. But, controlled porosity could not be achieved most probably due to thin titania matrix. On the other hand, this study gives some idea about the chemical durability of the coatings. As revealed by the XRD examinations there is no significant differences for the intensities of HAp phase and titania matrix before and after the water treatment, suggesting that the both of the coating components tolerate such aqueous treatment and coatings does not dissolve.

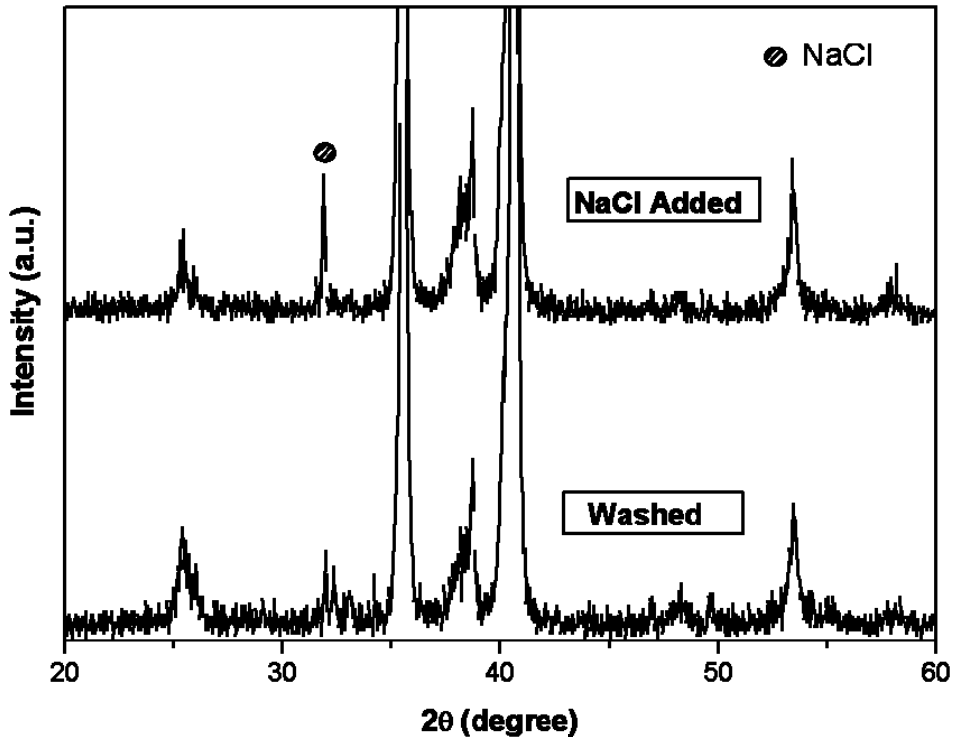

Figure 3.34 XRD diffractogram of multilayered(three-time coated) HAp-titania-NaCl coating (upper) before and (lower) after washing treatment. The water treatment was applied for 20 min.

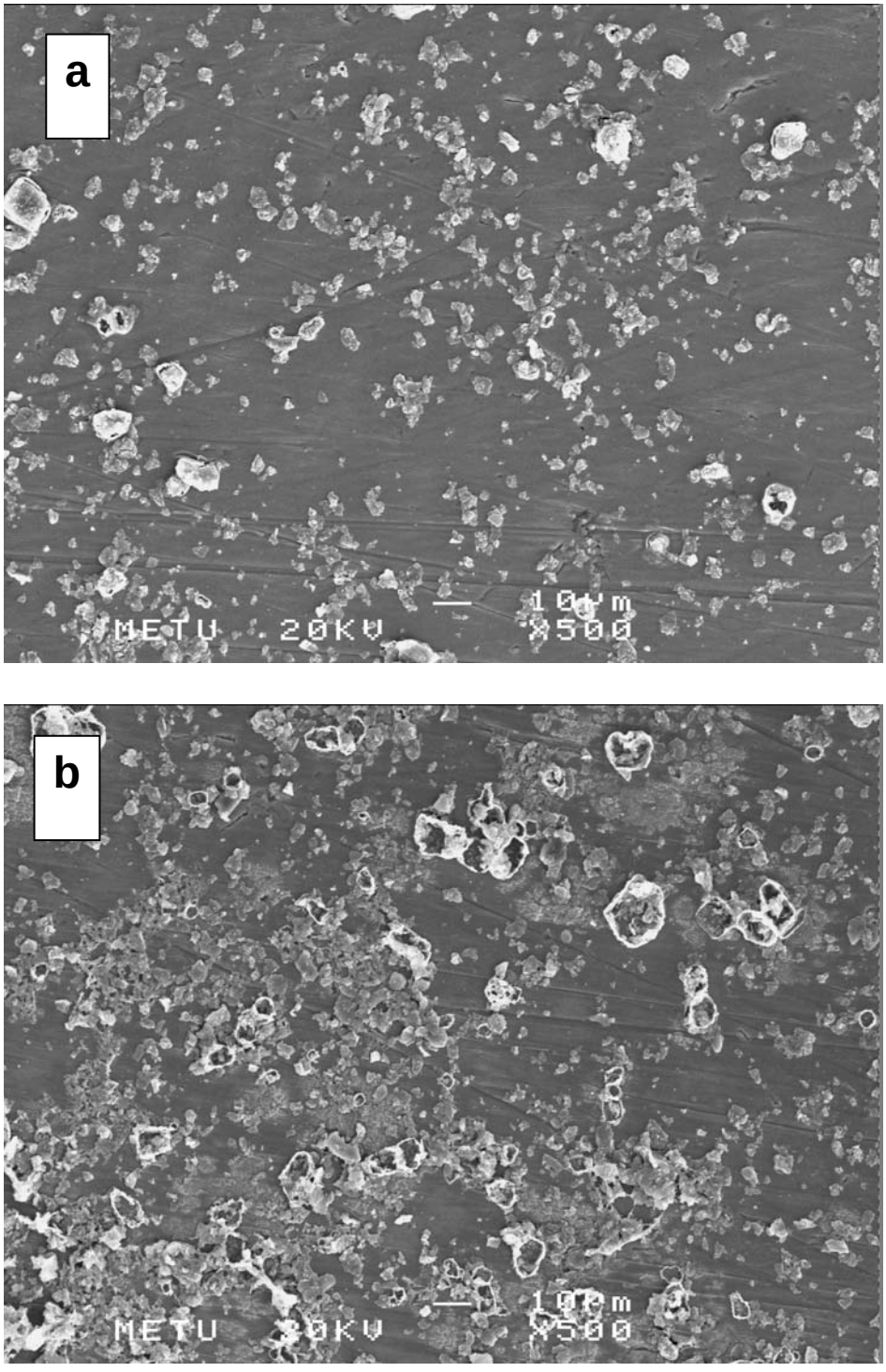

Figure 3.35 SEM micrographs of multilayered (three-time coated) HAp-titania-NaCl coating (a) before and (b) after washing treatment. The water treatment was applied for 20 min.

CHAPTER 4

CONCLUSIONS

Phase pure hydroxypapatite synthesis by precipitation method was accomplished. In addition, a sol-gel processing route for making HAp-titania hybrid coatings on Ti6Al4V alloy was developed. This part of study mainly focused on the phase and morphological investigations of the coatings. The general observations and findings for these two specific research themes are summarized as followings:

(i) Hydroxyapatite(HAp) powder synthesis:

Three different precursor couples were used to synthesize HAp powders: $Ca(OH)_2$ - H_3PO_4 [HAp-I], $CaCO_3$ - $(NH_4)_2HPO_4$ [HAp-II], $Ca(NO_3)_2.4H_2O$ – $(NH_4)_2HPO_4$ [HAp-III]. Phase and microstructure analysis of HAp powders were performed.

HAp-I synthesis occurred with the co-precipitation of another calcium phosphate phase -dicalcium phosphate dihydrate (DCPD). HAp-II, on the other hand, was obtained phase pure in as-precipitated condition. However, formation of CaO phase after calcination at 1000 ºC indicated a non-stoichiometry for this HAp. HAp-III was the most successful among all three routes used. Phase pure and stoichiometric HAp could be achieved.

The particle size of HAp could be controlled as supported by morphological investigations. HAp-I crystals have an average size of 0.5-1 μm from agglomerates with 2-20 μm size. HAp-II showed nano-sized crystals with irregular shaped agglomerates with a size up to 20 μm. Plate-like HAp-III, on the other hand, disclosed bigger particle size ranging 10-20 μm with no agglomerates. This distinction for the HAp powder size was strongly dependent to the solubility of the precursors which is also related to the saturation level of the ionic species in mother solution. Low solubility precursors (as in the case of $CaCO_3$ for HAp-II) leaded to high saturation indices which caused larger number of crystals with smaller size. Conversely, for HAp-III, bigger particle size was observed due to high solubility of $Ca(NO_3)_2 \cdot 4H_2O$.

According to FTIR results, HAp powders in as-precipitated condition are found to be carbonated apatite which is similar to the form of apatite in bone (calcium deficient and carbonated). However, only HAp-II among all three HAp powders was still carbonated after calcination.

(ii) HAp-titania Hybrid coatings:

HAp-titania coatings on Ti6Al4V were obtained by dip coating pretreated substrates into titania sols incorporated with HAp powders and subsequent maturing calcination treatments at 500 ºC for 30 min.

Coating thickness can be changed by a combination of processing parameters mainly, by multi layer coating application and withdrawal speed. The titania coating thickness can be controlled in the range of 0.120 μm-1.1 μm.

The macro scale structural integrity and coating morphology is mainly controlled by the overall thickness and also by drying behavior of the titania sol. Macro scale interconnected cracking occurred at a greater extent in the multilayered coatings or coating produced with faster withdrawal rates with relatively higher thickness values. The sol-gel formulation is another crucial factor leading to this type of cracking. Formation of a network of continuous macro cracked coating microstructure occurred greatly in the case of sols formed by liquid organic solvents with high liquid vapor pressure. The use low vapor pressure organic solvents decreases the macroscopic stresses during drying and drastically reduces the interconnected macrocrack formation problem.

The second factor determining the structural integrity was the related to physical interaction of solid HAp particles with the titania matrix during dip coating process. Relative proportions of the titania and HAp solid powders bonding on the substrate surface is determining factor for formation of microcracks originating around the HAp particles embedded in titania. Consequently, this problem becomes more obvious in the case monolayered thin hybrid coatings obtained at very withdrawal rates. Thin hybrid coatings with insufficient linkage of titania formed with slow withdrawal rates are found to be more vulnerable for this type of microcracking. This is due to greater local stresses caused by more HAp particles forcing thin titania film to detach by bending and due to more significant physical contact between solid HAp particles and liquid titania gel during withdrawal.

HAp-titania hybrid coatings can be widely used for orthopaedic and dental applications such as hip prosthesis, artificial tooth roots, screws, plates, cylinder push-ins, blades and subperiostal implants. These coatings provide better implant-coating leading to overcome for the loosening of the coating according to higher coating-implant interface than implant-coating interface. The corrosion resistant,

crack-free coatings are beneficial in terms of prevention for the metallic ion release from the implant. These properties expand the usage areas of these coated implants for internal fixation applications.

REFERENCES

1. W. Suchanek and M. Yoshimura, Processing and properties of hydroxyapatite-based biomaterials for use as hard tissue replacement implants. Journal of Materials Research, 1998, 13(1): p. 94-117
2. M. Vallet-Regi and J. M. Gonzalez-Calbet, Calcium phosphates as substitution of bone tissues. Progress in Solid State Chemistry, 2004, 32(1-2): p. 1-31.
3. S. Weiner and H. D. Wagner, The Material Bone: Structure-Mechanical Function Relations. Annual Review of Materials Science, 1998, 28(1): p. 271-298.
4. R. Z. LeGeros, Biological and Synthetic Apatites, Edited by P. W. Brown and B. Constantz, Hydroxyapatite and Related Materials, CRC Press, Florida, USA, 1994
5. M. Long and H. J. Rack, Titanium alloys in total joint replacement--a materials science perspective. Biomaterials, 1998, 19(18): p. 1621-1639.
6. S. M. Green, (ii) Deformation of materials. Current Orthopaedics, 2006, 20(1): p. 9-15.
7. U. K. Mudali, T. M. Sridhar and B. Raj, Sadhana, 2003, 28(3-4): p. 601-637.
8. J. B. Park and Y. K. Kim, Biomaterials:Principles and Applications, edited by J. B. Park and J. D. Bronzino, CRC Press, Florida, USA, 2003
9. S. H. Teoh, Fatigue of biomaterials: a review. International Journal of Fatigue, 2000, 22(10): p. 825-837.
10. F. G. Evans and A. King, Biomedical Studies of the Musculosketal System. 1961: p.49-53
11. T. Kokubo, H.-M. Kim and M. Kawashita, Novel bioactive materials with different mechanical properties. Biomaterials, 2003, 24(13): p. 2161-2175.
12. P. R. Bouchard, J. Black, B. A. Albrecht, R. E. Kaderly, J. O. Galante and B. U. Pauli, Carcinogenicity of CoCrMo (F-75) implants in the rat. Journal of Biomedical Materials Research, 1996, 32(1): p. 37-44.

13. ASM Handbook, Metallography and Microstructures, Philadelphia, USA 1992
14. C.-C. Shih, C.-M. Shih, Y.-Y. Su, L. H. J. Su, M.-S. Chang and S.-J. Lin, Effect of surface oxide properties on corrosion resistance of 316L stainless steel for biomedical applications. Corrosion Science, 2004, 46(2): p. 427-441.
15. A. F. von Recum, Handbook of Biomaterials Evaluation: Scientific, Technical and Clinical Testing of Implant Materials, McMillan Publishing Company, 1986
16. M. Niinomi, Recent biocompatible metallic materials Structural Biomaterials for the 21st Century as held at the 2001 TMS Annual Meeting; New Orleans, LA; USA;, 2001: p. 3-14.
17. A. L. Hutson, T. Nicholas and R. Goodman, Fretting fatigue of Ti-6Al-4V under flat-on-flat contact. International Journal of Fatigue, 1999, 21(7): p. 663-669.
18. W. L. Jaffe and D. F. Scott, Current Concepts Review - Total Hip Arthroplasty with Hydroxyapatite-Coated Prostheses. J Bone Joint Surg Am, 1996, 78(12): p. 1918-1934.
19. D. D. Deligianni, N. Katsala, S. Ladas, D. Sotiropoulou, J. Amedee and Y. F. Missirlis, Effect of surface roughness of the titanium alloy Ti-6Al-4V on human bone marrow cell response and on protein adsorption. Biomaterials, 2001, 22(11): p. 1241-1251.
20. T. Kokubo, H. M. Kim, M. Kawashita and T. Nakamura, REVIEW Bioactive metals: preparation and properties. Journal of Materials Science: Materials in Medicine, 2004, 15(2): p. 99-107.
21. R. Garcia and R. H. Doremus, Electron microscopy of the bone-hydroxylapatite interface from a human dental implant. Journal of Materials Science: Materials in Medicine, 1992, 3(2): p. 154-156.
22. L. Sun, C. C. Berndt, K. A. Gross and A. Kucuk, Material fundamentals and clinical performance of plasma-sprayed hydroxyapatite coatings: A review. Journal of Biomedical Materials Research, 2001, 58(5): p. 570-592.

23. M. F. Morks and A. Kobayashi, Influence of gas flow rate on the microstructure and mechanical properties of hydroxyapatite coatings fabricated by gas tunnel type plasma spraying. Surface and Coatings Technology, 2006, 201(6): p. 2560-2566.
24. S. Dyshlovenko, L. Pawlowski, P. Roussel, D. Murano and A. Le Maguer, Relationship between plasma spray operational parameters and microstructure of hydroxyapatite coatings and powder particles sprayed into water. Surface and Coatings Technology, 2006, 200(12-13): p. 3845-3855.
25. Y. C. Tsui, C. Doyle and T. W. Clyne, Plasma sprayed hydroxyapatite coatings on titanium substrates Part 1: Mechanical properties and residual stress levels, Biomaterials, 1998, 19(22): p. 2015-2029.
26. I. Corni, M. P. Ryan and A. R. Boccaccini, Electrophoretic deposition: From traditional ceramics to nanotechnology. Journal of the European Ceramic Society, 2008, 28(7): p. 1353-1367.
27. J. Ma, C. Wang and K. W. Peng, Electrophoretic deposition of porous hydroxyapatite scaffold. Biomaterials, 2003, 24(20): p. 3505-3510.
28. M. C. Kuo and S. K. Yen, The process of electrochemical deposited hydroxyapatite coatings on biomedical titanium at room temperature. Materials Science and Engineering: C, 2002, 20(1-2): p. 153-160.
29. X. Lu, Z. Zhao and Y. Leng, Calcium phosphate crystal growth under controlled atmosphere in electrochemical deposition. Journal of Crystal Growth, 2005, 284(3-4): p. 506-516.
30. W. Yan, T. Nakamura, M. Kobayashi, H. Kim, F. Miyaji and T. Kokubo, Bonding of chemically treated titanium implants to bone. Journal of Biomedical Materials Research, 1997, 37(2): p. 267-275.
31. M. N. Rahaman, Ceramic Processing and Sintering; Sol-Gel Processing, Second Edition, Marcel Dekker Inc., New York, USA, 2003
32. http://www.gaematech.co.kr/img/sub2_bon_pic06.gif; "Last accessed date: April, 2008"
33. A. C. Pierre, Introduction to Sol-gel Processing, Second Edition, Kluwer Academic Publishers, Massachusetts, USA, 2002

34. C. J. Brinker and G. W. Scherer, Sol-gel Science: The Physics and Chemistry of sol-gel processing, Academic Press Inc., California, USA, 1990
35. L. L. Hench, Sol-gel materials for bioceramic applications. Current Opinion in Solid State and Materials Science, 1997, 2(5): p. 604-610.
36. C. You, S. Oh and S. Kim, Influences of Heating Condition and Substrate-Surface Roughness on the Characteristics of Sol-Gel-Derived Hydroxyapatite Coatings Journal of Sol-Gel Science and Technology, 2001, 21(1-2): p. 49-54.
37. C. S. Chai, K. A. Gross and B. Ben-Nissan, Critical ageing of hydroxyapatite sol-gel solutions. Biomaterials, 1998, 19(24): p. 2291-2296.
38. H.-W. Kim, Y.-M. Kong, C.-J. Bae, Y.-J. Noh and H.-E. Kim, Sol-gel derived fluor-hydroxyapatite biocoatings on zirconia substrate. Biomaterials, 2004, 25(15): p. 2919-2926.
39. H.-W. Kim, Y.-H. Koh, L.-H. Li, S. Lee and H.-E. Kim, Hydroxyapatite coating on titanium substrate with titania buffer layer processed by sol-gel method. Biomaterials, 2004, 25(13): p. 2533-2538.
40. H.-W. Kim, H.-E. Kim, V. Salih and J. C. Knowles, Hydroxyapatite and titania sol-gel composite coatings on titanium for hard tissue implants; Mechanical and in vitro biological performance. Journal of Biomedical Materials Research, 2005, 72B(1): p. 1-8.
41. E. Milella, F. Cosentino, A. Licciulli and C. Massaro, Preparation and characterization of titania/hydroxyapatite composite coatings obtained by sol-gel process. Biomaterials, 2001, 22(11): p. 1425-1431.
42. T. Peltola, M. Pätsi, H. Rahiala, I. Kangasniemi and A. Yli-Urpo, Calcium phosphate induction by sol-gel-derived titania coatings on titanium substrates in vitro. Journal of Biomedical Materials Research, 1998, 41(3): p. 504-510.
43. A. Balamurugan, G. Balossier, S. Kannan, J. Michel and S. Rajeswari, In vitro biological, chemical and electrochemical evaluation of titania

reinforced hydroxyapatite sol-gel coatings on surgical grade 316L SS. Materials Science and Engineering: C, 2007, 27(1): p. 162-171.

44. M. Akao, H. Aoki and K. Kato, Mechanical properties of sintered hydroxyapatite for prosthetic applications. Journal of Materials Science, 1981, 16(3): p. 809-812.

45. M. Jarcho, C. Bolen, M. Thomas, J. Bobick, J. Kay and R. Doremus, Hydroxylapatite synthesis and characterization in dense polycrystalline form. Journal of Materials Science, 1976, 11(11): p. 2027-2035.

46. G. H. Nancollas and J. Zhang, Formation and dissolution mechanisms of calcium phosphates in aqueous systems, Edited by P. W. Brown and B. Constantz, Hydroxyapatite and Related Materials, CRC Press, Florida, USA, 1994

47. A. Nakajima, K. Takakuwa, Y. Kameshima, M. Hagiwara, S. Sato, Y. Yamamoto, N. Yoshida, T. Watanabe and K. Okada, Preparation and properties of titania-apatite hybrid films. Journal of Photochemistry and Photobiology A: Chemistry, 2006, 177(1): p. 94-99.

48. Handbook of Chemistry and Physics, 64th edition, Edited by R. C. Weast, M. J. Astle and W. H. Beyer, CRC Press, Florida, USA, 1983-1984

49. G. Wilmann, Coating of implants with hydroxyapatite - material connections between bone and metal. Advanced Engineering Materials, 1999, 1(2): p. 95-105.

50. E. R. Kreidler and F. A. Hummel, Phase relationships in the system SrO-P_2O_5 and the influence of water vapor on the formation of $Sr_4P_2O_9$. Inorganic Chemistry, 1967, 6(5): p. 891.

51. I. Rehman and W. Bonfield, Characterization of hydroxyapatite and carbonated apatite by photo acoustic FTIR spectroscopy. Journal of Materials Science: Materials in Medicine, 1997, 8(1): p. 1-4.

52. S. Leeuwenburgh, P. Layrolle, F. Barrère, J. de Bruijn, J. Schoonman, C. A. van Blitterswijk and K. de Groot, Osteoclastic resorption of biomimetic calcium phosphate coatings in vitro. Journal of Biomedical Materials Research, 2001, 56(2): p. 208-215.

53. R. N. Panda, M. F. Hsieh, R. J. Chung and T. S. Chin, FTIR, XRD, SEM and solid state NMR investigations of carbonate-containing hydroxyapatite nano-particles synthesized by hydroxide-gel technique. Journal of Physics and Chemistry of Solids, 2003, 64(2): p. 193-199.
54. L. D. Landau and B. G. Levich, Dragging of a liquid by a moving plate, Acta Physiochim, U.R.S.S., 1942, 17: p. 42-54
55. I. Strawbridge and P. F. James, The factors affecting the thickness of sol-gel derived silica coatings prepared by dipping. Journal of non-crystalline solids, 1986, 86(3): p. 381-393
56. Y.-W. Rhee, H.-W. Kim, Y. Deng and B. R. Lawn, Contact-induced Damage in Ceramic Coatings on Compliant Substrates: Fracture Mechanics and Design. Journal of the American Ceramic Society, 2001, 84(5): p. 1066-1072.
57. C.-S. Lee, D. K. Kim, J. Sanchez, P. Miranda, A. Pajares and B. R. Lawn, Rate Effects in Critical Loads for Radial Cracking in Ceramic Coatings. Journal of the American Ceramic Society, 2002, 85(8): p. 2019-2024.

APPENDIX A

ICDD CARD NUMBERS

Table A.1. ICDD Card Numbers of the substrate and final products.

Name	ICDD Card Number
Hydroxyapatite	09-0432
Dicalcium phosphate dihydrate	09-0077
Calcium oxide	03-0865
Titania (Anatase)	21-1272
Ti6Al4V	n/a